Dipl.-Ing. Astrid Stadlhofer

Development of Pt-free anode catalysts for alkaline direct ethanol fuel cells

DISSERTATION

Zur Erlangung des akademischen Grades
einer Doktorin der technischen Wissenschaften
erreicht an der

Technischen Universität Graz

Betreuung: Assoc.Prof. Dr. Viktor Hacker
Institut für Chemische Verfahrenstechnik und Umwelttechnik
Technische Universität Graz

2013

Abstract

The direct oxidation of renewable fuels such as alcohols in fuel cells is a promising option for the generation of electric power in portable and mobile applications with low power demand. Ethanol is mainly produced from renewable feedstock and its low toxicity and relatively high boiling point facilitate easy handling and storage. Efficient direct oxidation of ethanol leads to fuel cells with high energy density and low emissions.

The aim of this work was the development of a highly active and efficient electrocatalyst system for the oxidation of ethanol in alkaline environment which avoids the use of the rare and expensive platinum group metals (Pt, Pd, Ru etc.). The extensive literature review in the thesis revealed that only a very limited number of elements fulfill the requirements for the use as catalyst in Alkaline Direct Ethanol Fuel Cells. The experimental section of the thesis can be divided in three major parts: the influence of the support material of the catalyst system, the preparation method and the fabrication and characterization of bimetallic catalysts.

Since electrocatalytic reactions take place on the surface of the catalyst, they are very sensitive to the heterogeneous interface. Therefore, the main goal was to optimize the surface of the catalyst and adapt the preparation methods and materials. Supported nickel and gold catalyst systems represent a promising alternative to Pt group metals. Nickel as well as gold exhibits a strong activity towards the ethanol oxidation reaction (EOR) in alkaline media. The pretreatment of the carbon support material has a great impact on the activity of the electrocatalyst. Several nickel and gold catalysts supported on different carbon materials with varied pretreatment have been prepared and their activity and stability towards the ethanol oxidation reaction has been examined. Deposition of gold on different thermally pretreated carbon support materials resulted in a reduced onset potential of the EOR. The application of a water in oil microemulsion method for metal deposition significantly enhanced the stability and the peak current densities. Three different methods for the preparation of bimetallic catalysts were applied: codeposition, subsequent deposition and a galvanic replacement reaction. The use of Au and Ni simultaneously facilitates the EOR on a wider potential range and results in higher amounts of current than single metal catalysts.

Kurzfassung

Die direkte Oxidation von niedermolekularen, organischen Verbindungen wie Ethanol stellt eine vielversprechende Methode zur Gewinnung von Strom in portablen und mobilen Anwendungen dar.

Das Ziel dieser Arbeit war die Entwicklung eines hochaktiven und effizienten Katalysatorsystems für die Elektrooxidation von Ethanol in alkalischer Lösung ohne Verwendung von Platinmetallen (Pt, Pd, Ru etc.). Die ausführliche Literaturrecherche dieser Arbeit zeigte, dass nur eine sehr begrenzte Anzahl von Elementen die Anforderungen für die Verwendung als Katalysatoren in alkalischen Direkt-Ethanol-Brennstoffzellen erfüllen. Der experimentelle Teil dieser Arbeit kann in drei Schwerpunkte unterteilt werden: das Trägermaterial, die Herstellungsmethode und bimetallische Katalysatoren.

Da elektrokatalytische Reaktionen auf der Oberfläche des Katalysators stattfinden, war es das wichtigste Ziel, die Oberfläche des Katalysators zu optimieren und die Materialien sowie deren Herstellung und Vorbehandlung anzupassen. Nickel und Gold mit Kohlenstoff als Trägermaterial stellen eine interessante Alternative zu Platinmetallen dar. Beide Metalle katalysieren hochaktiv die Ethanoloxidation im alkalischen Medium. Die Vorbehandlung des Kohlenstoff-Trägermaterials wirkt sich stark auf die Aktivität des Katalysators aus. Der Einfluss der Art des Trägermaterials und dessen Vorbehandlung auf die elektrokatalytische Aktivität und Stabilität wurden untersucht. Die Abscheidung von Gold auf thermisch vorbehandeltem Trägermaterial führte zu einer deutlichen Absenkung des Ethanoloxidationspotentials. Die Anwendung einer Wasser-in-Öl-Mikrolemulsionsmethode verbesserte die Stabilität der Katalysatoren und erhöhte die Spitzenstromdichten. Drei verschiedene Methoden wurden angewandt, um bimetallische Katalysatoren herzustellen: simultane Abscheidung, aufeinanderfolgende Abscheidung und eine galvanische Austauschreaktion. Die Verwendung von bimetallischen AuNi-Katalysatoren ermöglicht die Ethanoloxidation in einem breiteren Potentialfenster bei höheren Stromdichten als monometallische Katalysatoren.

Content

1. Introduction

Fuel cells are considered as the key technology on the way to a sustainable energy supply. The growing demand in renewable resources and the slow transformation of the energy and transport sector of the recent years aroused increasing interest in an efficient energy conversion which supports the fuel cell technology to take the last hurdle towards commercialization. In combination with renewable hydrogen, fuel cells provide CO_2 free, safe energy for a large range of applications including large scale stationary power generation, mobile and portable applications [1]. However, the shortcomings of hydrogen fueled polymer electrolyte fuel cells (PEFCs) for portable devices are obvious; heavy, pressurized hydrogen tanks and unavailable hydrogen infrastructure prevent from reasonable applications as portable low power supply. Therefore alternative fuels were investigated in order to take advantage of the high efficient energy conversion ability of fuel cells in combination with easy fuel handling, low weight and no recharging times. Alcohols were identified as promising alternatives due to high energy densities and easy availability.

This thesis concentrates on alkaline direct ethanol fuel cells (ADEFCs), in particular on the anode catalyst system. The centerpiece of each electrode or even fuel cell is the catalyst. A suitable anode catalyst enables a complete and therefore efficient oxidation of the fuel. The high requirements on the catalyst were usually handled with high platinum loadings. However, platinum and platinum group metals (pgm) including palladium, rhodium, iridium and ruthenium are expensive metals (Figure 1) and especially the Pt loading is a significant cost factor in fuel cell manufacturing. Operation in alkaline environment significantly enlarges the range of stable metals and facilitates the electrochemical reactions.

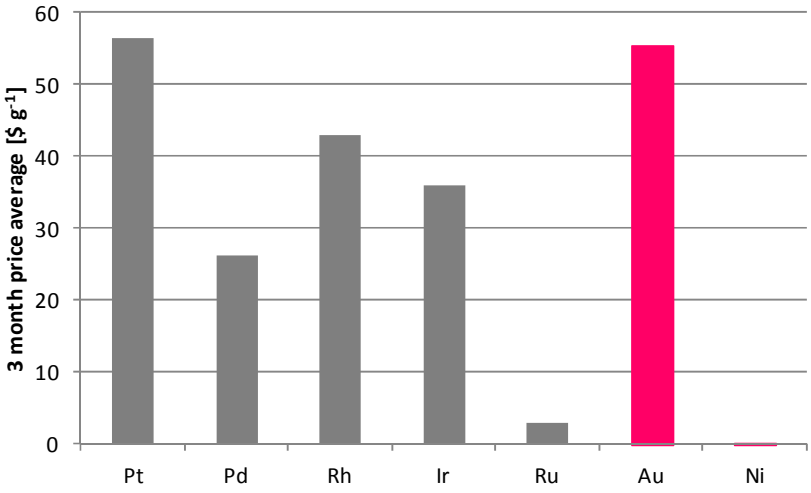

Figure 1: 3 month average price of pgm metals [2]**, Au and Ni** [3]**. The prices are an average of the daily values between 25.1.2013 and 25.4.2013 based on JM Base Price (pgm metals), London PM (Au) and LME Cash (Ni).**

In this work alternatives to PGM are investigated and developed. After extensive literature research and a screening for metals which show activity in electrocatalysis of the ethanol oxidation reaction (EOR), nickel and gold were chosen as base for investigations on the nature of the reaction and further improvements on the activity. The focus on the practical work was set on the identification and adaption of the catalyst-electrolyte interface. This was realized through optimization of the pretreatment of the support material and the method for the metal deposition. Since no single metal was able to fulfill the manifold requirements for a suitable PGM free anode catalyst, it was evident that bimetallic catalysts allow inserting additional features and multiply the functionality.

Chapter 2 of this thesis provides fundamentals on alkaline and direct fuel cells. In chapter 3 a closer look on the production of the fuel, in particular ethanol production from lignocellulosic feedstocks is given. The forth chapter summarizes publications on the electrocatalysis of Ni and Au, points out the actual state of the metal surface during operation as catalyst in alkaline medium and proposes reaction mechanisms based on facts from literature. In the fifth chapter experimental results are represented with emphasis on three main key aspects which are optimization of the support material, preparation methods and bimetallic catalysts.

2. Fundamentals

2.1. Alkaline fuel cells

The first fuel cells invented by Schönbein and Grove in the 19th century were based on the reaction of hydrogen and oxygen to water in acidic environment. More than 60 years later the first patents were applied for the first alkaline fuel cells (AFCs) [4]. Francis T. Bacon started experiments with potassium hydroxide (KOH) instead of acid as electrolyte [5]. As one of the first fuel cells, the alkaline fuel cell was further developed and reached a technological utilizable state. The most noted appearance was due to its application in NASA space missions. The Apollo mission and the space shuttle Orbiter were equipped with alkaline fuel cells [6]. AFCs were also considered for vehicular applications. Prototypes such as the Allis/Chalmers farm tractor, the GM "Electrovan" and the rebuilt Austin A40 were realized [5].

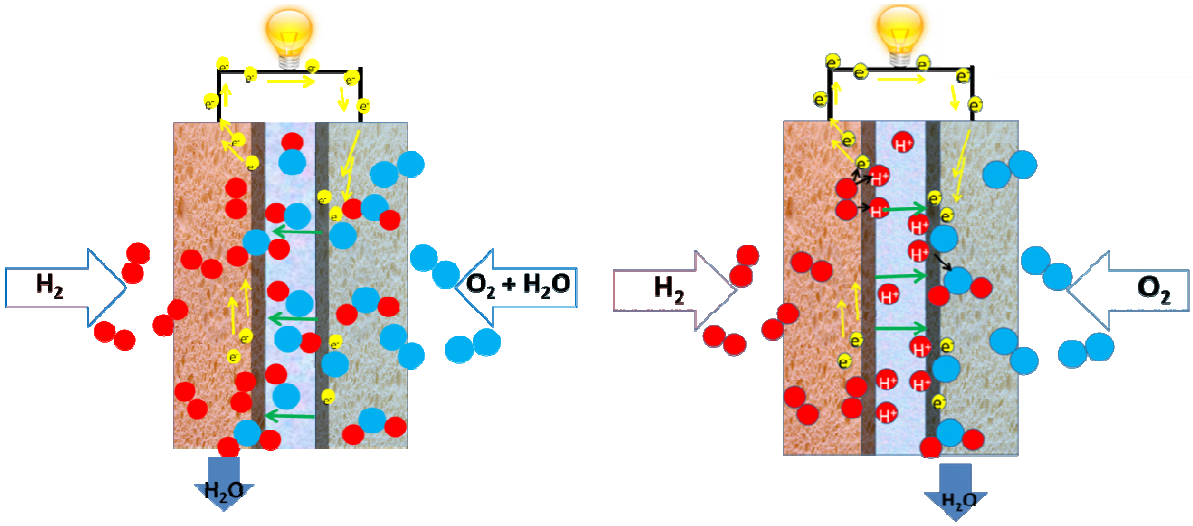

Anode:	$2H_2 + 4OH^- \rightarrow 4H_2O + 4e^-$	$2H_2 \rightarrow 4H^+ + 4e^-$
	$E_0 = -0{,}83V$	$E_0 = 0V$
Cathode:	$O_2 + 2H_2O + 4e^- \rightarrow 4OH^-$	$O_2 + 4e^- + 4H^+ \rightarrow 2H_2O$
	$E_0 = 0{,}4V$	$E_0 = 1{,}23V$
General:	$2H_2 + O_2 \rightarrow 2H_2O$	
	$E_0 = 1{,}23V$	

Figure 2: Working principle and reactions of an alkaline (left) and an acid (right) fuel cell

The working principle and the half-cell reactions of an alkaline fuel cell are shown in Figure 2. At the positive electrode (cathode), oxygen and water react catalytically to hydroxide ions. These hydroxide ions are transported via the electrolyte to the negative electrode (anode). At the anode, hydrogen is oxidized with the hydroxide ions to water and electrons, which flow through an external circuit to the cathode where they are consumed for oxygen reduction. The alkaline oxygen reduction requires two

molecules water per oxygen molecule. At the same time, four water molecules are produced during hydrogen oxidation. Water has to be transported from the anode to the cathode, whereas hydroxide ions migrate from the cathode to the anode (illustrated in Figure 2 with green arrows). The overall reaction produces on the anode side two molecules of water per molecule oxygen consumed.

Alkaline low temperature fuel cells constitute robust systems for electricity supply with a large spectrum of operation modes. The systems can be operated at ambient temperatures up to 200°C with molten or soluted potassium hydroxide as electrolyte. As ionic conductor between the electrodes, circulating or immobilized liquid electrolytes or gel electrolytes can be employed. Circulating electrolytes support the thermal management in stacks. Immobilized electrolytes, which used an asbestos net as matrix materials in the past, ensure an operation of the fuel cell without any moving parts, additional pumps and tanks as required for space or military applications [7].
Operation with liquid electrolytes entails special requirements for the electrode design. Multilayered electrodes which detain the corrosive electrolyte and are gas permeable were fabricated. Better electrode kinetics for anode and cathode reactions as well and lower corrosiveness to metals allow the use of non-noble metals as catalysts. Sintered nickel and silver electrodes, impregnated with platinum for higher activity or transition metals for higher stability were employed. Early AFC electrodes, such as in the Apollo program, used very high platinum loadings of up to 40 mg cm^{-2} [8].
Beside the very robust and reliable operation of AFCs and improved electrode kinetics in alkaline environment, some further advantages of AFCs exist. AFCs can reach high electrical efficiencies up to 70% [9], the water management is easy and the cold start behavior is superior to other fuel cell types [10]. The alkaline environment allows the use of thin, stamped metal bipolar plates with low ohmic resistance and lower acquisition costs compared to PEMFCs which require expensive corrosion resistive materials [11].
The promising positive features led to an extensive research on AFCs since the 1950s. Due to some undeniable drawbacks of the AFC and a fast development of proton exchange membrane fuel cells (PEMFCs) in the mid-1980s, research and industry focused on acid systems.
Most of these drawbacks arise from the use of liquid electrolyte. Additionally to electrolyte leakage issues, the direction of the gravity influences the liquid. Especially for space applications, this drawback has to be avoided by immobilized electrolytes [12]. Carbon dioxide (CO_2), a natural component of the air which represents 0,04 vol%, leads to severe performance losses. The reaction of CO_2 with the KOH in the aqueous electrolyte to carbonate reduces the ionic conductivity by reducing the available hydroxyl groups:

$$CO_2 + 2KOH \rightarrow K_2CO_3 + H_2O$$

Furthermore, the large metal carbonate precipitate, such as K_2CO_3 crystals, blocks the micropores of the electrodes and reduces the active surface area significantly. Metal carbonate and metal hydrogen carbonate precipitates can also block pores and mechanically degrade the active layers of the electrode:

$$CO_2 + 2OH^- \rightarrow CO_3^{2-} + H_2O$$
$$CO_2 + 2OH^- \rightarrow HCO_3^{2-}$$

Measures to avoid these detrimental effects are the use of e.g. soda lime in order to remove the CO_2 from the air by chemical absorption or circulating the electrolyte. Both methods imply additional peripheral supplements and further complication of the system [8,13].

All these drawbacks of the AFC can be circumvented by the use of anion exchange membranes. At the beginning of the 21st century, the liquid KOH has been replaced by solid alkaline polymer electrolytes [14,15]. This innovation led to an boom of research on alkaline fuel cells over the recent years [16]. The anion exchange membranes (AEMs) in the AFC work analog to the proton exchange membrane (PEM) with the important difference that hydroxide and carbonate ions are conducted rather than protons. The introduction of AEMs to AFCs retains the electrocatalytic advantages and excludes the negative effects from the liquid electrolyte such as leakage, electrode flooding and low CO_2 tolerance. Although still a certain amount of carbonate is formed due to the reaction of OH^- with CO_2, there will be no solid precipitate since no mobile cations such as e.g. K^+ are present and the conducting species is fixed in a polymer [16].
AEMs have already been in use in electrodialysis for desalination, treatment of waste water and water hydrolysis [17].
Nevertheless, AEMs are still at an early stage of development and the requirements for fuel cell applications are challenging. In addition to a high ionic conductivity, impermeability for gases, electronic isolation and good mechanical and chemical stability during fuel cell operation are required. In order to provide adequate mechanic stability, the membranes have to be processed as thin as possible (ideally 50-80 µm) to avoid volume changes when immersed in water or in any liquid fuel [16]. Chemical stability is still a very critical issue and will be discussed in one of the following passages.

Since the diffusion coefficient for H^+ is about four times higher than for OH^-, a four times higher concentration of ionic groups would be necessary to achieve a comparable conductivity to acidic membranes [15]. However, this approach is limited due to the increasing deterioration of the mechanic properties with increasing number of ionic groups. Volume changes and brittleness in dehydrated state arise from too high concentrations of fixed charges [18]. Furthermore, quaternary ammonium (QA) ionic groups show a lower degree of dissociation than sulfonic acid groups [11].

As functional groups in anion AEMs the following structures can be used:

$-NH_3^+$ $\quad -RNH_2^+$ $\quad -R_3N^+$

$= R_2N^+$ $\quad -R_3P^+$ $\quad -R_2S^+$ [17]

Onium ions often represent the fixed charges in the polymer and facilitate the ion transport. Among these structures the QA group exhibits the highest chemical und thermal stability compared to sulfonium and phosphonium moieties [17]. Due to this fact, most of the AEMs are based on quaternary ammonium as they provide a reasonable stability in alkaline environment [11]. Furthermore, they are easily synthetically accessible and exhibit a good hydrophilicity [19]. Figure 3 shows the structure of a QA group. R represents an alkyl or aryl moiety. In contrary to the ammonium ion (NH_4^+) and its primary, secondary and tertiary form, the QA is permanently charged and independent from the pH of the environment. Moreover, nitrogen containing organic groups

such as guanidinium (Figure 4), imidazolium (Figure 5) and their derivatives exhibit promising characteristics in conductivity and stability [20].

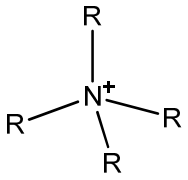

Figure 3: Quaternary ammonium group

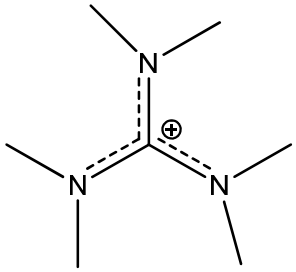

Figure 4: Guanidinium ion

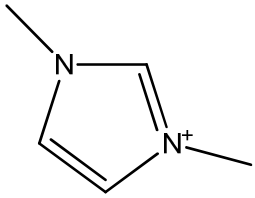

Figure 5: Imidazolium

The functional group is more susceptible for degradation than the polymer network, since the hydroxide ions are effective nucleophiles and the ionic groups, e.g. the QA groups are excellent leaving groups [11]. The high pH promotes nucleophilic attacks of the hydroxide ion [16]. Beside rearrangement reactions (mainly Sommelet-Hauser and Stevens), elimination and substitution reactions are competing for degradation of the QA groups. The predominant reaction pathway is strongly correlated to the nature of the polymer backbone [20]. If a hydrogen atom in antiperiplanar β-position to the nitrogen is available, the Hofmann elimination takes place (Figure 6). The attack of the hydroxide ion at the hydrogen atom in β-position leads to an alkene, an amine and water. This reaction belongs to the class of E2 elimination reactions [20]. In order to prevent degradation by the Hofmann elimination, polymer backbones that do not provide β-hydrogens have to be preferred.

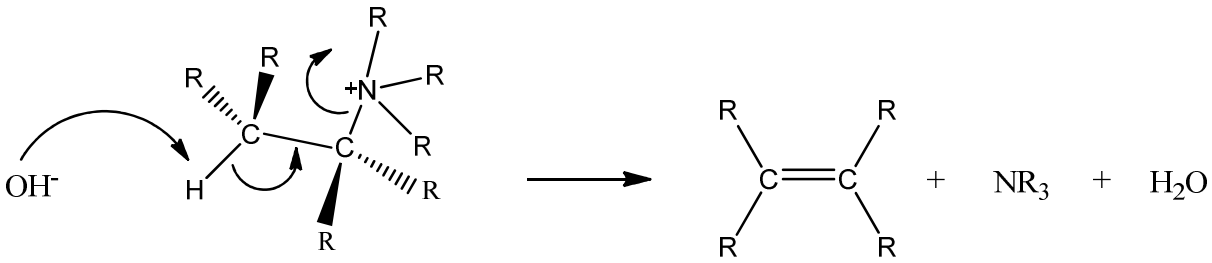

Figure 6: Scheme of the Hofmann elimination reaction pathway

If the α- and β-carbons to the nitrogen are sterically hindered and one of the substituents of the nitrogen is a methyl group, alternatively an Ei elimination pathway is possible. In this case, the hydroxide attacks a hydrogen atom from the methyl group and results in the same products as the E2 reaction.

If no β-hydrogen is available, nucleophilic substitution takes place (Figure 7). The hydroxide ion attack the α-carbon of the nitrogen atom and an alcohol, an amine and water are formed during this S_N2 reaction. The α-carbon can be part of the polymer backbone as well as the substituent of the nitrogen group, dependent on the constellation and nature of all substituents [20].

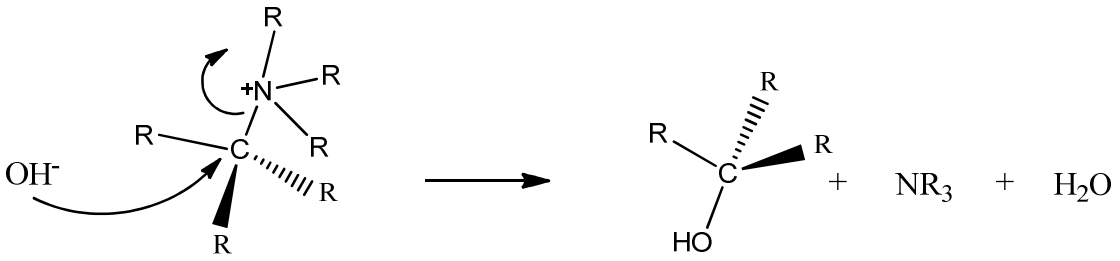

Figure 7: Scheme of the nucleophilic substitution reaction pathway

The same products as formed by a S_N2 substitution reaction are formed by rearrangements such as the Stevens (an 1,2 rearrangement) and Sommelet-Hausner rearrangements. Both reactions are based on an ylide formation by deprotonation of one of the nitrogen substituents, followed by further rearrangements [20].

Generally, AEMs consist of a charged functional group, a polymer backbone and optionally a crosslinking agent. The functional groups can origin from the monomer of the backbone or from chemical modification such as functionalization. The polymer backbone should be chemically stable and withstand nucleophilic attacks from the hydroxide ions. From the vast number of polymers, aromatic polymers, such as PSU (polysulfone), fluorinated polymers or biopolymers such as chitosan (Figure 8) can be chosen.

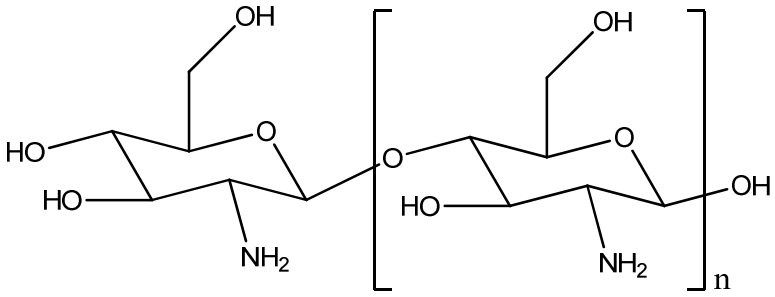

Figure 8: Deacetylated chitosan

Alternatively to these KOH/NaOH free AEMs, electrolyte doped membranes are in use. These membranes consist of a polymer matrix such as polyethylene oxide (PEO) (Figure 9), polybenzimidazole (PBI) or polyvinyl alcohol (PVA) and a hydroxide salt, mostly potassium or sodium hydroxide. These membranes have no intrinsic ion exchange capacity and comparably to liquid electrolytes, these membranes suffer from carbonation [20].

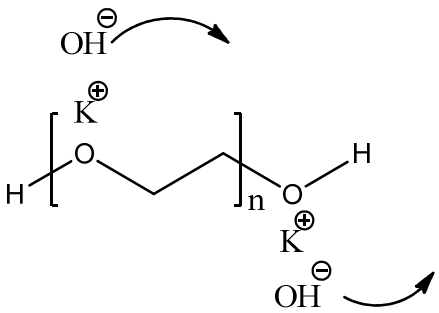

Figure 9: PEO doped with KOH

2.2. Direct ethanol fuel cells

Direct alcohol fuel cells (DAFC) generate electricity by direct oxidation of organic compounds without a preceding reforming step of the fuel. Possible fuels are:

- methanol
- ethanol
- ethylene glycol
- glycerol
- propanol

The direct use of alcohols in fuel cells opens up the opportunity to avoid efficiency losses from fuel processing, in particular the production of hydrogen. Furthermore, the state of aggregation of all the named alcohols above is liquid at standard conditions. This facilitates easier storage and handling of the fuel and allows further use of the traditional fuel infrastructure. The energy density of these low-molecular organic compounds is significantly higher than of hydrogen and is comparable to gasoline. Figure 10 shows the volumetric combustion energy density for several fuels [21].

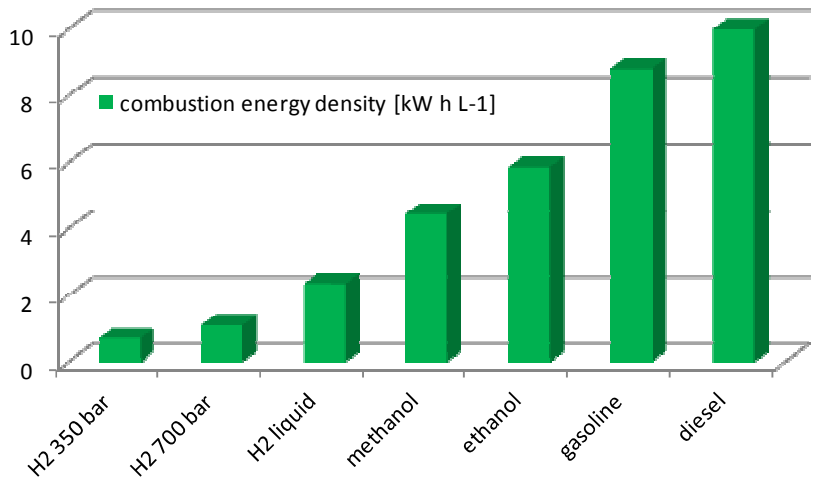

Figure 10: The combustion energy density calculated from the LHV per liter fuel [21]

For simple alcohols, the energy density increases with the number of carbon atoms in the molecule. Unfortunately, today's catalysts are not capable of converting the whole accumulated chemical energy into electricity. The electrooxidation of most alcohols follows complex reaction mechanisms and therefore exhibit sluggish reaction kinetics. Thus, hydrogen is still the most efficient fuel due to its simple oxidation mechanism [22]. The performance of a DAFC is still inferior compared to a PEMFC supplied with hydrogen [23]. Among alcohols, methanol has the highest electrochemical kinetics. The electrocatalytic cleavage of the C-C bond is still an important issue and hence requires extensive research (see Chapter 4).

DAFCs follow a similar principle as PEFCs. The fuel is oxidized to CO_2 at the anode, and oxygen is reduced at the cathode side:

$$2C_nH_{2n+1}OH + 3n\ O_2 \rightarrow 2n\ CO_2 + (2n+2)H_2O$$

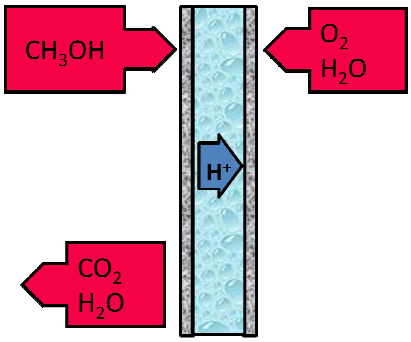

Figure 11: Scheme of a direct methanol fuel cell (DMFC)

Due to the earlier mentioned simple system set up at low temperatures, DAFCs are perfectly suitable for portable applications. The most important application is the off grid power supply for electronic devices such as mobile phones, laptops and military devices with power outputs up to 100W [24]. So far, only DMFCs (Figure 11) are commercially available. The direct electrochemical conversion of alcohol takes place at room temperature or even below. For methanol, if the overall process is considered, the preceded transformation of methanol to hydrogen via steam reforming, partial oxidation or autothermal oxidation and its further conversion to electricity in a proton exchange membrane fuel cell (PEMFC) is more beneficial for high power applications. Due to the simple system configuration, low power demands are better served with direct conversion in fuel cells [21]. But this boundary is very imprecise and is steadily shifted towards the DAFC with the development of better electrocatalysts.

Acid systems with proton exchange membranes as well as alkaline systems employing anion exchange membranes are possible. Generally, if the term “alkaline” is not added to the name, one can expect an acid system. Alkaline direct alcohol fuel cells have some advantages to its acid homologs. In contrast to hydrogen fuelled PEMFCs, the electrokinetic overpotential of DAFCs is not mainly caused by the oxygen reduction, but the anode reaction is chemically inhibited too [23]. As known for many reactions, the alkaline environment facilitates the electrocatalysis of the oxidation reaction. Furthermore, the direction of the osmotic drag drastically reduces alcohol crossover from the anode to the cathode [25]. This means, the proton transport through the membrane leads to alcohol transport from the anode to the cathode via electroosmosis. This fuel crossover leads not only to fuel loss, but to a mixed potential at the cathode and as a consequence to a reduced cell voltage and a lower Coulombic efficiency [23].

Focused on environmental and health hazards ethanol has some undeniable advantages to other fuels. Ethanol is only irritant to the human health in very high concentrations and it is possible to produce ethanol from biomass in safe processes [26]. The boiling point of 78°C is relatively low and additionally, it exhibits a high energy density of 8.01 kWh kg^{-1} [27]. Compared to fuels used nowadays, ethanol can be regarded as a less harmful chemical.

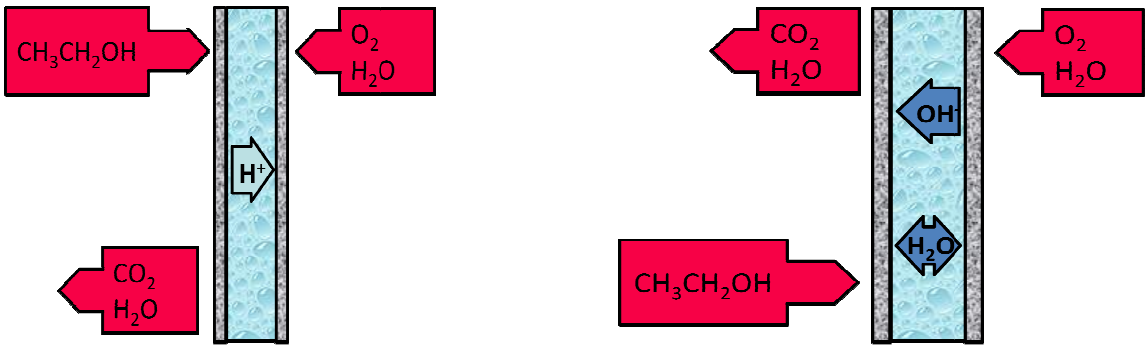

Anode: $CH_3CH_2OH + 9\,H_2 \rightarrow 2\,CO_2 + 12\,H^+ + 12\,e^-$ $E_0 = 0{,}084V$ | $CH_3CH_2OH + 12\,OH^- \rightarrow 2\,CO_2 + 9\,H_2O + 12\,e^-$ $E_0 = -0{,}744V$

Cathode: $O_2 + 4e^- + 4H^+ \rightarrow 2H_2O$ $E_0 = 1{,}229V$ | $O_2 + 2H_2O + 4e^- \rightarrow 4OH^-$ $E_0 = 0{,}401V$

General: $CH_3CH_2OH + 3\,O_2 \rightarrow 2\,CO_2 + 3\,H_2O$ $E_0 = 1{,}145V$

Figure 12: Scheme of a DEFC

The half-cell reactions and potentials for the acid system is well known and cited in several textbooks [28]. The anode potential for the reaction in alkaline media is calculated as follows:

$$CH_3CH_2OH(l) + 12\,OH^-(aq) \rightarrow 2\,CO_2(g) + 9\,H_2O(l) + 12\,e^-$$

$$-\Delta G_A^0 = 2 \times \Delta G_{CO_2} + 9 \times \Delta G_{H_2O} - \Delta G_{CH_3CH_2OH} - 12 \times \Delta G_{OH^-}$$

$$-\Delta G_A^0 = 2 \times (-394{,}36) + 9 \times (-237{,}13) - \big((-174{,}78) + 12 \times (-157{,}24)\big) =$$

$$= -861{,}23\ kJ\ mol^{-1}$$

$$E_r^0 = \frac{-\Delta G^0}{zF}$$

$$E_A^0 = \frac{-\Delta G_A^0}{12F} = \frac{-861{,}23}{12F} = -0{,}744\ V$$

All standard Gibbs free energies of formation and formation enthalpies are quoted from [29]. The abbreviations in brackets in the half cell reactions refer to the aggregation state of the substance. The cathode potential is calculated as follows:

$$O_2(g) + 2H_2O(l) + 4e^- \rightarrow 4OH^-(\text{aq})$$

$$-\Delta G_K^0 = 2 \times \Delta G_{H_2O} - 4 \times \Delta G_{OH^-} = 2 \times (-237{,}13) - 4 \times (-157{,}24) =$$

$$= 154{,}70\ kJ\ mol^{-1}$$

$$E_K^0 = \frac{-\Delta G_K^0}{12F} = \frac{154{,}70}{12F} = 0{,}401\ V$$

These potentials were subtracted in the next step to calculate the standard electrode potential:

$$E^0 = E_K^0 - E_A^0 = 0{,}401V + 0{,}744V = 1{,}145\ V$$

$$E_r^0 \ldots\ldots reversible\ cell\ voltage$$
$$\Delta G^0 \ldots. Gibbs\ free\ energy\ change$$

$$\Delta G^0 = \left(2 \times \Delta G_{CO_2} + 3 \times \Delta G_{H_2O}\right) - \Delta G_{CH_3CH_2OH} = 1325\ \text{kJ mol}^{-1}$$

$$\Delta H^0 = \left(2 \times \Delta H_{CO_2} + 3 \times \Delta H_{H_2O}\right) - \Delta H_{CH_3CH_2OH} = 1367\ \text{kJ mol}^{-1}$$

The maximal theoretical electrical energy conversion efficiency (η) is

$$\eta = \frac{\Delta G^0}{\Delta H^0} = 97\%$$

This calculation is under the assumption the reaction is a complete oxidation. In reality, complete oxidation is achieved very rarely but partial oxidation products such as acetic acid and acetaldehyde (Table 1). This lowers the electrical efficiency drastically.

Table 1: Overview of theoretical voltage and reversible energy conversion efficiencies with complete and incomplete oxidation

Overall reaction	Anode reaction	E^0	η
$\boldsymbol{CH_3CH_2OH + 3\ O_2 \rightarrow 2\ CO_2 + 3\ H_2O}$	$CH_3CH_2OH + 12\ OH^- \rightarrow 2\ CO_2 + 9\ H_2O + 12\ e^-$	1,145	97 %
$\boldsymbol{CH_3CH_2OH + O_2 \rightarrow CH_3COOH + H_2O}$	$CH_3CH_2OH + 4\ OH^- \rightarrow CH_3COOH + 3\ H_2O + 4\ e^-$	1,172	92 %
$\boldsymbol{CH_3CH_2OH + \frac{1}{2}O_2 \rightarrow CH_3CHO + H_2O}$	$CH_3CH_2OH + 2\ OH^- \rightarrow CH_3CHO + 2\ H_2O + 2\ e^-$	0,987	95 %

3. Ethanol production: lignocellulose based ethanol

3.1. Introduction

Since fossil energy sources are limited, the research for an energy supply based on renewable resources has high priority in order to meet the world's growing energy demand and deal with the greenhouse effect.

In 2006 31 billion liters of bioethanol were produced worldwide in 2006 which rose to 39 billion liters and 100 billion liters are estimated for 2015. Today the fraction of ethanol from lignocellulosic biomass can be neglected. Brazil and USA which produce 62% of the world production use mainly sugarcane and corn as feedstocks [30]. In the following sections promising alternatives will be discussed more closely.

In 2005, 67% of the ethanol production was dedicated to transportation fuels and the rest for food industry [31]. Ethanol is the most used biofuel. It can be blended with petrol or used neat in internal combustion engines (ICE). Ethanol is an attractive fuel because it has a higher octane number, broader flammability limits and a higher evaporation heat than gasoline which leads to advantages in the theoretical efficiency. Furthermore, the oxygen content of the ethanol molecule reduces NO_x and particulate matter emissions. Its low energy density (33% less than gasoline), its corrosiveness and its miscibility are the main disadvantages of the use of ethanol as fuel for ICEs [31]. The use of ethanol as biofuel is targeted by the EU, USA, Brazil, India and many others by a compulsory or subsidized blend of gasoline with ethanol known as E5, E10 or E85 [32].

In 2010, 8 million tons of fuel were sold in Austria [33]. Since 2007, all gasoline fuels are blended with approximately 5,5 vol% of ethanol which results in a consummation of 106 201 tons of bioethanol in Austria in 2010 for transportation [33]. The ethanol production from sugar beet is 5,2 t/ha [34]. If the differences in energy densities are neglected, one can assume that the substitution of all consumed fuels with ethanol produced from sugar beet occupies roughly 15 000 km^2, which accounts for 18% of the total area of Austria [35].

3.2. Feedstocks

Overview

In general, Bioethanol feedstocks can be divided into three classifications:

- Sucrose containing feedstocks, e.g. sweet sorghum, sugar beet and cane etc.
- Starchy materials, e.g. wheat, corn, potatoes etc.
- Lignocellulosic biomass, e.g. wood, grass, straw etc. [36]

About 90% of all ethanol is derived from the first two classes by fermentation, the rest is produced synthetically [31]. The choice of the feedstock strongly depends on the geological and climate situation. In tropical areas as Brazil and Columbia ethanol is mainly produced from sugar cane, while corn is the main source in EU, USA and China [37]. Bioethanol gained from the first two points in the above shown table is called first generation Bioethanol, while Bioethanol from lignocellulosic biomass is called second generation Bioethanol [38]. Fermentation processes for sugar and starch crops are well developed, but some grave disadvantages will still exist in future: the competition with food application and as implication high fluctuation of prices and ethical conflicts. Furthermore, the sugar yield per hectare is very low [31].

Due to these problems, it might be impossible to tremendously increase ethanol production with current technologies. Lignocellulosic biomass is a promising source for ethanol because of the high content of cellulose and hemicelluloses and their abundance almost all over the world. However, from a technological point of view, conversion of lignocellulosic materials to ethanol is much more difficult than that of sugar or starch containing materials [37].

3.3. Lignocellulose based Ethanol

Lignocellulosic biomass is a desirable feedstock for fuel production since it is the most abundant renewable organic component in the biosphere. Approximately 50% of the biomass in the world are counted on lignocellulosic materials. 442 billion liters ethanol could be produced by lignocellulosic biomass per year [36]. This would help to reach the world's energy demands derived from renewable resources even with further growing consummation.

For the sake of independency from fossil resources, various concepts of biorefineries have been elaborated which focus not only on one valuable product but on utilizing each component of the feedstock. A Lignocellulosic Feedstock biorefinery (LCF biorefinery, Fig. 2) is regarded as a potential large scale industrial biorefinery whose products could substitute the traditional petrochemical market [39].

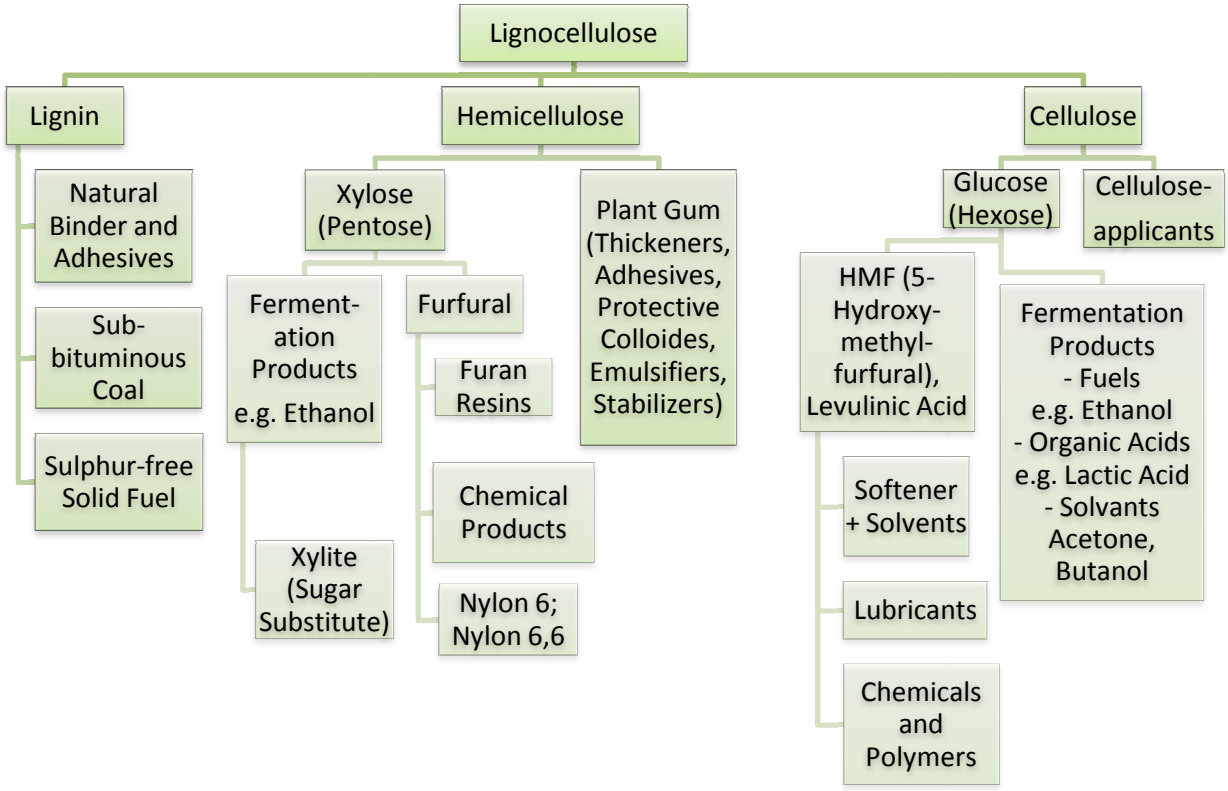

Figure 13: Scheme of a Lignocellulosic Feedstock Biorefinery (according to [39]**)**

3.4. Composition and chemical structure of lignocellulosic materials

Lignocellulosic materials are mainly composed by the 3 major constituents cellulose, hemicellulose and lignin which is also revealed by the name. Type and composition strongly depends on the employed feedstock (

Table 2).

Table 2: Contents of cellulose, hemicellulose and lignin in common lignocellulosic materials [40]

Lignocellulosic material	% Cellulose	% Hemi-cellulose	% Lignin
Hardwood	45-55	24-40	18-25
Softwood	45-50	25-35	25-35
Switch grass	**45**	**31,4**	**12-20**
Miscanthus	40	18	25
Coastal Bermuda grass	**25**	**35,7**	**9-18**
Corn stover	35-40	17-35	7-18
Wheat straw	**30**	**50**	**15**
Rice straw	36-47	19-25	10-24
Cotton seed hairs	**80-95**	**5-20**	**0**
Newspaper	40-55	25-40	18-30
White paper	**85-99**	**0**	**0-15**

3.4.1. Cellulose

Cellulose is a main part of the protective cell walls of plants as trunks, stalks and similar wooden portions of plant tissues. Isolated, cellulose appears as fibrous, water-insoluble substance.

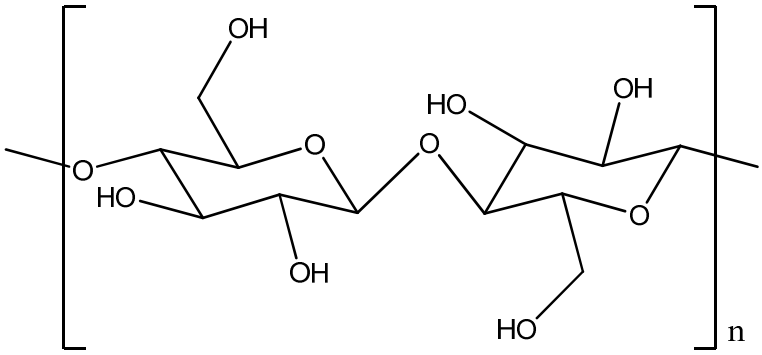

Figure 14: Glucose units in cellulose molecule

This unbranched homopolysaccharide consists of β-D –glucopyranose units that are covalently linked by (1 → 4) glycosidic bonds (Figure 14). These pyranose rings are in the thermodynamically preferred chair conformation $^4C_1$ with the hydroxyl groups in an equatorial position. The orientation of the linkages and additional hydrogen bonding make the polymer rigid and difficult to break. In nature, cellulose chains have a degree of polymerization (DP) of approximately 10 000 glucopyranose units in woodcellulose and 15 000 in native cotton cellulose [41]. This chain length varies with the origin and treatment of the raw material [42].

Cellulose accounts for 40-60% of the dry mass in lignocellulosic biomass. The process of breaking down the polysaccharide into free sugar molecules by adding water is called saccharification. The product of the hydrolysation of cellulose is glucose [31].

3.4.2. Hemicellulose

Hemicelluloses are the second most abundant polysaccharide and represent 20-40% of the dry mass of lignocellulosic biomass. Hemicellulose is not chemically homogenious like cellulose; it is a heterogeneous, highly branched polymer consisting of various sugars. Pentoses such as mainly xylose and arabinose; hexoses such as mannose, glucose and galactose; sugar acids and a small amount of non-sugars such as acetyl groups represent the most common components of hemicellulose. Hardwood hemicellulose contains mostly xylans, whereas softwood hemicellulose contains mostly glucomannans. Because of its branched, amorphous nature, hemicelluloses is relatively easy to hydrolyse [43].

3.4.3. Lignin

From a chemical point of view, lignin is very different compared to the other two major polymers that constitute lignocellulosic biomass. This biopolymer is an amorphous polyphenolic polymer which constitutes 10-25% of the dry mass of lignocellulosic biomass [31]. While the exact structure of lignin

is unclear, it is known that it is a highly irregular and heterogeneous with no regular repeating unit structures observed. Its function in nature is to encrust the cell walls and cement the cells together. This polyphenolic compound is essential for the growth of land plants because it provides mechanical support to the whole. Although beneficial for plants, the presence of lignin increases the industrial processing costs for cell wall deconstruction. Only a few organisms are able to degrade lignin into higher value products such as organic acids, phenols and vanillin [44]. For this reason, lignin usually incurs in ethanol production processes as residue and can be used to generate electricity and/or steam [45].

3.5. Lignocellulosic feedstocks

3.5.1. Wood and forest residues

Generally, wood is divided into softwood and hardwood. In countries of the Northern hemisphere, namely, particularly Sweden, Canada and USA, a significant part of the available biomass is softwood [46]. Coniferes are referred to as softwood, whereas trees with leaves like oak, willow, poplar and many more belong to hardwood. In Sweden, softwood is the most abundant raw material for ethanol production in the form of logging waste and waste from the forest industry [47].

The difference of softwood and hardwood is not only in the hardness as the names suggests, this property is due to differences in the chemical composition. Softwood consists of more hemicelluloses with lower xylose and higher mannose content than hardwood. Hardwood has significantly less lignin than softwood. Furthermore, lignin in softwood is composed of only two principal phenylpropane units which are coumaryl and guaiacyl that form the backbone. Hardwoods and herbaceous plants have additional syringyl groups. This simplification of the lignin structure severely complicates the process of delignification [48]. Additionally, the hemicelluloses in hardwood in mainly composed of hexoses which are with current technologies easier fermented to ethanol compared to the pentoses in softwood [37].

The combined sugar content of pine is very high which implies that the potential for ethanol production is very high too. Another promising feedstock is poplar because of its rapid growth. The annual yield of hybrid poplar trees in North America is estimated around 12 dry tons per hectare [31].

3.5.2. Grasses

Lignocellulosic perennial crops including grasses are a promising feedstock because of high yields, low costs and low environmental impact. Since the 1990s, research on switchgrass as energy crop is in progress. Switchgrass is a warm-season perennial grass native to North and Central America. It can grow on various soils and can grow to a maximum height of 3 m. Another large perennial grass is Miscanthus with a height of 2 m. Miscanthus is originally a native grass in Southeast Asia, brought to Europe as ornamental grass. Coastal Bermudagrass is another herbaceous, perennial crop grown in

the United States which can grow on different soil conditions and achieves a good biomass yield [37].

3.5.3. Agricultural wastes

Rice straw, wheat straw and corn stover are the major agricultural wastes. Rice straw is mainly incurred in Asia, whereas wheat straw and corn stover are mainly produced in America. Less than 6 % of corn straw is used for industrial processes and animal feed and bedding. This implies that more than 90 % of corn straw in the US is left on the fields. The situation with rice straw utilization is similar. Rice straw with an approximated global production of 600-900 million tons per year is the most abundant crop residue. Potentially 205 billion liters bioethanol per year could be produced out of rice straw [30].

3.5.4. Municipal solid waste

Lignocellulose holds a large fraction of municipal solid waste (MSW) amongst inorganic wastes, different types of natural polymers such as starch, lipids, glycogen, elastin, collagen, keratin and chitin as well as synthetic polymers such as polyesters, polyethylene and polypropylene [49]. Municipal wastes include lignocellulosic waste from domestic homes, industries and construction and demolition (C&D) sites. This lignocellulosic fraction from private households primarily consists of cellulose in the form of newspaper, wood and cardboard [50]. Engineered wood based materials from C&D consists of wallpapers, particle boards, plywood, strand boards and similar cellulose containing construction materials. Approximately 1,7 tons of lignocellulosic waste accrue from the construction of an average 180 m^2 house in the USA [51]. Residential and industrial municipal waste is mainly utilized in recycling or incineration, a small fraction and C&D waste are deposited in landfill sites [52]. The benefit from new technologies which permit the economically reasonable conversion of MSW to ethanol would be two-fold: the amount of lignocellulose waste and its negative effects on the environment would be decreased and secondly the waste would be converted to a valuable energy source especially beneficial for countries with limited access to starchy biomass such as Korea and Japan [50].

3.5.5. Availability

One major problem with bioethanol production is the availability of raw materials. This leads to a high volatility for the prices of the raw materials. Lignocellulosic biomass can serve as a cheap and abundant feedstock which offers the possibility to produce large amounts of ethanol from renewable resources at reasonable costs [53].

According to estimations [30], it would be possible to produce up to 442 billion liters ethanol per year from lignocellulosic materials and including crop residues and wasted crops, 491 billion liters ethanol per year could be reached. This is 16 times higher than the actual world bioethanol production which is based on first generation feedstock materials.

The in earlier sections mentioned agro-residues are also used as animal fodder or as combustion fuel. But only a very small portion of globally produced crop residues such as rice straw or corn stover is

used as animal feed, the main part is intricately disposed or removed from the field by burning, causing air pollution and affecting human health [30].

3.6. General process

A dissociation of the lignocellulose to ethanol process into single process steps is not definite and therefore not easy. Ethanol can be produced via a thermochemical process, a biochemical process or a combination of both. The thermochemical route includes the conversion of the lignocellulosic biomass into synthesis gas and further to ethanol. This process can be conducted in one step (direct route) or divided into several process steps (indirect route). The gasification process requires high temperatures, typically above 800°C and can be performed allothermal or autothermal [54]. Subsequently, the syngas is catalytically converted to ethanol. This step can either be homogeneously or heterogeneously catalysed [54]. In combined thermochemical and biochemical procedures, the syngas is fermented by microorganisms [55].

Nearly all biochemical lignocellulose to ethanol processes (Figure 15) start with the removal of large and unsuitable materials, followed by a diminution step to enlarge the active surface. The next step is hydrolysis where the material is broken down into simpler compounds. Then the cellulose fraction and the hemicellulose fraction are fermented to ethanol. The remaining part, lignin, can be used as boiler fuel or further processed to higher valued chemicals. The choice of the raw material pretreatment influences the whole process. Several pretreatment methods can be applied consecutively mostly including a physical step for setting up the size of the materials. Some of the pretreatment methods already hydrolyze a part of the lignocellulose; some methods deliver lignocellulose already fractionated into the main compounds and the condition of the material after pretreatment ranges from solution over slurry to dry mass. If it has not been conducted during pretreatment, the next step of the process is hydrolysis. Choosing a separate fermentation of cellulose and hemicelluloses requires an additional another fractionation to be carried out before fermentation. Dependent on which chemicals have been applied, a neutralization or cleaning session has to be interposed before microorganisms can start fermentation. The simultaneous saccharification and fermentation (SSF) process combines the 2 stages of hydrolysis and fermentation. The end product ethanol is then purified through distillation or filtration until the desired quality grade is reached.

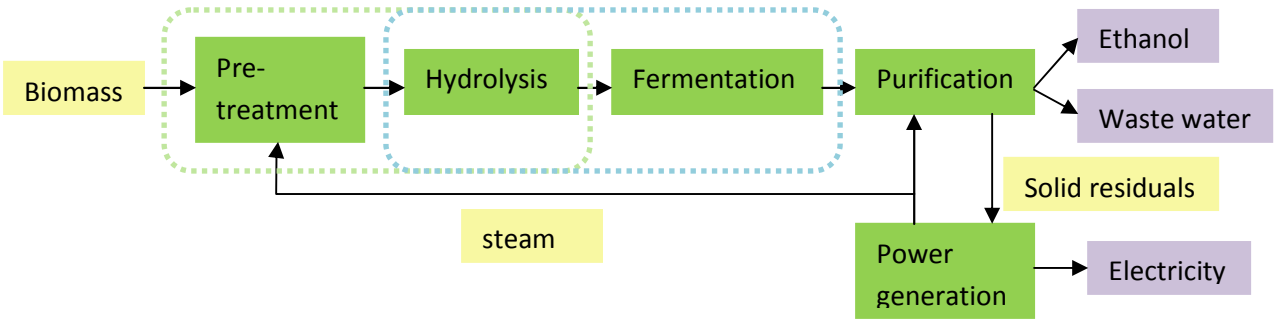

Figure 15: Flow diagram of an ethanol production process

3.6.1. Pretreatment

The choice of pretreatment is perhaps the most important step which influences every following process step as there are hydrolysis, fermentation, downstream processing and wastewater handling.

Native lignocellulosic materials are resistant to enzymatic attack by natural barriers. The most promising method of hydrolysis of cellulose to glucose is to use enzymes. To make the raw material accessible to enzymes, pretreatment is necessary [56].

The best method for pretreatment strongly depends on the type of lignocellulose. As discussed in the previous chapter, every type of feedstock requires a different kind of pretreatment for optimal results [49]. The various pretreatment methods give different types of materials which have to be further processed.

Decreasing the crystallinity of cellulose, enlarging its accessible surface area, reducing the protective layers of lignin and hemicellulose, decreasing the degree of polymerization of cellulose and decreasing the degree of acetylation of hemicellulose are the most important goals of pretreatment. Furthermore the process should feature a low energy demand, low operation costs and environmental sustainability [49].

Methods

Classification of these pretreatment methods is not definite. Several described methods would also have the full eligibility to be classified under a different item. Water and steam are not considered as chemical agents and therefore pretreatment methods with steam as main active substance were not classified as chemical methods. Furthermore, borders between steam pretreatment, autohydrolysis, and acid pretreatment are fluent.

a) Physical methods

All physical methods are targeted in increasing the surface area using different methods. In most cases the power consumption is extremely high to reach a good state for the following process step which is hydrolysis. In some cases the energy input during physical pretreatment is even higher than the theoretical energy content from the biomass [56].

- **Mechanical treatment**

Chipping, grinding, milling or a combination of this methods are applied for the comminution of the lignocellulosic in order to reduce cellulose crystallinity and enlarge the surface. The desired sizes vary between one millimeter and several centimeters [57].

- **Pyrolysis**

Cellulose and hemicellulose thermally convert to into fermentable sugars achieving good yields. When the lignocellulosic material is treated at temperatures above 300°C it decomposes to gaseous products and char [53].

- **Irradiation**

  - Gamma rays

The irradiation of cellulose with gamma rays causes the cleavage of the β-1,4-glycosidic bonds which results in a larger surface area and lower crystallinity [58]. Although this method is known and researched since the 80's, it is still far from being used in full-scale processes because of high costs [56].

  - Microwaves

Microwaves irradiation is based on the thermal effect caused by microwaves in aqueous surrounding. Internal heat is generated by vibration of polar bonds. In inhomogeneous materials such as lignocellulosic biomass, the concentration of polar bonds is restricted to specific areas and cause there explosion effects among particles and destroys structures of lignocellulose [30].

  - Electron beam

The electron beam irradiation is a non-thermal irradiation method. Activated by a continuously changing magnetic field from electron radiation, the polar bonds are stimulated to vibrate. This vibration accelerates the chemical degradation by decreasing the degree of polymerization and crystallinity of cellulose[30].

b) Chemical methods

- **Acid pretreatment**

Known since the 19th century, acid pretreatment achieves high yields of sugars from lignocellulosic biomass. Acid pretreatment is based on the use of sulfuric, nitric or hydrochloric acids and aims to expose cellulose for oxidation. Two main operation modes are widely used: dilute acid pretreatment which involves high temperatures and low acid concentrations and concentrated acid pretreatment which means operation at low temperatures at high concentrations [53].

  - Dilute acid

Dilute-acid hydrolysis is probably the most common method among the chemical pretreatment methods. It can be applied as pretreatment for hydrolyzation or as the actual method of hydrolyzing to fermentable sugars. This treatment generally involves mineral acids such as HCl and H_2SO_4 [49].

Methods for dilute acid treatment can roughly be divided into 2 different processes:

i) Low loading with solids (5-10 w%), high temperature (>160°C) and continuous flow mode
ii) High loading with solids (10-40 w%), lower temperature (<160°C) and batch mode [53].

At low concentration of acid (e.g. 0,1-1% H_2SO_4), this treatment can achieve high reaction rates and high cellulose and hemicelluloses hydrolysis. Almost 100% hemicelluloses removal is possible and only a small fraction of lignin is dissolved.

Dilute hydrochloric acid showed a similar high efficiency in the hydrolysis of the biomass as sulfuric acid, but HCl is more corrosive to the equipment [49].

- Concentrated Acid

Chemical pretreatment with concentrated acids allows operation at low temperatures and pressures. Sulfuric acids are usually used, but also processes with hydrochloric acid, nitric acid trifluoroacetic acid (TFA) were successful. Treatment with concentrated acid removes cellulose and hemicelluloses from the solid biomass. The residual solid has a high content of lignin and nearly no other byproducts like degradation products occur. The optimal acid concentration depends on the choice of the acid and ranges from 41% with HCl, to 71% with H_2SO_4 and 100% with TFA. Acid recovery is an important step regarding process costs. HCl and TFA are easier to recover than H_2SO_4. Another disadvantage is the difficult protection of the equipment of corrosion [59].

- **Alkaline Hydrolysis**

The very regular and cross linked matrix of lignocellulosic matrices is a very efficient defense against penetration of enzymes to the fibers. Alkaline treatment causes a swelling of the pores of lignocellulosic material which increases the cellulose digestibility. Conversely to acid hydrolysis, alkaline pretreatment are very effective for delignification and exhibit only limited solubilization of cellulose and hemicellulose [59].

Alkaline chemicals such as sodium hydroxide, potassium hydroxide, calcium hydroxide and ammonia, which are widely used, provoke the cleavage of aryl ether linkages in lignin. This permits the cellulose to swell beyond normal water-swollen stages [49]. This process is followed by a saponification of intermolecular ester bonds that crosslink hemicelluloses and other components. As a result, the pore size, the intraparticle porosity and the capillary size are increased [59].

NaOH is the most common chemical used for the treatment of lignocellulosic biomass to enhance the digestibility. It acts as a strong swelling agent and changes the crystalline structure of cellulose I to cellulose III [49]. Because of the relatively mild conditions with low pressures and temperatures ranging from ambient to 120°C, reactor costs are lower than those of acid technologies [31].

For softwood species, which contain a large amount of lignin, the success of alkaline pretreatment is negligible or not existent [56]. The use of lime instead of sodium hydroxide is especially suitable for agricultural residues and will be described in a following section.

- Ammonia based pretreatment methods

Ammonia is an efficient delignification reagent. Therefore ammonia is widely used in various pretreatment methods such as ammonia fiber explosion (AFEX), ammonia recycled percolation (ARP) and soaking in aqueous ammonia (SAA) [60]. The various pretreatment methods strongly interdigitate and therefore a clear classification is impossible. Focusing on the reagent, the AFEX method would also perfectly fit to this section, but the method is additionally relatable to the physicochemical methods section, where it is described.

i) Ammonia-recycled percolation (ARP) pretreatment

The ARP is conducted in a percolation reactor with preheated liquid ammonia in aqueous solution (5-15 w%) through the substrate at temperatures up to 180°C and high pressure [61]. The ARP process solubilizes about half of xylan from the hemicellulose but retains more than 92% of the cellulose [62]. The degree of delignification is up to 63% and the resulting glucan in the solid can be hydrolyzed by enzymes to near completion [61]. Treatment with ammonia in aqueous solution at high temperatures results in solution of lignin via an ammoniolysis reaction. These conditions have virtually no effect on carbohydrates. The low lignin content increases the accessibility of cellulase to the cellulose. Additionally, lignin is toxic to microorganisms and adsorbs enzymes and the removal of lignin diminish the negative consequences such as low enzyme efficiency, high dosage and costs [63].

ARP was initially introduced to enhance the enzymatic digestibility of hardwoods and was then successfully extended to corn stover and grass pretreatment [63] .The application to softwood, which contains more lignin, is less effective [56].

ii) Soaking in aqueous ammonia (SAA)

The SAA method is a batch pretreatment process with lower severity than ARP. To pretreat the biomass more effectively, harsher reaction conditions like adding hydrogen peroxide or elevated temperature and concentrations would be required in the SAA which would induce high processing costs [60].

- Lime pretreatment

Calcium hydroxide (lime) is used to pretreat wheat straw, poplar wood, switchgrass, corn stover and similar agricultural residues. Besides the lignin, this pretreatment also removes acetyl and various uronic acid substitutes on hemicelluloses [53]. Main advantages of this process are the moderate and therefore economic operation conditions regarding temperature and pressure. Lime is, compared to NaOH and KOH, a cheap chemical which has less safety requirements. A limitation occurs in the reagent recovery because some alkali is converted into irrecoverable salts [59].

- Alkaline hydrogen peroxide (AHP)

The addition of an oxidant (mostly H_2O_2) to alkaline pretreatment with lime or sodium hydroxide can improve the performance [59]. The alkaline solution of H_2O_2 reacts with lignin and forms products of low molecular weight and high solubility in water [64]. AHP is applied in batch mode or in

combination with other pretreatment processes such as steam explosion, hydrothermolysis and SAA [59].

In this method, lignocellulosic material is soaked in an alkaline solution (pH 11,5 with NaOH) which contains hydrogen peroxide for a time range between 30 minutes to several days [65].

AHP has been successfully applied to corn stover, barley straw, wheat straw, soft wood and various herbaceous and woody plants at continuous flow operation at high biomass loading (40% solids) and low H_2O_2 loading. Research on improved pH control, peroxide recycling and stabilization could further improve the performance of AHP treatments [66].

- **Organosolv process**

Organic solvent or organosolv processes are an effective pretreatment for lignocellulose as preparation for fermentation with the additional option of isolating the lignin for further processing. In this approach aqueous-organic solvent with or without catalysts is added to the lignocellulosic biomass and removes the lignin fraction and, depending on reaction conditions, a specific part of the hemicelluloses fraction. Solvents commonly used in this process are ethanol, methanol, ethylene glycol tetrahydrofurfuryl alcohol, dimethylsulfoxide, peracetic acid, acetone, phenols, and ethers [67]. Some of those substances are explosive , highly inflammable and therefore difficult to handle. Additionally, an inorganic acid catalyst such as H_2SO_4 or HCl [56] or organic acids (oxalic acid, salicylic acid and acetylsalicylic acid) can be used to reduce the operating temperature or enhance the delignification process. If the reaction temperature is above 180°C, the addition of catalysts is unnecessary [67].

It is important to remove the used solvents properly from the cellulosic material because these solvents act as inhibitors for the following fermentation. The solvents are drained from the reactor, evaporated, condensed and recycled [57].

- **Ozonolysis**

Ozone is an effective oxidant which is soluble in water and easily accessible. During ozonolysis mainly the lignin polymer is degraded, but also hemicellulose is slightly solubilized. Ozone is highly reactive towards conjugated double bonds and functional groups with high electron densities. In contrast to cellulose and hemicelluloses, lignin has a high content of C=C bonds which are attacked by the ozone [68].

Reactions for ozonolysis treatment are carried out at room temperature and ambient pressure and do not produce any toxic residues. Therefore it would be possible to minimize the environmental pollution by a deliberate process design. One severe disadvantage of this method is the large amount of ozone required which produces high process costs [57].

- **Ionic liquids**

Many recent publications about lignocellulosic biomass pretreatment [69–71] focus on pretreatment with a rather new class of substances called ionic liquids. Ionic liquids (IL) are salts composed of a

large organic cation and a small inorganic anion. The melting points of ILs are generally quite low and most ILs are liquid at room temperature [72]. Their solvent properties can be changed by adjusting anion and cation constituents. ILs can be designed with a very low volatility and high thermal stability to simplify recycling. Cellulose can be fully dissolved by ILs [73]. The most up-and-coming ionic liquids are based on ethyl, methyl or butyl immidazolium cations with halides, acetates or methyl phosphates as anions [72].

Before this new branch of biomass pretreatment can be applied to industrial scale, further research is needed.

c) Physicochemical methods

- **Steam explosion**

In this process lignocellulosic biomass is rapidly heated by high-pressure steam at 160-260°C and held for a certain time at this condition. Due to a sudden decrease in pressure the condensed moisture evaporates (explodes). This thermal expansion breaks the structure of fibers in the biomass. Beside this physical effect, hemicellulose is hydrolyzed by the acetic and other natural acids released during the steam pretreatment. Water itself also acts as acid at elevated temperatures [74]. Steam pretreatment without explosion step is referred to as autohydrolysis.

Steam pretreatment with pristine water steam involves no costs for recycling or environmental preventive measure. Therefore it can be considered as the most cost-effective option for hardwood and agricultural residues, but not for softwood. For softwoods, steam pretreatment is only effective with additional acid catalysts such as H_2SO_4, SO_2 or CO_2 to reach high sugar yields [36].

- Sulfur dioxide

SO_2 is a promising additive for steam explosion since it requires milder reaction conditions and therefore much less expensive reactor material, generates less gypsum and produces more material with high fermentabiltiy as comparable additives. One major disadvantage of SO_2 is its high toxicity and the high safety and health risks involved [53].

- Ammonia fiber explosion

Ammonium fiber explosion (AFEX) is a combination of a steam explosion process and an alkaline pretreatment method with ammonia. In this process, lignocellulosic biomass is treated in bath mode with liquid anhydrous ammonia at temperatures between 60 – 140°C at high pressure. This pressure is kept for a certain time and then abruptly relieved which results in a rapid expansion of the ammonia gas followed by a physical disruption of the biomass fibers [73].

Ammonium fiber explosion (AFEX) treatment results in the decrystallization of cellulose, partial depolymerisation and deacetylation of hemicelluloses, cleavage of lignin-carbohydrate complex linkages, lignin C-O-C bond cleavage, increase in accessible surface area because of structural disruption and increased wettability of the treated biomass [75].

In contrast to other physicochemical pretreatment methods such as steam explosion where slurry is produced, AFEX produces only solid material with a dry mass recovery of 100%. AFEX is very well established for herbaceous and agricultural residues, but its efficiency for hardwood is limited and for softwood AFEX is not attractive.

One drawback of this process is the ammonia recovery and the costs involved for recycling and safety requirements [59].

- Carbon dioxide explosion

Supercritical CO_2 is considered as green solvent because its non-toxicity, the process does not produce any harmful materials and its easy recovery after extraction [76].

The explosion treatment follows the same scheme as steam explosion treatment: the lignocellulosic biomass is treated at high temperatures and high pressure with a supercritical CO_2 and effects destruction of the fiber structure by a quick pressure relief followed by expansion of the CO_2. Despite many advantages as higher conversion yields, the supercritical CO_2 process is too expensive for industrial application [36].

- **Liquid hot water treatment**

Compressed hot water at temperatures from 170-230°C at pressures above 50 bar is used to hydrate cellulose and remove hemicelluloses and parts of lignin [30]. This method is similar to steam pretreatment, but lower temperatures and lower solid content are used.

Advantages of this method are the high xylose recovery, no addition of any acid or chemical and the environmental compatibility.

- **Wet oxidation treatment**

As wet oxidation treatment the treatment of biomass with water and air or pure oxygen at temperatures above 120°C is referred to. In some cases alkaline catalysts are added. All three factions of lignocellulosic biomass are affected in this process. This method is only effective for biomass with low lignin content because the yield decreases with increasing lignin content [56].

d) Biological methods

Another method to pretreat lignocellulosic material is to use microorganisms that degrade lignin, hemicelluloses or cellulose. Among several fungi such as brown rot fungi and soft rot fungi, white rot fungi are the most effective microorganisms for pretreatment of lignocelluloses. White rot fungi attack hemicelluloses and lignin, whereas brown fungi attack only cellulose and soft rot fungi both cellulose and lignin [30].

This method is very environment friendly because of its low energy requirement, no chemical requirement and mild conditions. But one main feature that distracts this method from being widely applied is the treatment rate which is far too low for industrial use.

Comparison

Crystallinity of cellulose, lignin structure, hemicellulose structe and active surface area were the most important points discussed in chapter 3.6.1 Pretreatment. The previous techniques described affect at least one of these factors and facilitates therfore the following process steps. Generally, high pH methods selectively solubilize lignin, whereas acid pretreatment tend to solubilize hemicellulose [63].

Table 2 shows a comparison of different pretreatment methods for corn stover. All methods showed an amelioration of digestibility to more than 90% compared to untreated biomass. But the product compositions as well as reaction times are very different and the suitable method has to be chosen according to energy demand, operation conditions and further processing.

Method	Temperature [°C]	Reaction time [minutes]	Used chemical	Glucan [%]	Xylan [%]	Lignin [%]	Conversion* [%]
Untreated corn stover	-	-	-	31,6	21,4	17,2	23,3
Dilute Acid	160	20	Sulfuric acid	59,3	9,5	22,5	91,1
LHW	200	24	water	76,1	4,8	7,1	95,5
AFEX	90	15	ammonia	36,1	21,4	17,2	96,0
ARP	170	10	ammonia	61,9	17,9	8,7	90,1
Lime	55	4 weeks	CaO	52,7	16,2	25,2	93,0

Table 2: Comparison of the effect of different pretreatment methods for corn stover [63]
***Digestibility after 72 hours for an enzyme loading of 15 FPU/g cellulose in the original feedstock**

For agricultural residues a large number of pretreatment techniques reach high sugar yields whereas possibilities to pretreat woody biomass, especially softwood, are limited. Acid hydrolysis and steam pretreatment with acid catalysts, two methods with high equipment cost and formation of inhibitors during treatment, are suitable for all kind of lignocellulosic biomass [56].

3.6.2. Hydrolysis and Fermentation

Hydrolysis

In this step the complex carbohydrates are converted to monomers:

$(C_6H_{10}O_2)_n + nH_2O \rightarrow nC_6H_{12}O_6 \rightarrow$ HMF → Formic Acid + Levulinic Acid

Hemicellulose→ Xylose + Arabinose + Galactose + Mannose + Glucose + acetic acid → *HMF + Furfural* → *Formic acid + Levulinic Acid*

Undesired degradation products during hydrolysis are printed in italic script. This reaction is catalyzed by dilute acid, concentrated acid and enzymes.

Whereas lignin removal and hemicellulose hydrolysis are commonly classified as pretreatment, cellulose hydrolysis is considered as the major hydrolysis step. Hydrolysis without preceding pretreatment step would reach yields under 20%, whereas yields after pretreatment often exceed 90% [31].

a) Acid Hydrolysis

Acid hydrolysis involves the exposure of lignocellulosic biomass to an acid for a defined period of time at a specific temperature. This results in sugar monomers from cellulose and hemicellulose via a complex heterogeneous reaction.

Hydrolysis

Acid hydrolysis is applied in the so-called two-stage acid process in dilute and concentrated version, following the acid pretreatment (Figure 16).

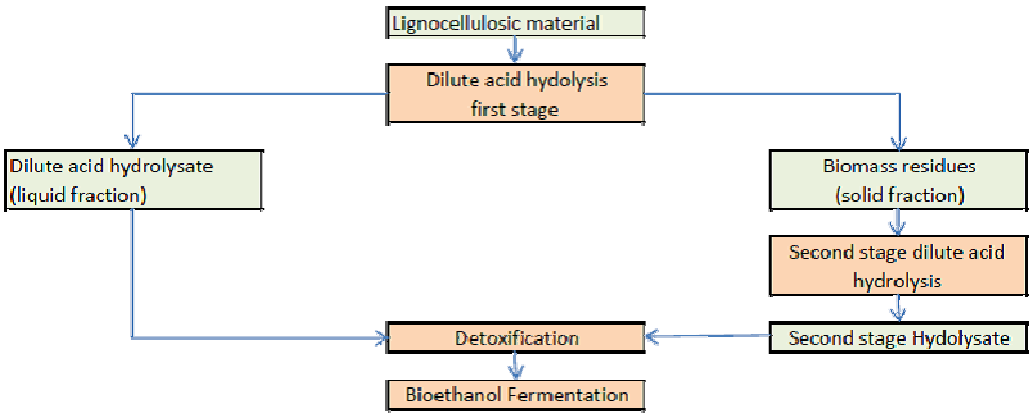

Figure 16: Flow diagram of the hydrolysis process of lignocellulosic material

The first stage is conducted under mild conditions (170-190°C) and mainly hydrolyses hemicellulose. If the reaction would continue, the sugars would further react into different products, mainly furfural and hydroxymethylfufural (HMF). This does not only reduce the sugar yield, these side products additionally inhibit the fermentation process. Therefore in the first stage the pentoses are produced and isolated. In the following second stage, the remaining solids were treated under harsher operating conditions (200-230°C) to recover the hexoses [31]. Yields are 70-98% for xylose, galactose, mannose and arabinose, but only 50% for glucose [77].

Cleaning

Furfural, hydroxymethylfurfural and acid, the main degradation products formed during pretreatment and hydrolysis, together with acid from acid pretreatment and hydrolysis are toxic or inhibit the fermenting microorganisms. Therefore these undesired compounds have to be removed.

For some processes, depending on the acid concentration, acid recycling is necessary for an economic performance. The acid is exchanged by ammonia in continuous ion exchange and is recovered. The remaining low acid concentration in neutralized with lime. Gypsum is formed, precipitates and is filtered from the sugar solution. On average, 0,02 kg gypsum per kg feedstock is

formed which has to be disposed or is used to some extend as agricultural soil conditioner. A process without acid recovery produces even 0,6-0,9 kg /kg feedstock [31].

b) Enzymatic Hydrolysis

Enzymes are able to catalyze the breakdown of polysaccharides to monomer sugars for further fermentation to ethanol. Enzymatic reactions are highly specific, therefore no degradation ore by-products occur as observed with acid hydrolysis. Enzymatic hydrolysis is an environmental friendly alternative which takes place at mild conditions (pH 4,8 and temperatures between 45-50°C), does not evoke corrosion problems with reactor materials and waste treatment costs are low [78].

Enzymatic hydrolysis is carried out by enzymes which are highly substrate specific. This cellulase enzyme is a complex mix of enzymes which work synergistically and where each enzyme attack typical parts of the hemicellulosic and cellulosic fibers.

Cellulose hydrolysis

Cellulase enzymes involve endo-, exoglucanase and β-glucosidase. Both endo- and exoglucanases hydrolyze β-1,4-glycosidic bonds from of cellulose fibers in low crystallinity regions, but while endoglucanase randomly cleaves bonds at accessible cellulose chains and produces chain ends, exoglucanase progressively cleaves sugar monomers at chain ends [53]. β-glucosidase cleaves liberated cellobiose to glucose. Therefore, β-glucosidase is strictly speaking no cellulase, but its role is very important since cellobiose inhibits many cellulases. β-glucosidase is inhibited by glucose. Since most enzymes are end product inhibited, the rate of enzymatic hydrolysis decreases rather quickly. The maximum cellulase activity was measured at about 50°C and a pH between 4-5. The optimal conditions strongly depend on the enzyme source and residence time [77].

Hemicellulose hydrolysis

Hemicellulose contains the different sugar units xylan, glucan, mannan, arabinan and galactan. This sugar variety explains why hemicellulitc enzymes are more complex than cellulases and consist of a mixture of at least eight enzymes. The enzymes endo-1,4-β-D-xylanase, exo-1,4- β-D-xylocuronidase, α-L-arabinofuranosidase, endo-1,4-β-D-mannase, β-mannosidase, acetyl xylan esterase, α-glucuronidase and α-galactosidase are involved to form pentoses and hexoses [30].

While the number of enzymes involved in hemicellulose hydrolysis is much greater, the accessibility is easier than in cellulose hydrolysis because xylan does not form tight crystalline structures [53].

Enzyme production

Filamentous fungi are the main source of cellulase and can be found in various species such as Trichoderma, Penicillium, Aspergillus, Fusarium, Phanerochaete, Humicola and Schizophillum. The most efficient cellulase producing organism is Trichoderma. It produces a complex mix of enzymes, but it lacks β-glucosidase. This can be compensated by addition of Aspergillus which is a very efficient β-glucosidase producer [30].

Compared to fungi, cellulolytic bacteria only produce a small amount of enzymes. Species of Clostridium, Cellulomonas, Thermonospora, Bacillus, Bacteriodes, Ruminococcus, Erwinia, Acetovibrio, Microbispora and Streptomyces are able to produce cellulases, but fungi are more promising because of their aerobic growth and the good production. However, enzymes are still a cost intensive part of ethanol production rate [31].

c) Fermentation

Successful pretreatment and hydrolysis result in a mixture of various 5C and 6C sugars in monosaccharide and oligosaccharide form. For industrial production, microorganisms should efficiently convert all sugars to ethanol.

According to the following reactions, a theoretical yield of 0,51 kg ethanol is possible per kg glucose and xylose.

$3\ C_5H_{10}O_5 \rightarrow 5\ C_2H_5OH + 5\ CO_2$

$C_6H_{12}O_6 \rightarrow 2\ C_2H_5OH + 2\ CO_2$

Microorganisms such as bacteria, yeasts and fungi can convert sugars to ethanol. Saccharomyces cerevisiae is the most common used industrial fermentation microorganisms and is also known as baker's yeast, but it cannot ferment pentose sugars. Considering that pentose sugars represent up to 20 % of all sugars in lignocellulosic, an efficient xylose developing microorganism should be done.

Because of the sugar mixture, diauxic growth and different reaction rates are observed. Generally, microorganisms prefer glucose, galactose, xylose and arabinose in this order. Hexoses can be converted within a few hours; the conversion of xylose lasts for two to three days. Because of this different properties and fermentation rate between glucose and xylose, process design is difficult [61].

Comparably with cellulose, xylose can be metabolized by bacteria, fungi or yeast. Only a few yeast species such as Pachysolen tannophilus, Candida shehatae and Pichia stipsis metabolize xylose efficiently. Wild-type strains of the most common fermentation yeast, saccheromyces cerevisiae, cannot convert pentoses into ethanol, but xylose using S. cerevisiae derived by metabolic engineering achieves high ethanol yields [36].

Some species of anaerobic bacteria are able to ferment pentoses, but they are inhibited by already low sugar and ethanol concentrations. Additionally, they produce a wide variety of by products which reduce the ethanol yield. Efforts have been made to obtain recombinant strains of bacteria such as Escherichia coli, Klebsiella oxytoca and Zymomonas mobilis by introducing ethanologenic genes [46].

3.6.3. Processes

Various levels of process integration involving enzymes were developed for the next step of processing lignocellulose.

Separate Hydrolysis and Fermentation (SHF)

SHF is the most rudimental mode to produce ethanol. In this case the pretreated biomass is hydrolyzed by enzymes and is subsequently fermented in a glucose fermentation reactor. This configuration produces a mixture of ethanol and unconverted xylose. To make use of the hemicellulose fraction, a second fermentation step is necessary to ferment xylose to ethanol (Figure 17). This step can also be located parallel to glucose hydrolysis and fermentation (Figure 18) [31]. In both process schemes the enzyme production is not included and therefore another reactor and at least one further process step is required.

Summing up, the SHF process is split into distinct process steps for enzyme production, cellulose hydrolysis, glucose fermentation and xylose fermentation. This offers the possibility to optimize the operation conditions and microorganisms for each process step appropriate.

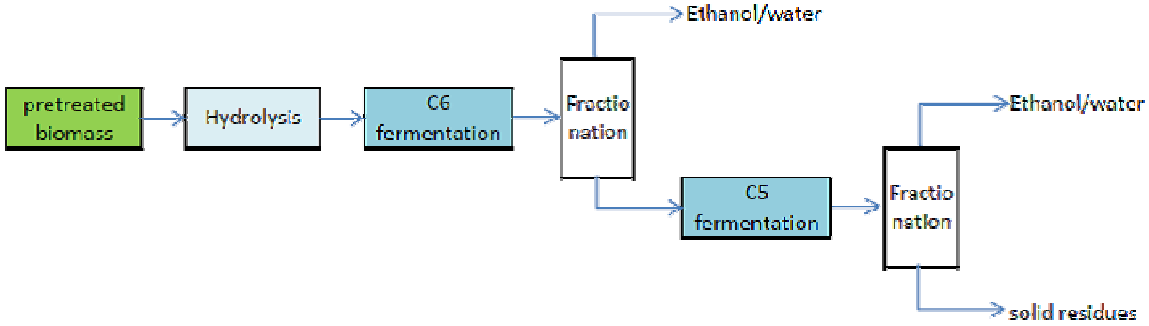

Figure 17: SHF scheme with subsequent hemicellulose conversion

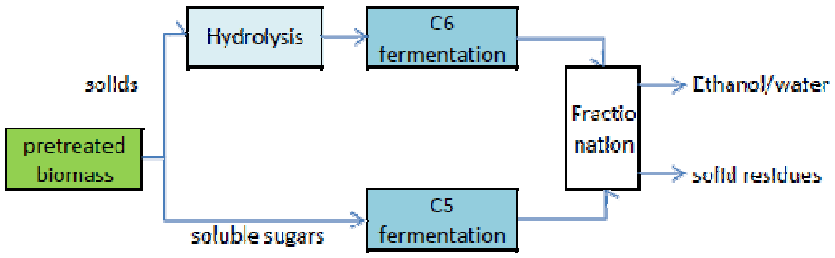

Figure 18: SHF scheme with parallel hemicellulose conversion

Simultaneous Saccharification and Fermentation (SSF)

During the SSF process, the cellulose hydrolysis and glucose fermentation steps are conducted together in a single reactor (Figure 19). Beside the advantage of having combined two process steps in one vessel, this configuration results in faster reaction rates and higher product yields compared to

the SHF process. The reason for this is the inhibition of cellulase by glucose which is formed by cellulase from cellulose. The rapid conversion of glucose to ethanol avoids this hindrance and additionally protects the mixture from unwanted microorganisms [78].

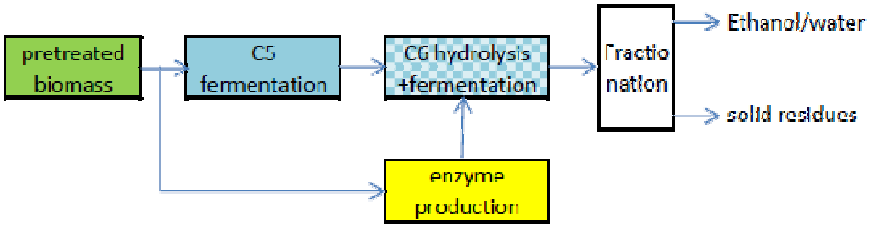

Figure 19: The Simultaneous Saccharification and Fermentation process

An important upgrade to the SSF process was developed with the Simultaneous Saccharification and Cofermentation process (SSCF). In former processes fermentation of the hemicellulose fraction is either neglected or performed separately, the SSCF process employs microorganisms which are able to ferment xylose and glucose. Excluding enzyme production, only one process step is required to convert the pretreated biomass to ethanol [79] (Figure 20).

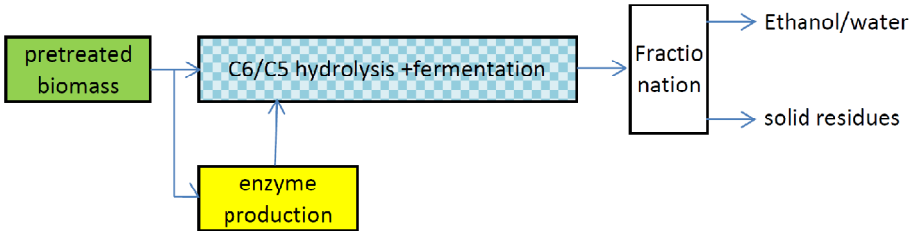

Figure 20: The Simultaneous Saccharification and Cofermentation process (SSCF)

Direct microbial conversion (DMC)

Direct microbial conversion (DMC), also known as Consolidated Bioprocessing (CBP), combines all necessary process steps after lignocellulose pretreatment in a single reactor including enzyme production (Figure 21). Microorganisms which hydrolyze lignocellulose and ferment sugar to ethanol at the same time are grown during the process. Examples of these microorganisms are bacteria such as Clostridium thermocellum and fungi including Neurospora crassa, Fusarium oxysporum and Paecilomyces sp. Because of low yields and poor reaction rates this process is still far from being efficient [30].

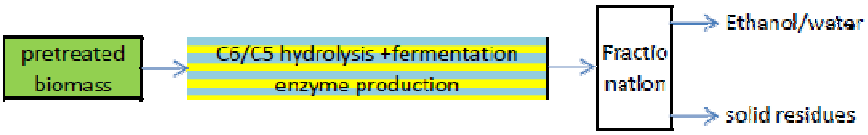

Figure 21: Direct microbial conversion (DMC)

3.7. Development status

Currently, production costs for lignocellulosic ethanol are 2,5 to 3 times higher than for ethanol derived from starch or sugar containing plants, which implies that second generation ethanol is economically not yet competitive to first generation ethanol [80]. A significant amount of the production costs accounts for the supply with enzymes. Compared to the thermochemical route, the biochemical process generates higher operating costs due to the high enzyme cost, but has the advantages of higher ethanol production and lower investment cost [54]. In recent years, great efforts have successfully been made to reduce the enzyme loading resulting in a significant reduction of the enzyme cost [80,81]. Another approach in order to decrease production costs is to upscale production facilities [80]. The plans for the commercialization of lignocellulosic ethanol in the US are ambiguous. Several plants were targeted to start the commercial production in the coming years, but some schedules had to be changed due to ramifications of the financial crisis in the last decade on the funding. The majority of the existing ethanol production plants in Europe are demonstration facilities with a few exceptions like planned plants in Crescentino, Italy, Hull, UK and Sweden [82]. Cellulosic ethanol producing plants are often placed directly on site of plants producing first generation ethanol or mills. This allows benefiting from existing infrastructure and short distances if the feedstock is produced on site. Some companies already produce ethanol from lignocellulose as side product during specialty cellulose in Norway or lumber production in Canada.

3.8. Conclusion

Significant progress has been made in the past decade in the conversion of lignocellulosic biomass to ethanol. The specific structure of lignocellulosic material was successfully investigated and is now well understood and process schemes were developed and implemented, but still there is much room for further development.

To be a competitive technology, cost and energy input for each process step have to be reduced despite growing prices for fossil energy carriers. One promising possibility to realize these ambitious goals represents biotechnology. Robust organisms that can be easily cultivated and are able to hydrolyze all kind of hardly pretreated cellulose containing biomass and convert it to ethanol at high yield without byproducts at room temperature would be ideal. Further research in biotechnology will lead to a realistic approach to the described all-in-one microorganism followed by a successful commercialization of the bioethanol from lignocellulose process.

4. Electrocatalysts for the EOR

Parts of this literature survey were submitted for publication [254].

As already pointed out in previous chapters, the direct oxidation of ethanol proceeds via multiple pathways and intermediates. The high number of atoms increases the number of electrooxidation steps and creates a network of reactions leading to different products. Catalysis plays an important role in order lead the molecule to the desired complete oxidation which gains the maximum of energy.

Much literature has been published in the last few years on catalysts of the ethanol oxidation reaction, but the focus has mainly been on platinum group metals in acidic media [83–92].

Generally, the oxidation mechanism follows a dual reaction scheme with one pathway leading to complete oxidation and the second to partial oxidation [83]. Following pathway 1, the ethanol molecule is oxidized after adsorption on the catalyst surface via two adsorbed C_1 species to carbon dioxide (Figure 22). In pathway 2, the partly oxidized molecule is desorbed before the C-C bond is broken, resulting in acetaldehyde and acetic acid as partially oxidized products. Subsequently, these desorbed molecules diffuse into the bulk electrolyte and since the contact to the electrode surface is lost, further oxidation to CO_2 is very improbably [93].

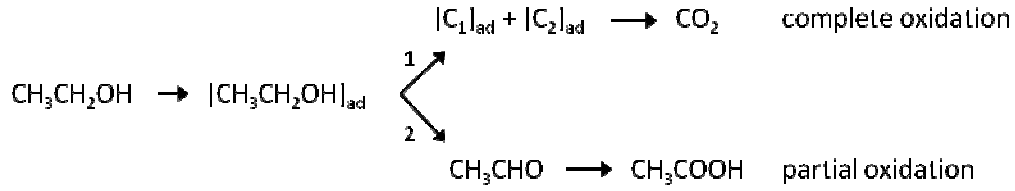

Figure 22: Reaction pathways of the EOR

The reaction mechanisms, and therefore the rate-determining step, are strongly dependent on the catalyst system and the pH chosen. Furthermore, the catalyst surface structure, the applied potential and the ethanol concentration influence the composition of the products [89]. There are some controversies in literature regarding the structure of the adsorbed species and the further oxidation mechanism, particularly of pathway 2 [83]. Even if the focus is only at Pt electrodes in acid environment, different electrode surface structures and different measurement methods led to several detailed reaction mechanisms and identification of the adsorbed species proposed by researchers [86,94]. The main products produced by oxidation of ethanol on Pt or Pt alloy catalysts in acidic environment are acetaldehyde, acetic acid and only a small amount of carbon dioxide [95].

Pure Pt is not the most suitable catalyst for the EOR [83]. The surface of pure Pt electrodes is quickly covered by poisoning, strongly adsorbed species such as carbon monoxide resulting from the splitting of the C-C bond in ethanol. The addition of ruthenium or tin as cocatalysts attenuates the problem of poisoned catalyst surfaces and slightly increases the kinetic of the EOR [96]. Ru and Sn atoms on the Pt surface facilitate the oxidation of strongly adsorbed species by delivering sufficient oxygen atoms in order to oxidate the adsorbed molecule but do not enhance the scission of the C-C bond [83].

A different successful approach to increase the reaction kinetic is to establish the reaction in alkaline media. The EOR is facilitated by the higher concentration of hydroxide adsorbed on the electrode

surface which is involved in the oxidation of surface adsorbed species and generally higher current densities can be achieved [97]. In acid media, only Pt and Pt alloys exhibit the necessary stability during fuel cell operation. Alkaline environment allows the employment of nonnoble metal catalysts and oxides [98]. Among pure unsupported metals, Pd exhibits the highest activity towards the EOR in alkaline media [99]. On Pd- and Pt-based catalysts, the rate determining step is the removal of adsorbed ethoxy species and the main product is acetate. Detailed reaction mechanisms for these catalytic materials have been proposed by several researchers [92,100]. For further increase of the catalytic activity, promoting metals such as Pb, Tl, Ru, Sn, Au, Bi and Cu were successfully added to Pd and Pt based electrodes [99]. Additional positive effects concerning the poisoning of the catalyst surface were achieved by introduction of metal oxides such as CeO_2, NiO, MgO and ZrO_2. The promoting effect of these oxides has the same cause as addition of Ru; the oxides ensure an oxygen enriched catalyst surface [99]. The product distribution of Pt based catalysts is basically the same as in acid environment, with the main products acetaldehyde and acetic acid, and a slightly increased amount of CO_2 [92]. Pd is only elctrocatalytic active towards the EOR in strongly alkaline environment and oxidizes ethanol selectively to acetate with no acetaldehyde as byproduct [100].

The key to control the reaction and particularly the formation of adsorbed intermediates are the catalytic properties of the electrode material [85] and hence it is a prerequisite to identify the processes on the electrode surface in order to align the reaction to complete oxidation. This literature review intends to show alternatives to the conventional platinum-ruthenium catalyst for use in alkaline direct ethanol fuel cells.

In recent years, research on platinum-free catalysts has been booming, but the literature on platinum-free catalysts for alkaline DAFCs has mainly concentrated on oxygen reduction where non-noble multimetallic components were applied and studied [101–103]. Pt-free catalysis of the EOR on Pd in alkaline media has been well-researched and documented [100,104]. Some research has been conducted on the basis of Ru [105–107] and Rh [108] EOR catalysis. For the EOR catalysis by other metals, a vast number of publications are available. However, due to different measuring techniques, catalyst morphologies, and support materials, comparisons are difficult. This review proposes nickel, gold, and compounds based on them as the most promising alternatives to platinum group metals. Other metals such as silver and cobalt are only discussed as additives to nickel and gold, since there is no literature available demonstrating catalytic activity towards the EOR by these pure metals. In order to significantly improve the activity for ethanol oxidation, a fundamental understanding of the main features and characteristics of the metals involved must be achieved, and their interactions with the morphology and supports must be understood. The main properties of each promising catalyst material in heterogeneous catalysis and electrochemistry are introduced to identify the origin of the material's catalytic activity and to point out possibilities and directions for enhancement of its performance. All potentials quoted in this paper refer to the RHE unless otherwise stated.

3.1. Gold

3.1.1. General

To better understand the catalytic properties of gold, a few of its chemical and physical properties are explicated, allowing us to draw important conclusions regarding chemisorption and oxidative potential. The outrageous characteristics of gold concerning resistance to oxidation and corrosion have been very well known for several centuries, and it is therefore commonly used in jewelry and coinage. Together with its two homologs, copper and silver, these metals are often called “coinage metals” [109].

Gold has the atomic number 79 with atomic configuration $[Xe]4f^{14}5d^{10}6s^{1}$ and is found in the Ib group of the periodic table of elements [109]. It is a very noble element [110], with a redox potential ε_0 of +1,69 for Au/Au^{3+}[111] due to its high electron affinity, which is greater than that of oxygen. Gold is the most electronegative metal and is the only metal that does not react directly with sulfur, oxygen, and other electronegative elements. Dissolution of gold is only possible by strong oxidizing or complexing agents [111].

Unlike other group Ib metals, gold can assume a wide range of oxidation states. Gold commonly occurs in the oxidation states +1 and +3, but chemical compounds with Au(II) and Au(V) are also found. Three stable types of monohalides exist, but the bond with fluoride is unstable because of its strong electro negativity. Due to this negativity, another oxidation state has been documented: the auride anion with the oxidation state -1 [111].

Gold is known as the least reactive metal, but this inertness is not because of an inability to form chemical bonds. Gold forms very stable alloys and intermetallic compounds with many other metals such as copper, aluminum, tin, and titanium [110]. Like all coinage metals, gold has a full d-band and therefore a full antibonding orbital. This evokes surface repulsion of potential adsorbates like oxygen or hydrogen [112]. Compared with silver and copper, the electron orbital overlap is very high. When the average number of bonds between gold atoms decreases, as is the case for surface atoms, this orbital overlap decreases and the band structure is weakened [113]. If the number of low coordination surface atoms is high enough, chemisorption on the surface is possible. This explanation of the discrepancy of reactivity between bulk gold and small gold particles in the 1980s led to a boom in research on catalysis by gold [114].

3.1.2. Heterogeneous catalysis

Gold has been considered chemically inert and therefore a poor catalyst. The reason for this error was that gold was studied mostly in bulk form until 1975. In the 1980s, catalysis of the oxidation of CO by metal oxide-supported gold was discovered [115]. Another important progress was the finding of the catalytic activity of small gold particles for the hydrochlorination of ethyne, which is used for industrial production of vinyl chloride [116]. These advances in catalysis by gold renewed interest, and several new reactions were successfully explored [109,116–120]:

- Low temperature oxidation of CO
- Hydrochlorination of ethyne
- Water gas shift reaction
- Selective hydrogenation
- Hydrogen peroxide production
- Reduction of Nitric and Nitrogen Oxides
- Methanol synthesis
- Complete oxidation of hydrocarbons
- Selective partial oxidation
- Epoxidation of propylene

The catalytic performance of gold is influenced by three major factors:

- Size of gold particles

Because of the importance of the particle size, preparation methods for supported catalysts came to the fore. Traditional impregnation methods as used for PGMs do not allow synthesis of particles below 10 nm, because gold has a lower melting point than Pt and Pd, and calcination requires high temperatures which would lead to coagulation of gold. This coagulation is distinctly enhanced by the chloride ion descended from the $HAuCl_4$ precursor [121].

- Type of support

The selection of the support material is strongly dependent on the reaction that should be catalyzed. For CO oxidation, semiconductive materials like TiO_2, NiO, Co_3O_4, and Fe_2O_3 are suitable, as well as the insulating metal oxides Al_2O_3 and SiO_2. Not only is the choice of metal oxide important, but the crystal lattice of the support material decides whether the oxidation of hydrocarbons by Au/TiO2 is selective or not [122].

- Gold/support Interface

The strong interaction between catalytic interactivity and the preparation method was investigated in the well-explored reaction of CO oxidation on Au/TiO_2 [121,123]. In contrast to Pt or Pd, the preparation method of the gold catalyst made a significant impact on the resulting activity of the catalyst. Surprisingly, not only was the gold particle size crucial for high turnover frequencies, but the contact structure between the gold particle and the metal oxide was important too. The gold must be attached to the support material as a hemispherical particle to achieve the highest activity. This implies that the reaction takes place at the perimeter interface between gold and metal oxide [121].

3.1.3. Electrocatalysis in aqueous alkaline media

Gold as an electrocatalyst results in an enhancement of electrical conductivity, because of the lower electrical resistance compared to platinum [124]. In many cases, the activity of gold in alkaline media is clearly higher than that of platinum, mainly due to the fact that gold is not as susceptible as platinum to surface poisoning species [125]. The electrochemistry of gold in aqueous solutions is complex, since it involves several kinds of deposits, monolayers, and oxide formation.

$$2Au + 3H_2O \rightarrow Au_2O_3 + 6H^+ + 2e^- \qquad E_0 = 1{,}457\,V \quad for\ hydrated\ oxide$$

$$E_0 = 1{,}511\,V\ for\ unhydrated\ oxide$$

$$Au_2O_3 + H_2O \rightarrow AuO_2 + 2H^+ + 2e^- \qquad E_0 = 2{,}630\,V \qquad [126,127]$$

The activity of gold as a catalyst increases with pH [128]. In alkaline media, gold is covered with OH^- ions before it is converted to oxides at higher potentials. This coverage is involved in catalytic interactions with organic substances [129]. The adsorption energy of OH^- ions on gold is clearly lower than on platinum, which leads to diminished inhibition [130]. The polarity of the OH_{ads}^- bond in relation to the gold surface decreases with the charge of the electrode. The polarity of the OH_{ads}^- bond on positively charged gold electrodes is considerably lower than on negatively charged surfaces [131]. Because of this polar character, the adsorption can be regarded as a partial charge transfer reaction:

$$Au + OH^- \leftrightarrows Au - OH_{ads}^{(1-\lambda)} + \lambda e^- \qquad [132]$$

The charge transfer coefficient λ varies between 0 for a completely nonfaradaic case and 1 for a completely faradaic case. The adsorbed hydroxide species exists predominantly in the hydrated state [132]. The presence of chemisorbed OH_{ads}^- ions strongly affects the catalytic ability of gold catalysts towards oxygen reduction, oxidation of hydrogen and organic molecules [131].

A cyclic voltammogram of a gold electrode in alkaline solution (see Figure 23) reveals some peculiar electrocatalytic properties of gold. Compared to platinum, the most striking difference is the absence of a hydrogen adsorption region in both alkaline and acidic media. In acidic media, the double layer region of gold expands in a potential range from 0 to 1,3 V. The oxidation peaks in acidic and alkaline media strongly resemble each other, with the only difference being that the oxidation region, which consists of several positive peaks at 1,1 to 1,3 V [133], is shifted positively in acidic media. Oxygen desorption is visible as a single negative peak at 1,1 V [134].

The formation of a monolayer of oxide on the electrode surface starts at lower potentials than quoted in standard listings, due to the increased activity of surface atoms as compared to the bulk gold atoms for which these values were generated [127]. Hysteresis between oxide monolayer formation and desorption can be observed. The reduction appears at a lower potential with a sharp peak, compared to the oxidation peak at slightly higher potentials in plateau form. This hysteresis is caused by electrochemical processes after the electron transfer step, e.g. exchange of surface dipoles with adsorbed species and repulsion forces during the oxide growth [127]. These hydrated oxides have a low density compared to bulk gold oxides. Therefore, disruptions in the metal lattice and

irregularities must be expected. After oxide formation, oxygen gas evolution starts in both acidic and alkaline media at 1,6 V [126].

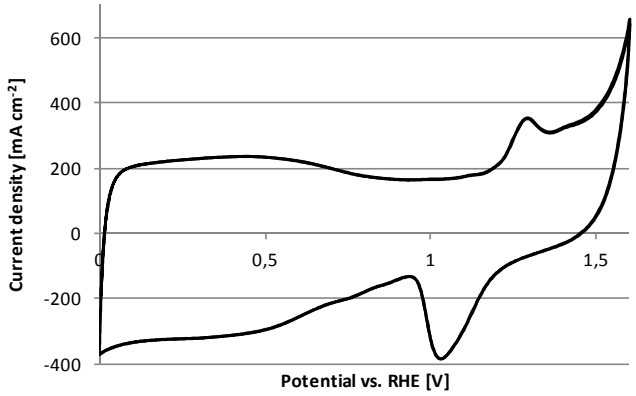

Figure 23: CV of a carbon-supported gold catalyst in 0,1 M KOH with scan rate 50 mV/s

Due to the lack of a hydrogen adsorption region, oxidation peaks are mainly used to determine the actual surface area of gold electrodes. In one monolayer of gold oxide, an electric load of 386 µC per actual cm^2 is charged [135].

The growth of an oxide film on Au in alkaline media is strongly dependent on the potential applied and the time that the metal is exposed to high potentials. At potentials up to 1,8 V, the oxide film grows to a limited thickness of one monolayer of AuO, or $Au(OH)_x$ as the hydrated form. This initial oxide formation is slow and starts with OH chemisorption originating from the OH^- ions of the alkaline solution. If potentials higher than 2 V are applied, three additional oxidation states occur that result in films of unlimited thickness on the initial AuO film. The outermost film layer then has a chemical composition of $Au(OH)_3$ [136].

Compared to dry conditions, gold also shows a high affinity for CO electrooxidation in alkaline aqueous media. The catalytic process is initially controlled kinetically, but with increased anodic polarization it changes to diffusion control [137].

As seen in the preceding chapter, during heterogeneous catalysis by gold the monomolecular structure of the catalyst and support material have a great influence on the activity and properties of the catalyst. A greater roughness of the gold surface, as produced by electrodispersion or decomposition of gold amalgam, causes an additional methanol oxidation peak which cannot be detected on smooth electrodes [138]. The surface structure of gold is therefore decisive for the reactive activity because it influences OH^- adsorption and oxide layer formation [139].

The influence of the surface structure can also be explained by the existence of two different kinds of surface atoms with different electrochemical behaviors. Equilibrated, highly coordinated gold surface atoms with full d-orbitals have a lower tendency to catalyze reactions than metastable gold surface atoms with a low lattice coordination number and only partially filled d-orbitals. A high number of metastable surface atoms implies a high number of active sites. Since these metastable atoms undergo oxidation at less positive potentials, this phenomenon is also referred to as premonolayer oxidation [140].

Active sites on the surface can be generated by roughening the electrode using gold nanoparticles and codeposition, or by alloying with additional metals.

3.1.4. Electrooxidation of organic compounds

Gold exhibits considerable activity towards the oxidation of alcohols within the potential range between 0,4 and 1,3 V [141]. Compared with other noble metals such as Pt, Pd, and Rh, gold shows a higher oxidation activity, but at a rather high potential range [142].

Alcohols such as

- Aliphatic alcohols including:
  - Methanol [132,139,143]
  - Ethanol (see next chapter)
  - propanol [141][129]
  - Butanol [142]
- Polyols including ethylene glycol [144,145], glycerol [146,147], and sugars [148,149]
- Aldehydes
  - Formaldehyde [150,151]

Generally, the activity and product distribution are strongly dependent on the pH and the nature of the electrolyte. This is due to the reaction pathway in alkaline media where alcohols are deprotonated because of the acidity of the alcohol group, which is believed to be the reactive species during alcohol oxidation [147].

$$H_\beta R - OH_\alpha + OH^- \leftrightarrow H_\beta R - O^- + H_2O \qquad [143]$$

The resulting alkoxy compound is much more reactive than alcohols. The increased activity of the oxidation reaction in alkaline media is therefore conditioned not only by the metal used as a catalyst. With methanol, unsaturated alcohols, and alcohols functionalized with fluoride as exceptions, the oxidation activity of organic compounds increases with decreasing pK_a values because of this deprotonation step [125]. The alkoxide reacts further with the hydroxide, which can be adsorbed as a partially charged anion on the gold surface or in solution.

Aldehydes are not stable in alkaline media and can react with the corresponding carbonic acid if proton acceptors such as positively polarized gold or molecular oxygen are present [125], or if the intermediate stays adsorbed and is further oxidized on the catalyst surface [152].

The onset potential of alcohol oxidation is slightly dependent on the concentration of the alcohol. The oxidation of 2-propanol starts earlier at higher concentrations [130]. The oxidizability is strongly dependent on the chain length of the alcohol and the substituents on the α-carbon atom. The

oxidation current of secondary alcohols is higher than that of primary alcohols and it increases linearly with the chain length [130]. Methanol oxidation is an exception to this rule because ethanol oxidation on gold is 8 times faster [130]. The oxidation current is inversely dependent on the pK_a; the oxidation currents decrease with increasing pK_a, again with methanol as an exception [125].

The substituents of the α-carbon atom have a great influence on the binding energy of the C_α-H bond. The C-H bond in methanol is stronger than that of other alcohols [143]. For methanol, fluorinated compounds, and formaldehyde, the first charge transfer originated by the OH^- assisted C-H bond break is the rate-determining step [151]

Hydroxide adsorption greatly affects the catalytic activity of gold. The presence of CO on Au (111) surfaces promotes this step. The methanol oxidation reaction is enhanced and the onset potential is lowered. For ethanol and glycol oxidation, no promoting effects due to CO adsorption are observed [143]. CO adsorption facilitates the adsorption of OH^- on the catalyst surface, which plays a significant role in the oxidation of alcohols. A similar stronger OH^- adsorption effect can be created by increasing the roughness of the gold surface. The activity of gold is highly sensitive to the shape and size of its crystallites. The artificial formation of holes and edges creates positions with low coordination numbers, which promotes the adsorption of OH^- [138,153].

The potentials at which methanol oxidation can be observed on gold electrodes strongly depend on its crystallographic orientation, while the magnitude of the oxidation current achieved is similar. This confirms that the surface structure of gold, and as a consequence OH^- adsorption and oxide layer formation, are important factors influencing methanol oxidation [139]. Methanol oxidation on gold electrodes does not suffer any significant poisoning effects from adsorbed CO [132]. Adsorption of hydroxides and oxide formation on the electrode surface overlap with methanol oxidation and contribute to the rate-determining factors [132]. As in the case of glycerol, the gold catalyst is completely inactive under acidic conditions. In alkaline media, glycerol is converted to glyceric acid and immediately oxidized further to glycolic and formic acid [147]. Gold catalyzes the regioselective oxidation of galactose to galactonic acid in alkaline media under mild conditions. The oxidation starts at lower potentials, as on Ni or Pt, and proceeds at low concentrations as a first order reaction [149]. The decay of the gold catalyst is more pronounced in reactions where a C-C bond cleavage occurs than in reactions such as the ethanol oxidation with no C-C dissociation [154].

3.1.5. Electrooxidation of ethanol

The main products of the EOR on bulk gold are C_2 compounds, since gold does not break the C-C bond. At low pH, the EOR is negligible. With increasing pH, the oxidation currents arising from surface oxidation increase as well as those from ethanol oxidation, strengthening the general thesis of a strong interaction with surface oxides [125].

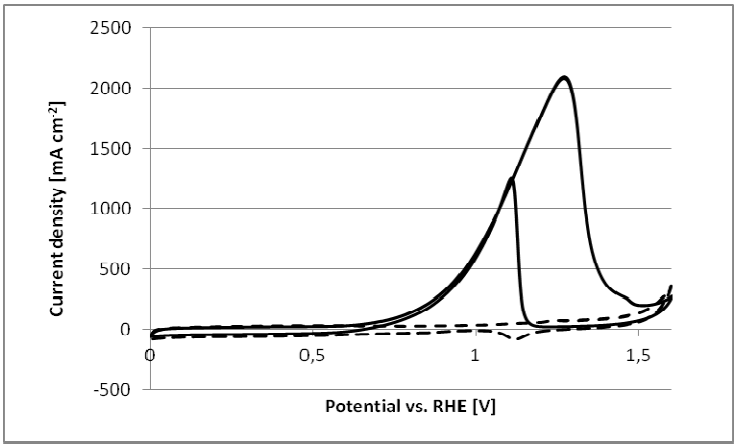

Figure 24: CV of a carbon-supported gold catalyst in 0,1 M KOH und 0,5 M Ethanol (solid line) and in 0,1 M KOH (dashed line) with scan rate 10 mV s^{-1}

In a 0,1 M KOH solution the EOR starts between 0,6 and 0,7 V, depending on the electrode material, and reaches its peak at around 1,15 V, well before surface oxidation starts (Figure 24). The EOR peak on the backward sweep nearly coincides with the reduction peak of surface oxides, and reaches its maximum when the surface reduction is finished. Measured on metallic gold surfaces, no hysteresis between the forward and backward scan can be observed, which implies that no adsorbing species inhibit the EOR on gold [128]. If a supported gold catalyst is used, the oxidation current density on the backscan is clearly lowered due to a higher capacitive current, as compared to bare metals [256].

In contrast to a Pt electrode in acid, the current densities from the EOR on a gold electrode increase with the reactant concentration [152]. An increased ethanol concentration results in increased current densities until a concentration of around 2 M ethanol is reached, followed by a reduction of the current density when the concentration is increased further [152]. At low ethanol concentrations the current density increases linearly with the concentration [155]. Upon further reduction of the ethanol concentration, the total current on the backscan of a CV can be negative, because of the superimposed oxide reduction which has a higher reaction rate [133]. Compared to the EOR in alkaline media on platinum, the reaction rate on gold is slower [133].

During chronoamperometric ethanol oxidation, the oxidation current reaches its maximum just at the beginning of electrolysis and then decreases steadily. This can be explained by electrode deactivation due to passivation and by the decrease in ethanol concentration [133]. The number of electrons exchanged per ethanol molecule was experimentally quantified as 4,25. The main product of the EOR is acetate (see formula below) and except for a small amount of carbonate, no further reaction products can be detected after ethanol electrolysis on gold in alkaline media [133].

$$CH_3CH_2OH + 5\,OH^- \rightarrow\ CH_3COO^- +\ 4\,H_2O + 4\,e^-$$

Although the mechanism of the EOR on gold has been studied by several research groups [133,152], there are still open questions due to contradictory results and interpretations.

1) Adsorbed species

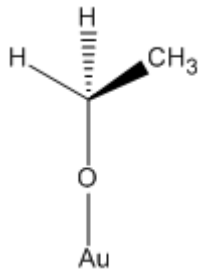

Figure 25: Adsorbed ethoxy group on gold surface

The initial adsorbate on the electrode surface has never been identified directly, but thermodynamic considerations reveal a higher stability of the Au-O bond compared to Au-C, in contrast to platinum electrodes where Pt-C is preferred. Therefore there is a high probability that an ethoxy group is the initial adsorbate (see Figure 25) [152]. During this adsorbtion, one molecule of water and one electron are already produced.

2) Interaction with OH^-

The next step of the EOR involves the interaction of the adsorbed ethoxy group with a hydroxide anion via nucleophilic elimination of one proton, which immediately reacts in alkaline solution to produce water. Due to the strong influence of pH on electrocatalysis [125] and heterogeneous catalysis [156,157], the important role of the hydroxide ion during the EOR is obvious. This hydroxide can be in solution [152], which would indicate an Eley-Rideal (ER) mechanism, or adsorbed on the electrode surface (Figure 26) [133] according to the Langmuir-Hinshelwood (LH) mechanism.

The increased inhibition of the EOR at higher potentials due to the oxidation of hydroxide ions adsorbed to gold oxides points to an LH mechanism [158]. Furthermore, the reaction rate of the oxidation of aliphatic alcohols increases with increasing chain length [130], and secondary alcohols are oxidized faster than their primary homologues [133]. For a reaction following an ER mechanism, a decrease in the reaction rate would be expected due to increasing steric hindrance of the reaction.

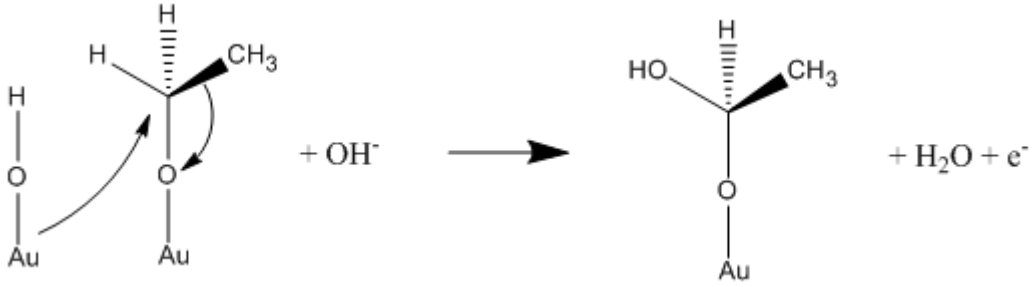

Figure 26: Reaction with hydroxide adsorbed on the electrode surface

3) Oxidation to acetate

Further oxidation to the final product proceeds very quickly via interaction with hydroxide ions in solution (shown in Figure 27). This step has no influence on the reaction rate [152].

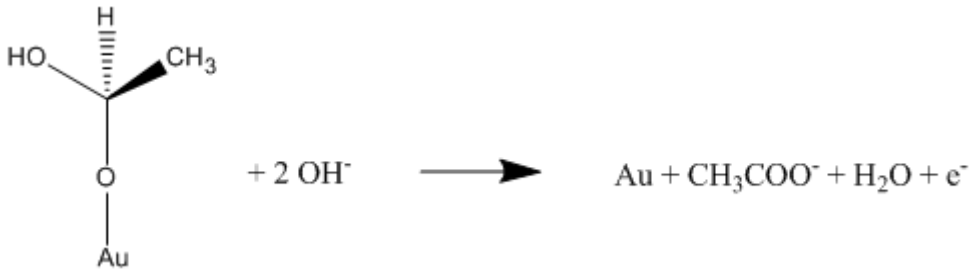

Figure 27: Oxidation to acetate

As pointed out in previous sections, the morphology of the gold electrode is extremely important. It can be changed, and the EOR enhanced, by using support materials such as zeolites [159] or TiO_2 nanotubes [160], enlargement of the active catalyst area with nanoparticles [161–163] or synthesis techniques [155], or the introduction of additional metals [140,144] or electron-conducting polymers [164].

When the deposited amount of gold is increased, it begins to agglomerate like silver and the particle diameter increases. This effect is caused by coalescence during the growth of gold clusters and is due to atom diffusion on the carbon substrate [148].

Incorporation of small amounts of the non-PGM metals Ag, Pb, Bi, Cd, and Tl in the gold electrode strongly affects the onset potential of electrocatalytic oxidation of several organic compounds. The presence of Ag [165], Pb, or Bi [144] on the catalyst surface causes a negative shift in the onset potential without any change in the current density. With Cd and Tl systems, the overvoltage is also slightly reduced, but the current density suffers a large decrease [144]. The addition of lead to the gold electrode allows control of the surface morphology. Inclusion of Pb ions increases the surface area of the electrode, but this does not necessarily improve performance as a catalyst. In alkaline solutions the active sites of gold can become overoxidized and inhibit the elctrocatalytic reaction [140].

3.1.6. Comparison of potentials and peak currents of the EOR on gold in the literature

Comparison of different catalyst materials in a literature review is nearly impossible since different scan rates, treatments of the catalyst before the experiments, and electrolytes can change the results of the experiment considerably. Additionally, experimental methods diverge and results are not always quoted in the same units. Table 3 aims to give an overview of the materials researched so far and their performance.

Table 3: Comparison of achieved current densities with gold catalysts in the literature. In the case of several published values under different conditions in one paper, the highest was chosen
***value determined from a graph because not given in the text**
[+]not included in Figure 36 and Figure 37 because of incomplete information in the publication

Onset P [V]	Peak P [V]	Peak j [mA cm^{-2}]	catalyst	Electrolyte	Scan rate [mV s^{-1}]	
0,6	1,25	2,4	gold beads	0,1 m NaOH 0,5 M EtOH	50	[128]
0,538	1,225	5,8	gold disk	1 M KOH 1 M EtOH	5	[146]
0,75*	1,14	0,25	Au/GC	1 M NaOH, 0,1 M EtOH	50	[163]
0,8*	1,2*	8,7*	single crystal gold bead	0,15 M NaOH 0,5 M EtOH	20	[143]
1	1,3	8 mA (no j)	gold grid	0,1 M NaOH 0,1 M EtOH	50	[133]
	0,18* (Ag/AgCl)	1,1	gold zeolite modified graphite	0,5 M NaOH 0,5 M EtOH	50	[159][+]
0,6	1,15	6*	Polycrystalline gold disk	0,1 M KOH Up to 2 M	100	[152]
-0,3 SCE	0,15 SCE	0,7* mA (no j)	Mesoporous gold electrode	0,5 M NaOH 0,4 M EtOH	100	[155]
-0,33 HgO	0,377 HgO	1,348	Au nanoparticles on carbon support	0,1 M KOH 0,1 M EtOH	20	[154]
-0,34 SCE	0,28 SCE	3,5	Au-PANI	0,5 M NaOH 1 M EtOH	100	[164]
0,6	1,15*		20% Au/C	1 M NaOH 1 M EtOH	1	[166]

4.2. Nickel

4.2.1. General

Nickel has the atomic number 28 with the electron configuration [As]$3d^8 4s^2$ and is therefore in the transition metal group VIIIb, together with its homologs palladium and platinum [111].

Nickel exists in the oxidation states -1, 0, +1, +2, +3, and +4, and builds compounds with oxygen, hydrogen, halogens, cyanide, sulfur, and organic ligands. The most stable and therefore most common oxidation state, particularly in aqueous media, is +2 [111]. Typical nickel salts ($NiSO_4 \cdot 7\ H_2O$ and $Ni(NO_3)_2 \cdot 6\ H_2O$) have a bright green color due to their hydrated Ni^{2+} complexes ($Ni(H_2O)_6^{2+}$) [167].

The solubility of nickel hydroxide is very low, therefore it is impossible to obtain a nickel ion-containing solution in alkaline media [168]. Nickel hydroxide acts as a base at moderate pHs [111].

In addition to the very well documented and examined nickel hydroxides, which are important for energy storage in batteries, nickel forms several compounds with oxygen [111]. Annealing of nickel salts forms NiO, which can be oxidized to Ni_3O_4 and Ni_2O_3. Ni^{4+} can be obtained by oxidation from $Ni(OH)_2$ with $S_2O_8^{2-}$ as the dioxide $NiO_2 \cdot x\ H_2O$ [111].

The ferromagnetic metal crystallizes in two allotropic structures. α-Ni has a closely packed hexagonal structure and β-Ni is face-centered cubic [167].

In aqueous environments nickel dissolves in acidic media according to

$$Ni \rightarrow Ni^{2+} + 2e^-$$

and in strong alkaline media to

$Ni + 2\ H_2O \rightarrow HNiO_2^- + 3H^+ + 2e^-$ [167]

At negative potentials below -0,5 V, nickel is stable even at low pH. At potentials higher than -0,5 V and pHs higher than 6, Nickel builds up a passive layer and does not dissolve. Due to this passivation, nickel is stable in strong alkaline solutions even at high anodic potentials, while it quickly corrodes in acidic environments [167].

Nickel has been broadly applied in electrochemical storage systems since the invention of alkaline batteries such as the Edison accumulator and the nickel-cadmium battery at the end of the 19th century. Because of its popularity as an electrode material, its electrochemical properties have been well explored [167,169]. The redox couple $Ni(OH)_2$/NiOOH is widely used as the positive electrode material for rechargeable batteries [168].

4.2.2. Heterogeneous catalysis

Besides the application of nickel for energy storage in various electrochemical devices, nickel is also used as a catalyst for a broad range of processes in the petrochemical, chemical, and automotive industries. It is used in metallic form as in Raney nickel or in supported forms with classical support materials such as Al_2O_3, SiO_2, zeolites, or carbon. Nickel catalyzes the hydrogenation of a large number of organic functional groups as well as dehydrogenation, hydrogenolysis, and cracking of hydrocarbons [170].

4.2.3. Electrocatalysis in aqueous alkaline media

Nickel placed in contact with alkaline solutions immediately forms a layer of $Ni(OH)_2$. The exact potentials at which this reaction takes place are strongly dependent on the pH and can be identified from a Pourbaix diagram [167]. At higher potentials, the oxidation state of nickel changes continuously with the potential between +2 and +3 [171].

$$\alpha - Ni(OH)_2 + OH^- \leftrightarrow \gamma_2 - NiO(OH) + H_2O + e^- \qquad E_0 = 1{,}38\,V \text{ [172]}$$

$$\beta - Ni(OH)_2 + OH^- \leftrightarrow \beta - NiO(OH) + H_2O + e^- \qquad E_0 = 1{,}45\,V \text{ [172]}$$

Two modifications of nickel hydroxide are known: α-$Ni(OH)_2$ and β- $Ni(OH)_2$ [172]. α-$Ni(OH)_2$ does not belong to a well-defined structure type, and α-$Ni(OH)_2$ represents a large set of disordered Ni(II) hydroxides [173]. α-$Ni(OH)_2$ is not stable in alkaline solution and converts irreversibly to β-$Ni(OH)_2$ (sometimes called β_{bc} meaning badly crystallized [174]). The α-$Ni(OH)_2$ phase lacks hydroxyls and contains intercalated anions and water. The general formula of this α-$Ni(OH)_2$ is $Ni(OH)_{2-x}A^{n-}_{x7n} \cdot yH_2O$ with x=0,2-0,4; A=nitrate, chloride, carbonate or sulfate and y=0,6-1 [174]. β-$Ni(OH)_2$ is isomorphous with $Mg(OH)_2$, or brucite, and crystallizes in a hexagonal form [173].

Nickel hydroxide does not form large, well shaped crystals. Depending on the experimental conditions, α-type hydroxides are the main product of electrodeposition and most precipitation reactions. The β-form can be achieved via further conversion by aging or specific synthesis routes [173].

The hydroxide layers formed in alkaline media exhibit p-type semiconductive properties with low conductivity [175,176]. α-$Ni(OH)_2$ is an electronic isolator, its capacitance increasing with the thickness of the deposit [176]. Oxidation of the hydroxides leads to a higher conductivity [172]. NiOOH is a good mixed conductor since high mobility for both ionic species and electrons is provided [175].

Oxidation leads to Ni^{3+} and Ni^{4+} oxides with several oxide compositions equivalent to $NiO_{1,75}$ [172]. β-NiOOH is a well-defined material and crystallizes like the β-nickel hydroxide, closely packed in a hexagonal system. It can be derived from β-$Ni(OH)_2$ by removing one electron and one proton. The structure can be described as NiO_2 with intercalated protons. In contrast to β-$Ni(OH)_2$, β-NiOOH is a hydrogen-bonded structure with no free hydroxyl groups [173]. Proton diffusion into the $Ni(OH)_2$

lattice is a crucial step in the mechanism of oxidation to NiOOH [177]. With the conversion of β-$Ni(OH)_2$ to β-NiOOH, the water content of the layer increases [178].

γ-NiOOH is the name of a large group of Ni oxide compounds with a large inter-sheet distance. The general formula is $A_xH_y(H_2O)_zNiO_2\ with\ x, y \leq 1$ and A representing alkali ions like Na^+ and K^+, and with water molecules intercalated between NiO_2 sheets. The valance state of nickel is clearly higher than 3 and is estimated to be around 3,75 [173,179]. γ-NiOOH compounds crystallize in rhombohedral systems with similar hexagonal parameters. Among γ-NiOOH compounds, the differentiation between γ_1-NiO(OH) and γ_2-NiO(OH) is used depending on the synthesis route. γ_1-NiO(OH) exhibits higher crystallinity due to its synthesis by hydrolysis of highly organized sodium or potassium nickelates as compared to γ_2-NiO(OH), which is produced at room temperature from Ni^{2+} solutions or by oxidation of α-$Ni(OH)_2$ [173].

Aging of β-NiO(OH) and rapid oxidation of β-$Ni(OH)_2$ in alkaline solution result in γ-NiO(OH) phase formation. During β- $Ni(OH)_2$ oxidation, γ-NiO(OH) is not the main product because this would require a structural change. The intercalation of water molecules, ion exchange, and a sheet glide all pose a higher energy barrier than the oxidation to β-NiO(OH) [173]. If γ_2-NiO(OH) is reduced, α-$Ni(OH)_2$ is formed.

The oxidation of α-$Ni(OH)_2$ in alkaline media occurs at slightly lower potentials than β-$Ni(OH)_2$ [172]. A similar effect can be observed during the reduction of nickel oxy-hydroxides, where the reduction of γ-NiO(OH) occurs before the highly ordered and closed packed β-NiO(OH) forms. The low phase stablilities in α and γ-phases are due to higher intersheet distances and disorder [173]. The intersheet distance for α-$Ni(OH)_2$ is 8,05 Å and 7,2 Å for γ-NiO(OH) [180]. Metallic nickel oxidizes in the following order (all possible modifications): Ni→ α-$Ni(OH)_2$→ β-$Ni(OH)_2$→ β-NiOOH→ γ-NiO(OH) [178] (see Figure 28).

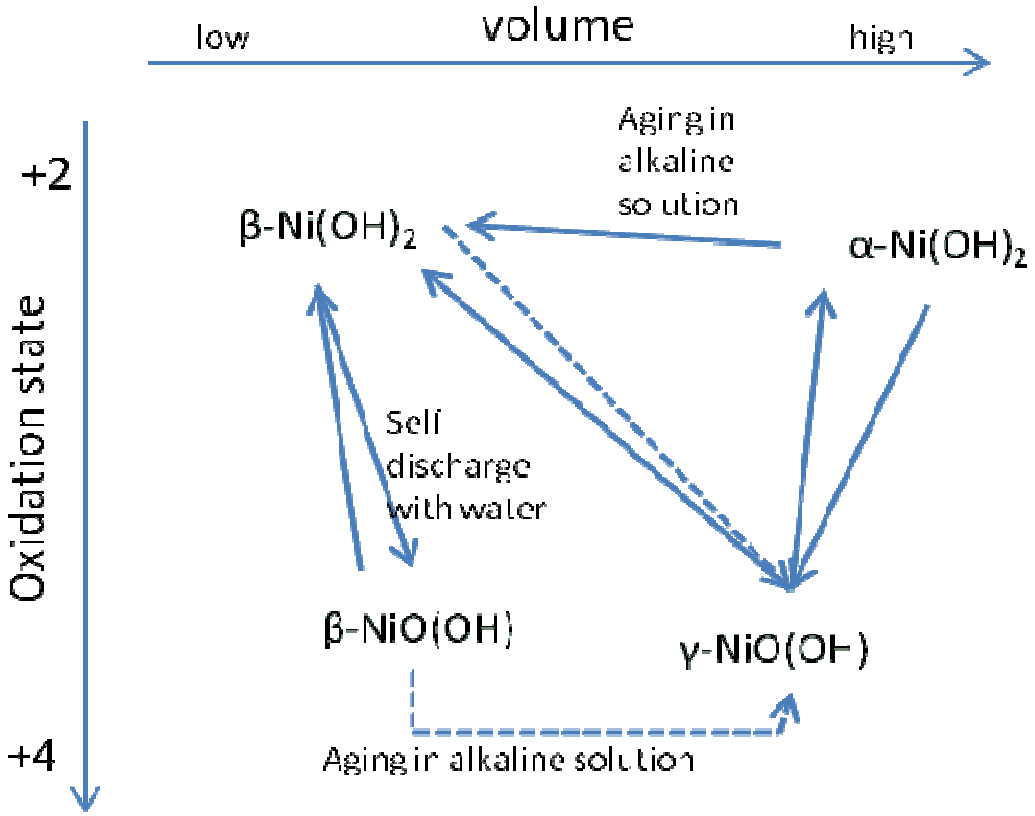

Figure 28: Influence of changes in the oxidation state on the volume of nickel catalysts during phase transitions [181]

Transition between the phases is also accompanied by a considerable volume change, caused by altered crystal order and interlayer distances (Figure 6). An electrochemically deposited Ni electrode exhibits a α-structure, but in contact with alkaline solution the electrode cracks and a volume decrease become visible with AFM [180]. The electrodes ages and converts to β-$Ni(OH)_2$ which is more closely packed. This volume decrease can also be observed during oxidation to the oxohydrate form [180]. The crystallographic change involved in the conversion of β-$Ni(OH)_2$ to β-NiO(OH) is very small due to similar intersheet distances (4,6 Å and 4,7 Å), therefore the volume change is small [175].

The reduction reactions known as “self-discharge reactions” are particularly interesting for use in energy storage:

$$2\,\beta - NiOOH + H_2O \rightarrow 2\,\beta - Ni(OH)_2 + \frac{1}{2}O_2$$

$$2\,\beta - NiOOH + H_2 \rightarrow 2\,\beta - Ni(OH)_2$$

The electrochemical properties of Ni are extremely dependent on the pretreatment, and cyclovoltammograms are sensitive to scan rate, range, and return potentials. Slight modifications in the measurement setup can result in different peak phenomena [177,182]. Irreversible changes take place on the electrode surface even under potentiostatic control [183]. Figure 7 shows possible compositions of passivation films in different media.

If a metallic nickel electrode is placed in air, it passivates with a thin layer of nonstochiometric oxides and hydroxides (Figure 29). This passivation film is semiconductive and allows the reduction and oxidation of water with certain overpotentials, but further oxidation of the nickel surface is not possible because the oxide film hinders the transport of reagents to the metal. This oxide layer can be removed to a certain extent in aqueous media by applying a potential negative enough to reduce water. The evolving hydrogen reduces the nickel surface [168]. For a complete removal of the oxide layer, it must be treated mechanically and kept in an oxygen-free atmosphere. Due to the impossibility of removing these layers electrochemically, applying spectroscopic and electrochemical techniques with access to a defined reference state is difficult [178]. Even mechanically, ultrasonically, acid, and electrochemically treated nickel electrodes exhibit a NiO layer of 10 Å [184].

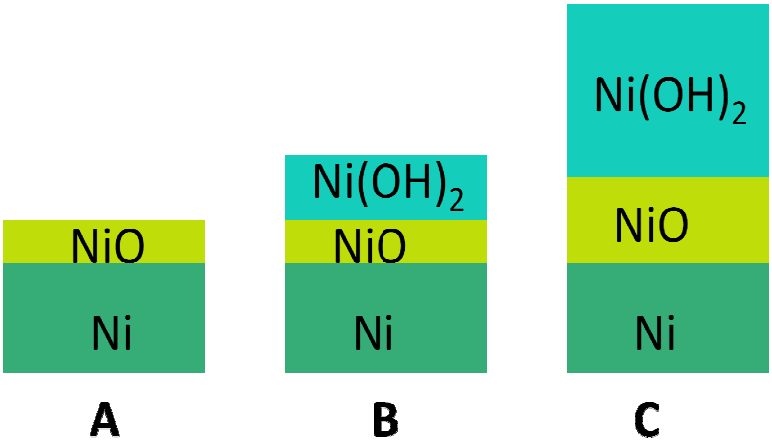

Figure 29: Passivation layers of Ni
A: Nickel surface placed in air; bulk nickel with a thin layer of nonstochiometric oxides
B: Nickel surface placed in aqueous solution
C: aged Nickel electrode (after [185]**)**

Oxide formation by exposure of nickel to oxygen and water at room temperature is time dependent. First, dissociative chemisorption of oxygen on Ni occurs. Upon further exposure the oxide film thickens over time until a final oxide layer between 2 and 4 atomic layers thick is formed [185].

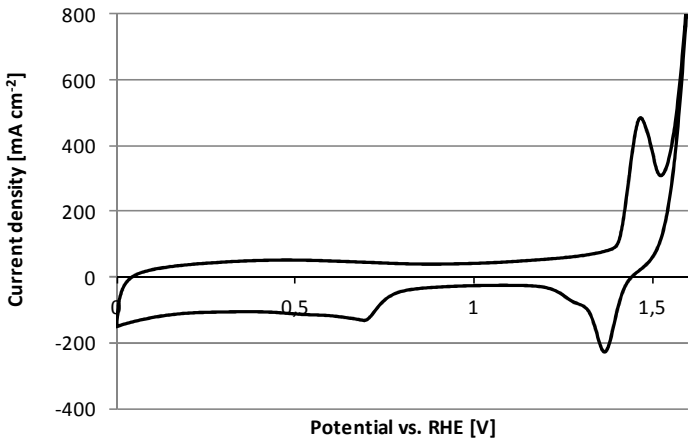

Figure 30: CV of a Ni/C electrode in 0,1 M KOH with a scan rate 10 mV s^{-1}

If a nickel electrode is placed in alkaline aqueous solution for the first time, the first sweep exhibits an additional peak on the voltammogram. The peak at ~ 0,1 V during the first cycle corresponds to the reaction

$$Ni + 2OH^- \leftrightarrow Ni(OH)_2 + 2e^-$$

and is only visible in the first cycles [186]. Oxidation of the small amount of adsorbed hydrogen also take place in this potential range [183]. This oxidation peak is followed by a oxidation plateau which corresponds to the conversion of α-$Ni(OH)_2$ to β- $Ni(OH)_2$ [186]. Three layers of β-$Ni(OH)_2$ are estimated to be built on the electrode surface [183]. At higher potentials around 1,4 V (shown in Figure 30) , NiOOH is built according to the reactions

$Ni(OH)_2 + OH^- \leftrightarrow NiO(OH) + H_2O + e^-$ and

$Ni(OH)_2 + 2OH^- \leftrightarrow NiO_2 + 2H_2O + 2e^-$.

The corresponding reduction, depending on the reaction conditions, is split into 2 peaks due to the existence of two crystallographic forms of the oxohydride which are reduced at different potentials [186]. The oxidation of $Ni(OH)_2$ to NiOOH is a first order reaction, which implies that the oxidation rate is pH dependent. For thick layers of nickel hydroxide, the diffusion of electroactive species is the rate determining step [187].

Additionally, the electrochemical behavior of a Ni electrode in CVs is to a certain extent dependent on the applied scan rate. Up to scan rates of 50 mV s^{-1}, the peak current is proportional to the scan rate as is expected for surface-adsorbed substances [188]. At scan rates higher than 50 mV s^{-1}, a deviation from this linearity can be observed which indicates a diffusion-controlled process [188]. At scan rates between 100 and 1000 mV s^{-1}, the anodic and the cathodic peak currents are proportional to the square root of the scan rate [189].

4.2.4. Electrooxidation of organic compounds

Nickel electrodes catalyze several electrochemical reactions such as the

- hydrogen oxidation [190–192]
- water electrolysis [193,194]
- oxidation of amines [171,187]
- oxidation of alcohols [171,187,195–198]
- axidation of aldehydes
- CO and CO_2 reduction [199]
- oxidation of sugar [198]

reactions.

Nickel can be used as the anode catalyst in alkaline fuel cells (AFC) using hydrogen as fuel. Hydrogen dissociates and adsorb on the surface [190]. The performance of an AFC with Ni-electrodes decreases with time. This is due to the formation of a passive layer containing of NiO which increases during fuel cell operation [192]. Nickel oxide does not catalyze the hydrogen oxidation reaction, and therefore the overvoltage increases. The nickel catalyst undergoes further changes during use which enhance degradation. The nickel particles disintegrate and become smaller. This phenomenon is known as hydrogen-induced embrittlement [190]. This embrittlement is due to hydrogen loading and unloading and causes increased electrical resistance in the catalyst particles [190].

Most oxidisable organic compounds such as aliphatic alcohols, amines, axalic acid, ethylene glycol, glycerol, and glucose are oxidized at the same potential but result in different oxidation currents. This potential is exactly the potential where the surface oxidation starts [171]. The kinetic control of these reactions is confirmed by the independence between the oxidation currents and the rotation speed when a rotating disk electrode is used. Only a few substances such as p-aminophenol are oxidized via a diffusion-controlled process [171].

Oxidized β-$Ni(OH)_2$ is a better catalyst for water electrolysis than oxidized α-$Ni(OH)_2$, due to the later onset of oxygen formation on α electrodes [172]. This effect can be observed for the majority of electrocatalytic applications. Oxidation of β-$Ni(OH)_2$ yields β-NiOOH as the main product, which exhibits better electroactive properties than the γ-form which is the main product of the oxidation of α-$Ni(OH)_2$. Although the oxidation state of γ-NiOOH is higher and more electrons could potentially be exchanged, the formation of γ-NiOOH leads to cracking and disintegration of the metal film, with higher internal resistance as a result [200].

CO can adsorb to the Nickel surface at potentials above 0 V. CO adsorbs to the surface via reaction with hydrogen, and hinders hydrogen sorption and hydroxide formation [201]. Adsorbed CO on a bare Ni electrode causes a shift in the onset potential of 300 mV in the positive direction for the oxidation from Ni metal to $Ni(OH)_2$. The initial stage of Ni oxidation is inhibited by adsorbed CO. In acidic media, CO adsorbed on Ni desorbs when $Ni(OH)_2$ is formed. In alkaline media, CO undergoes electrooxidation when the underlying metal is oxidized [202].

As observed for the oxidation of many small organic compounds, aldehyde oxidation coincides with the potential region at which NiOOH is formed. This Ni(III) oxide acts as an oxidizing agent and is involved in an acyclic oxidation mechanism similar to that proposed for Hg [203]. Aldehydes without α-keto or hydroxyl groups are oxidized to the corresponding carboxylate and Cannizarro and aldol byproducts, whereas oxidation of aldehydes containing a α-keto or hydroxyl group leads to a broad spectra of oxidation products [203].

Primary and secondary amines are oxidized to nitriles on nickel with high efficiency [171].

Glycolic and glyoxylic acid react to produce formate and a small amount of oxalate in KOH on nickel. Formate production can also be observed for ethylene glycol. Differing from Pt and Au reactions, the resulting formate shows no electroactivity on nickel [204].

The speed of the oxidation reaction is strongly dependent on the size of the substrate. The rate constants decrease for long chain substrates and sterically hindered substrates such as branches at the α-carbon [187].

The peak current densities for oxidation of organic compounds are below the values that would be expected for a diffusion-controlled reaction. Kinetic control of the electrode reaction was confirmed by experiments with a rotating disc electrode. The oxidation current is independent of the rotation speed [171].

The oxidation of small organic compounds is very sensitive to pH, the concentration of the hydroxide ion and the concentration of the substrate. At high concentrations of OH^- the current is linearly dependent on the concentration of organic species. At low OH^- concentrations, the current is barely dependent on the concentration of organic species. The influence of pH depends on the potential region. During the sharp rise of the oxidation current at low potentials, the current shows a first order dependence with respect to pH, but shows no dependence under the current plateau [171].

At constant substrate concentrations, the peak current shows a linear dependence on the concentration of OH^- until a certain break point. The position of this point depends on the organic substrate and ranges from OH^- concentrations below 0,1 M for pentanol, butanol, propanol, and ethanol to concentrations above 0,6 M for propargyl alcohol. After this point the current is independent of OH^- concentration. This behavior indicates a OH- diffusion-controlled process [205]. This break is further dependent on the concentration of the alcohol and occurs at higher hydroxide concentrations with increasing alcohol concentrations. Additionally, the break point is dependent on the thickness of the hydroxide layer. The thicker the hydroxide layer, the longer the current is dependent on the concentration of OH^- [205].

The mechanism of alcohol oxidation on Ni electrodes is dependent on the position of the hydroxyl group in the molecule. Primary alcohols are converted to the corresponding carbonic acid, secondary alcohols are oxidized to ketones, and tertiary alcohols are not oxidized at all [197].

1. Oxidation of the surface hydroxide

$$Ni(OH)_2 + OH^- \xrightarrow{fast} NiO(OH) + H_2O + e^-$$

2. Adsorption of the alcohol on the electrode surface

3. Hydrogen abstraction

$$NiO(OH) + alcohol \xrightarrow{slow\ (rate\ determining)} Ni(OH)_2 + radical\ intermediate$$

4. Oxidation of the adsorbed intermediate $NiO(OH) + radical\ intermediate \rightarrow Ni(OH)_2 + product$ [187]

In this mechanism a direct electron transfer from the alcohol to the anode is avoided [171]. Experiments with deuterated alcohols showed a primary isotope effect, ensuring that electron transfer is not rate-determining [187].

During oxidation a radical intermediate is created which further reacts with ketones and carboxylic acids for secondary and primary alcohols respectively. The rate-controlling step is the breaking of the bond between a hydrogen atom and the α-carbon atom. The nickel oxohydroxide surface contains trapped hydroxyl radicals which react with this hydrogen atom to form water [171].

At low potentials, the oxidation current is dependent on the concentration of the alcohol and the concentration of the hydroxide ion, so it is pH dependent [171]. At lower concentrations of the OH^- ion the diffusion of hydroxide ions limits the reaction rate [205].

The oxidation current for organic species is dependent on the thickness of the oxide layer. Freshly polished nickel electrodes with coverage of 10 to 20 monolayers of nickel oxides have a considerably lower activity compared to cathodically deposited or chemically prepared electrodes. This effect results mainly from an increase in the surface area which is larger for high volume nickel hydroxide than for bulk nickel [205].

On nickel electrodes, the formate ion does not show any electroactive properties in alkaline media like those demonstrated for Pt electrodes, which may provide important information on the oxidation route [204].

Ethylene glycol undergoes a selective dissociative oxidation on Ni. Ethylene glycol is oxidized to a single product, formate. Polyols such as glycerol, mannitol, and erythritol are equally oxidized to formate with a slight negative shift of the onset potential. The overvoltage decreases with the length of the carbon chain. The nickel electrode in alkaline solution affects cleavage of every C-C bond in the polyol chain. Cleavage of the C-C bond only occurs at vicinal diols. 1,2-propanediol is oxidized to equal amounts of acetate and formate, whereas 1,3-propanediol is oxidized to a broad spectrum of mainly C3 compounds [204].

For methanol, the oxidation reaction proceeds in two stages. The polarization curves for methanol in alkaline solution exhibit a sharp rising current, followed by a section with a reduced slope. In contrast to most other alcohols, the polarization curves for methanol and 2-butanol show an additional rapid rise in the oxidation current after the region with diminished slope. The selectivity for oxidation product is strongly dependent on the potential region of the oxidation. If methanol is oxidized near the onset potential, the main product is formate. At higher potentials the formate is further oxidized to carbonate. This reaction is visible in the second oxidation wave of methanol polarization curves [197].

4.2.5. Electrocatalysis of ethanol

Figure 31 shows a CV of carbon supported nickel in KOH and ethanol solution. The oxidation of ethanol on nickel in alkaline media results in 98% acetic acid [171]. The EOR is dependent on a) OH^- concentration, b) the potential and c) ethanol concentration.

The OH^- concentration that limits the dependence of the oxidation current on the oxidation current is itself dependent on the ethanol concentration. For ethanol oxidation in a 0,343 M solution, the current is linearly dependent on the OH^- concentration until 0,8 M is reached. For a 0,857 M ethanol

solution, the current increases linearly with OH^- concentration until a concentration of 0,2 M is reached [205].

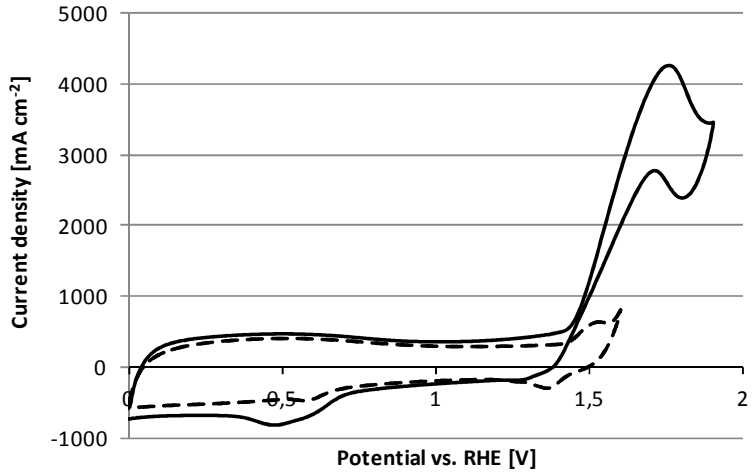

Figure 31: CV of Ni/C in 0,1 M KOH (dashed line) and 0,1 M KOH + 0,5 M EtOH (solid line) with 50 mV s^{-1} scan rate

Cyclic voltammograms in ethanol and alkaline electrolyte do not exhibit an oxidation peak on the cathodic peak at very low scan rates. If the scan rate is increased, the peak reappears. This indicates that the oxidation of nickel has faster reaction kinetics than the oxidation of ethanol [206].

The properties and activity of nickel catalysts towards the EOR can be enhanced in various ways. Besides the incorporation of additional elements and co-deposition of conducting polymers, the catalysts can be tuned by modification and enlargement of the active surface area via advanced synthesis techniques and support materials, e.g. carbon nanotubes [207]. Synthesis of nanostructured nickel electrode surfaces lowers the onset and peak potentials for the EOR due to an increased number of active sites on the electrode surface [208–210]. Furthermore, the electrocatalytic properties can be improved by employing support materials with good conductivity and high surface area such as carbon nano fibers [256] and zeolites [211,212].

Nickel-nitrogen complexes

Transition metals such as Ni, Fe, and Co form macrocyclic complexes with N_4-, N_2O_2-, S_2-, O_4-, and S_4-compounds, and are considered promising alternative to Pt in fuel cells. Mesomeric and inductive effects on the ligands cause catalytic activity, which is mainly used for oxygen reduction. The poor stability, especially in acidic media, can be ameliorated by heat treatment [102].

Introducing of conducting polymers or nitrogen complexes into a nickel electrode improves performance in various ways. The electrode benefits from the good conductivity, mechanical properties, and adhesion to electrode substrates. The properties of nickel oxide are enhanced concerning the oxidation of alcohols due to fine dispersion of the metal particles which results in a dramatic increase of active surface area. Contact with a semiconductive polymer can change the Fermi level toward the oxidation of ethanol and enhance the electroactivity [189]. Immobilized electron-conducting polymers with a reversible redox center serve as fast electron-transfer mediators between the electrode and the substrate [213]. Nickel complexes with polypyrrol [189],

diemethylglyoxime [214], porphyrines [213], or other tetraazomacrocyclic complexes such as cyclam [215] have been successfully applied to the EOR. Complexes with polyanilin [216] or o-aminophenol [217] showed activity for the oxidation of similar alcohols.

Polypyrrole [187-189]

A polypyrrole-NiO film can be produced by electropolymerization. Polypyrrol (Fig. 32) acts as a p-type semiconductor and enhances charge transfer in the electrode [189].

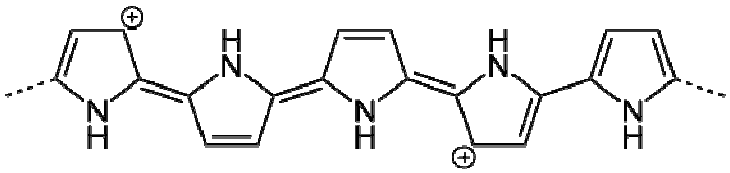

Figure 32: Polypyrrole

This composite material produces a fine dispersion of Ni particles, and as a consequence an increase of active surface area. A NiPPy on graphite electrode has as onset potential for the EOR that is ca. 150 mV lower than a conventional Ni/graphite electrode. This elctrocatalytic enhancement is attributed to the increased concentration of the active species NiOOH on the electrode surface [189].

DMG

Dimethylglyoxime (DMG) is a commonly used ligand for Ni complexes due to its sensitive formation of stable complexes (Figure 33). Nickel complexed with dimethylglyoxime ($Ni(II)(DMG)_2$) catalyzes the oxidation of ethanol to acetate via a 4-electron process. $Ni(II)(DMG)_2$ is oxidized to $[(DMG)_2(H_2O)Ni(III)ONi(III)(OH(DMG)_2]^-$ [214].

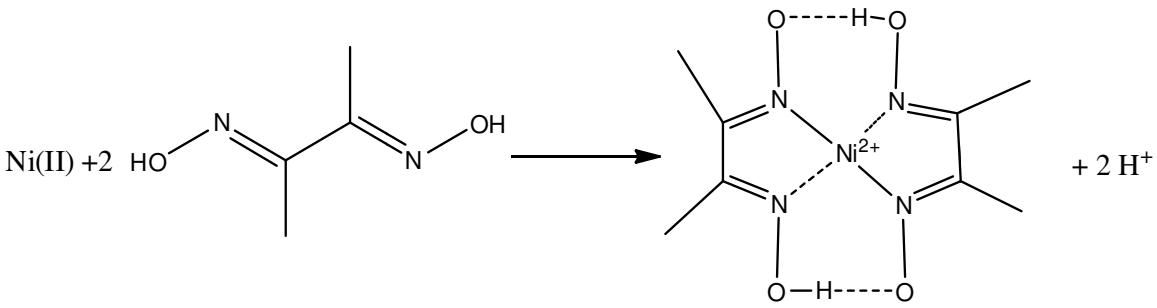

Figure 33: Complexation of dimethylglyoxime

Porphyrin

In this macrocyclic complex Ni is bonded to four nitrogen atoms in a square planar arrangement (Figure 34). The Ni redox center exhibits high catalytic activity towards the EOR. These electrochemically polymerizable complexes can be substituted with various ligands [213].

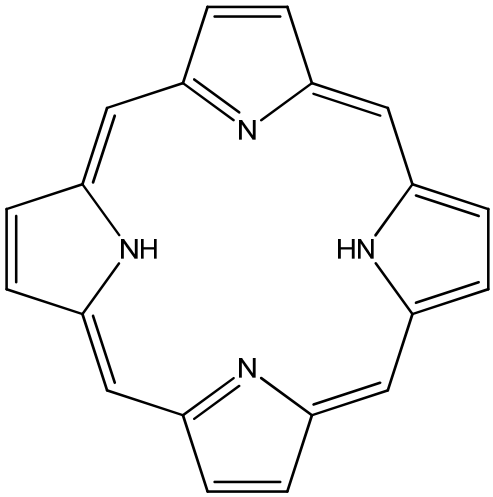

Figure 34: Porphyrin

Cyclam and derivatives

A high pH is a prerequisite for Ni-cyclam (cyclam is 1,4,8,11-tetraazacyclotetradecane, shown in Figure 35) film formation. Cations and anions from the supporting electrolyte have no influence on the electrode, except for NH_4^+ cations which block the redox center [215].

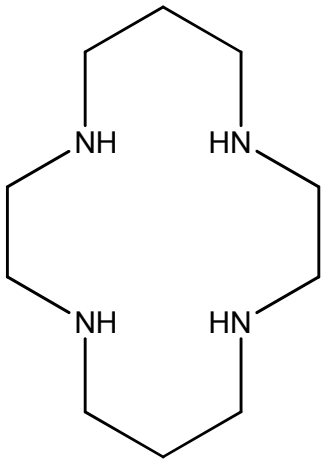

Figure 35: Cyclam

Nickel alloys and admetals

The addition of foreign atoms to nickel electrodes can enhance their elctrocatalytic activity towards the EOR. In most cases this is due to improved long-term stability. The admixture of supplemental atoms suppresses the formation of γ-NiOOH. The formation of the γ-phase leads to volume expansion and subsequent disintegration of the surface and a higher internal resistance. β-NiOOH is the favored phase for elctrocatalytic applications in alkaline media [218]. Besides the following possibilities which have already been applied to EOR, nickel-titanium [219,220], nickel-zinc [221],

nickel-copper [200,222], and nickel-aluminium alloys [223] show activity for methanol oxidation or similar activity, and may also exhibit activity towards EOR.

Cr:

Incorporation of Cr_2O_3 nanoparticles into an electrodeposited Ni electrode leads to modification of the surface morphology of the electrode. Cr_2O_3 particles reduce the size of nickel grains due to their increased deposition at nickel grain boundaries [206].

Strongly dependent on the composition of the electrode, the addition of Cr_2O_3 nanoparticles promotes the EOR. Besides a slight enhancement of the charge transfer process of $Ni(OH)_2$/NiOOH, the crucial factor for this promoting effect is the increased surface area and increased number of effective sites [206]. The cyclic voltammetric behavior of Ni-Cr electrodes is similar to that of pure electrodes. The electrochemical charge of the alloy is higher [224].

The addition of Cr_2O_2 nanoparticles to a nickel electrode results in improved performance towards the EOR in terms of stability. The presence of Cr_2O_3 has a positive influence on the undesired formation of γ-NiOOH and stabilizes β-NiOOH [206].

Ni-P

Phosphor admixed to the nickel electrode results in a smooth structure and a less porous structure of the Ni-P alloy. Improvement of the elctrocatalytic performance is attributed to its suppression of the γ-NiOOH phase [218,225]. Ni-P alloys tend to exclusively form hydroxides and oxohydroxides in β form and build a better defined surface structure than electrodes without phosphor [226].

Ni-B

The addition of boron to nickel electrodes enhances activity towards the EOR as well as stability. This positive effect of boron in a Ni-B alloy is based on both structural and electronic effects.

The structure of a Ni-B alloy strongly depends on the boron content. Deposited alloys with boron contents below 8 atomic % are nanocrystalline, alloys with 10-15 at% exhibit both nanocrystalline and amorphous regions and alloys with a boron content higher than 20 at% are amorphous. A mixed heterogeneous crystalline-amorphous structure enhances the EOR on Ni electrodes due to an increased number of active sites.

The addition of boron decreases the coordination number of nickel atoms on the electrode surface. This enhances the degree of unsaturation of the Ni atoms and promotes the chemisorption of ethanol. In amorphous alloys, an electronic interaction occurs between Ni and B. Electrons are transferred from B to Ni, causing electron enrichment of Ni and electron deficiency in the B. This has a positive effect on the EOR efficiency due its decrease of catalyst poisoning by intermediate products.

The stability of Ni-B electrodes increases with the boron content and therefore with the amorphous fraction [227].

Ni-Fe-Co alloy catalyst

Ni-Co-Fe alloys in a hydrazone-based polymer matrix are reported to accomplish complete oxidation of ethanol to CO_2 with high efficiency. Due to the dominance of the complete oxidation pathway, no acetate occurs, and acetaldehyde is further oxidized to carbonate. The suggested reason for the good performance of the catalyst is the lack of CO. Ni provides the active site for the dehydrogenation of ethanol while Co and Fe serve with adsorbed OH [228].

4.2.6. Comparison of potentials and peak currents of the EOR on nickel in the literature

Table 4 compares all achieved and published peak current densities during ethanol oxidation in alkaline media on nickel electrodes. Figures 36 to 39 show peak and onset potentials of gold and nickel catalysts.

Table 4: Comparison of achieved current densities in the literature. In the case of several published values with different reaction conditions in one paper, the highest was chosen
***value determined from a graph because not given in the text**

Onset P [V]	Peak P [V]	Peak j [mA cm^{-2}]	catalyst	Electrolyte	Scan rate [mV s^{-1}]	
0,38* Ag/AgCl	0,73* Ag/AgCl	0,53*	Ni/CNT	0,1 m KOH 0,2 M EtOH	20	[207]
		0,34	Ni disc	0,87 M KOH 0,1 M EtOH		[171]
-0,3* Hg/HgO	0,2* Hg/HgO	4,75*	Nanoporous Ni	1 M KOH 1 M EtOH	50	[210]
-0,45* Hg/HgO	-0,2* Hg/HgO	17	Ni hollow spheres	1 M KOH 1 M EtOH	5	[208]
0,45* Ag/AgCl	0,7* Ag/AgCl	1,4* mA	Ni POAP modified graphite	0,1 M NaOH 0,02 M EtOH	10	[217]
0,5* Ag/AgCl	0,6* Ag/AgCl	20,88	Ni disc	0,07 M KOH 0,686 M EtOH	10	[205]
1,38*	1,49*	1,25*	Ni sheet	1 M EtOH 1 M NaOH	20	[229]
0,4* SCE	0,44 SCE	0,01*	Ni microrods	0,01 M EtOH 0,1 M NaOH	50	[196]
0,25* Ag/AgCl	0,4* Ag/AgCl	4,5 mA	Ni(II)DMG_2 complex	0,1 M EtOH 1 M NaOH	5	[214]
0,45* Hg/HgO	0,775 Hg/HgO	327	Ni-Cr_2O_3/C	1 M NaOH 2 M EtOH	50	[206]
0,45* Hg/HgO	0,874 Hg/HgO	282	Ni-B/C	1 M NaOH 2 M EtOH	50	[227]
0,36* Ag/AgCl	0,48* Ag/AgCl	25*	Ni-P/SnO_2/Ti	1 M KOH 1 M EtOH	150	[225]
0,33* SCE	0,55* SCE	8* mA	Ni/Polypyrrol	1 M NaOH 1 M EtOH	10	[189]
	0,59 SCE	0,17* mA	Ni/TMHPP	0,1 M NaOH 0,5 M EtOH	100	[213]
0,4 Ag/AgCl	0,61 Ag/AgCl	110 mA mg^{-1}	Ni/C	0,1 M KOH 0,1 M EtOH	20	[195]

4.3. Conclusion

A broad variety of alternatives to rare and therefore expensive platinum group metals has been presented in this review. The literature in the recent years has concentrated on nickel and gold as potential non-PGM catalysts for the EOR. Gold as a catalyst, and in particular as an electrocatalyst, has been well explored, but the exact reaction mechanism for the EOR is still based on assumptions and contradictory proposals have been published.

The literature on nickel as an electrocatalyst is not so well reviewed, although results on alcohol oxidation have been published for 50 years. These promising results warrant a closer look at the complex electrochemistry of nickel. A fundamental understanding of the state of the surface and phase transitions is a prerequisite in order to design an effective catalyst for the EOR. Promising results with Ni-based alloys and polymer composites show that there is still space for further amelioration.

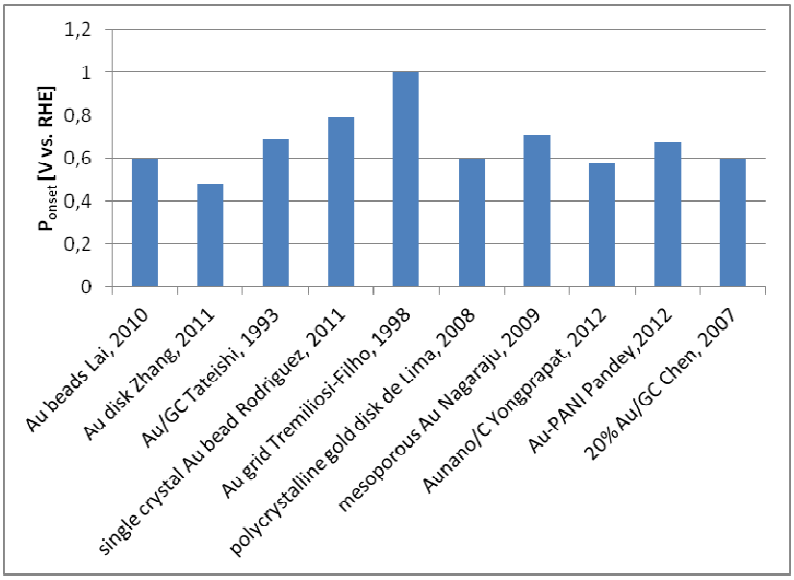

Figure 36: Comparison of onset potentials during EOR with gold catalysts. All potentials refer to an RHE at pH 13.

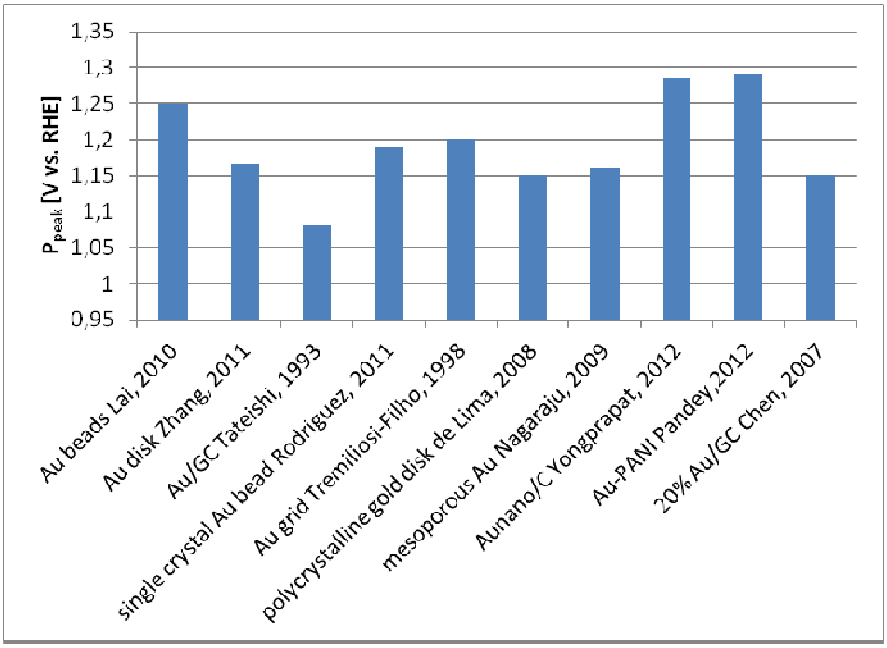

Figure 37: Comparison of peak potentials during EOR with gold catalysts. All potentials refer to an RHE at pH 13.

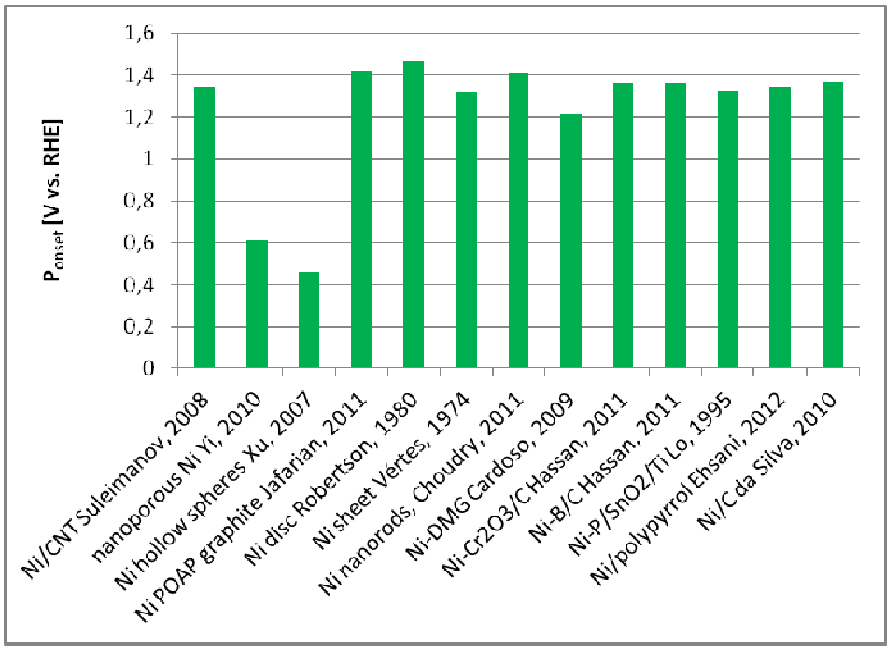

Figure 38: Comparison of onset potentials during EOR with nickel catalysts. All potentials refer to an RHE at pH 13.

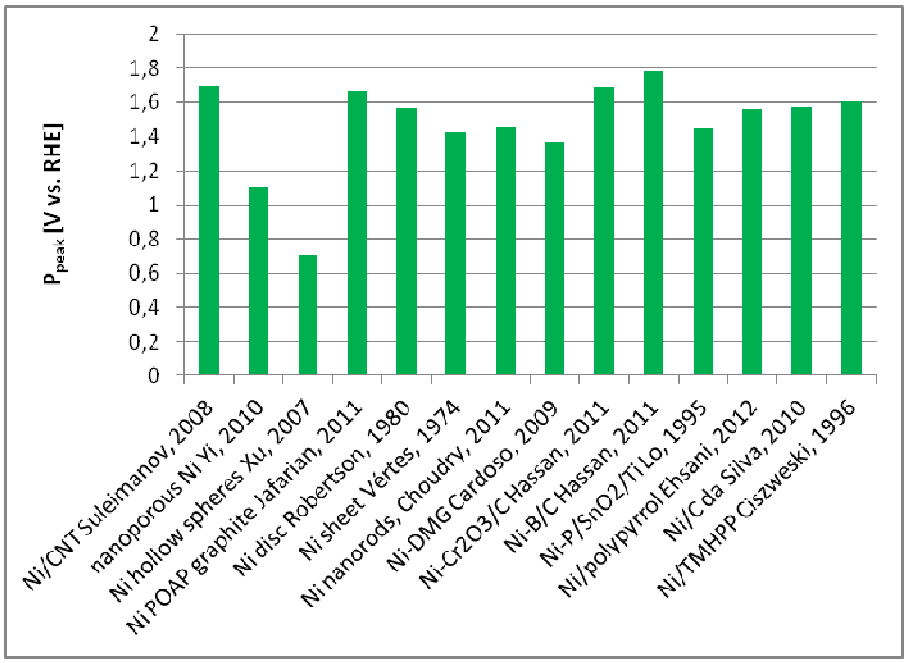

Figure 39: Comparison of peak potentials during EOR with nickel catalysts. All potentials refer to an RHE at pH 13.

5. Development of anode catalysts for alkaline direct ethanol fuel cells

5.1. Aim, methods and experimental set-up

5.1.1. Aim

The aim of the experimental work was to develop highly active anode catalysts for ADEFCs. A prerequisite for the choice of the catalyst material was the avoidance of platinum group metals (PGM). Among PGMs rank platinum, palladium, rhodium, ruthenium, osmium and iridium (Figure 40).

Fe	**Co**	**Ni**	**Cu**
Ru	**Rh**	**Pd**	**Ag**
Os	**Ir**	**Pt**	**Au**

Figure 40: Excerpt of the periodic table of elements (groups VIIIb and Ib until period 6)

A screening for activity towards the EOR was performed among transition metals and compounds in order to pick out the most active metals for further investigations. The most auspicious results were obtained with nickel and gold catalysts. The next step was to develop highly active and stable catalyst systems based on these two metals. Different synthesis methods, support materials and different pretreatment of these carbon based materials were applied in order to adjust the fabrication to the features of the metal. The characterization of the catalysts focused on electrochemical methods.

5.1.2. Methods

All catalysts were characterized with a combination of several methods. The focus was on electrochemical characterization methods including cyclic voltammetry (CV) and chronoamperometry (CA) techniques. Product formation was monitored via gas chromatographic measurements. Information on the morphology of the electrocatalysts was obtained by SEM-EDX. Elemental analysis for information on the metal load was performed with ICP-OES.

Electrochemical characterization methods

Experimental set-up

The electrochemical experiments were performed in a glass cell with a Pt wire as counter electrode and a reversible hydrogen electrode (HydroFlex®, gaskatel). The catalyst inks were applied on a RDE tip consisting of a glassy carbon disk with 5 mm OD in a PTFE cylinder (pine industries). The RDE tip was fixed on a rotator (Princeton Applied Research).

The catalyst slurries were prepared with a certain amount of catalyst (around 15 mg, weighed with analytical balance), 400 µl Isopropanol and 50 µl Nafion solution (5 wt% in isopropanol) and sonication for 15 minutes in an ultrasonic bath. A volume of 10 µl of this ink were transferred to the RDE tip and dried for 15 minutes. In order to compensate variation of the sample weight, all current densities are normalized to one mg.

All catalysts were surveyed in a solution of 0,1 M KOH in deionised water (18 MΩ) and a solution of 0,1 M KOH and 0,5 M Ethanol in deionised water. For each measurement 50 ml electrolyte was placed in the glass cell and purged with pure nitrogen for 30 min in order to remove solved gases.

The measurements were performed with a galvanostat/potentiostat (Autolab/PGSTAT302N).

Cyclic voltammetry (CV)

Voltammetric methods provide quantitative and qualitative information on the properties of materials. During cyclic voltammetry the potential is swept with a fixed scan rate between two values and the resulting current-potential diagram is recorded. This method is mainly applied in order to gain information on electrochemical reactions. If an electroactive species is present in the electrolyte, the currents originating from chemisorptions process on the surface are superimposed by the current resulting from the corresponding reaction. If no species are available that are electrochemical converted between the chosen potentials, the resulting currents originate from chemisorptions on the electrode surface [230]. Differentiation between currents from reactions on the surface layers and electrochemical reactions of components of the electrolyte is possible by the choice of the scan rate; more precisely, the higher the scan rate, the more currents from electrode surface oxidation and reduction become visible [231].

For information on the catalyst surface CV experiments were performed in 0,1 M KOH at scan rates of 50 mV/s if not noted differently. Especially for Pt based electrocatalysts it is common practice to determine the electrochemical active surface area (EASA) derived from hydrogen adsorption peaks. Neither Ni nor Au exhibit potential regions with hydrogen adsorption. For information on the surface, the charge of the reduction peak from the surface oxide reduction reaction was determined. The oxide layer of Ni is not completely evident and the number of layers and type of oxides is strongly changing with time. Therefore no trustable constants can be found in literature to calculate the EASA of Ni in electrocatalysts. In order to provide comparability the charge of the Ni oxide reduction peak was calculated for various Ni catalysts since it can be assumed that all catalysts had a similar history. The EASA of gold was calculated by the assumption that one cm^2 holds a charge of 386 µC [133]. Again it has to be outlined that oxide formation on gold does not proceed strictly in monolayers and the determined value contains a substantial error.

CV experiments in 0,1 M KOH and 0,5 M EtOH were performed with a scan rate of 10 mV/s unless otherwise stated. As the most important properties, the onset potential and the peak potential were noted. The onset potential was defined as potential when the oxidation current was twice the capacitive currents. Peak potentials were defined as the potential when the current density from the EOR reaches its maximum.

Chronoamperometry

For information on the stability of the catalysts, the current densities were recorded over a certain time at a fixed potential in 0,1 M KOH and 0,5 M EtOH in deionised water as electrolyte. The duration of the experiments was 600 s and 1200 s respectively. As potential the peak potential was chosen from CV experiments which was 1,6 V for Ni catalysts and 1,2 for gold catalysts. The limiting current densitiy was determined by the arithmetic mean of the last 100 s of the experiments. For bimetallic catalysts, the limiting current densities were determined for all potentials between 0,4 V and 1,8 V in 0,1 V steps.

Gas chromatography

The electrolytes from CA experiments were analysed qualitatively with a gas chromatograph (SRI 8610C) equipped with a N plot column and helium as carrier gas. The reaction products were detected with FID and TCD detectors. Prior to injection of a distinct volume of the probe, the electrolyte was neutralized with HCl. In all samples acetic acid and acetaldehyde were detected.

Inductively coupled plasma optical emission spectrometry (ICP-OES)

The elemental analysis of the catalysts was performed by the Institute of Analytical Chemistry and Food Chemistry. The samples were solubilized microwave assisted at 40 bar and 210°C with aqua regia. The amount of Ni and Au was then determined with ICP-OES (Ciros Vision EOP).

Scanning electron microscopy coupled with energy dispersive X-ray spectroscopy (SEM-EDX)

SEM analysis was performed at the Institute for Electron Microscopy and Nanoanalysis (FELMI) together with Hartmuth Schröttner. The analysis was performed on a Zeiss Ultra 55 Gemini with an energy dispersive X-ray spectrometer (Genesis, EDAX Inc.). The electron energy used for the analysis was 7 keV. A sample of the loose material was poured on a graphite tape. For all catalysts first a survey image was recorded followed by detail images. The elemental composition on the surface was measured with EDX. An AsB detector was used for further compositional information and In-lens SE detector for a high contrast surface.

5.2. Support material

5.2.1. Introduction

Since electrocatalytic reactions take place on the surface of the catalyst, they are very sensitive to the heterogeneous interface. This interface is not only influenced by the catalyst surface, electrolyte ions and reaction products are also involved in this dynamic interplay of the active site of the catalyst [232]. Carbon has been used for many years as catalyst support for various processes in industry and research. Activated carbon is stable in both acidic and alkaline media and allows a fine metal dispersion and stabilizes the particles [233]. Support materials have to fulfill further requirements in order to qualify for application in low temperature fuel cells. The electronic conductivity has to be sufficient to provide electronic flow in the electrode. Catalyst layers in fuel cells must be relatively thin in order to avoid strong influences from mass transport in the electrode [234]. Therefore the support material should provide a high active metal surface, pores for improved mass transport of electrolyte and reaction products and electronic conductivity. Moreover, the support material must stabilize the metal surface and improve the conditions for the electrochemical reaction. Aside from surface area effects, the support material influences the reaction by providing adsorbed species such as hydroxide or additional oxygenated species.

Several carbon materials such as carbon black, graphite material and ordered carbon materials such as carbon nano tubes (CNT) have been used as support materials in low temperature fuel cells. Carbon black is widely applied as support due to its low cost and high availability [235]. Vulcan XC72 is an oil-furnace carbon black with non monodispersed particles.

Carbon nanofibers (CNFs) are catalytically grown by decomposition of a carbon containing gas or polymers [234,235]. The definitions and differences between carbon nano tubes and carbon nano fibers are blurred and are handled individually. CNFs do not have a hollow cavity mandatorily compared to CNTs, but the variety of possible structures (platelet, fishbone, hollow etc.) makes classification difficult [236]. CNFs possess high mechanical strength, high electrical conductivity and exhibit high chemical stability in aggressive environment.

Pretreatment of carbon materials can further increase the metal dispersion and catalytic activity. Pretreatment methods can be classified in chemical and physical activation methods. The chemical activation is also referred to as oxidative treatment and involves application of strong oxidants such as HNO_3, H_2O_2 or O_3. The oxidative treatment increases the number of oxygen surface groups and forms surface acidic sites [255].

Physical methods involve a thermal treatment under inert atmosphere or air at temperatures ranging from 400°C to 1100°C. This activation step removes impurities from the carbon surface.

An alternative way to ensure finely dispersed metal deposits is the application of perovskites. The properties of this metal oxide support material are defined by the exact phase composition and the structural defects [237]. La_2NiO_4 was prepared via a modified sol gel solution combustion synthesis.

In this thesis different support materials (carbon black, CNFs and a perovskite type) were pretreated with different methods and subsequently used as catalyst support. The influence on the metal deposition efficiency and the metal surface area were examined.

5.2.2. Experimental

Pretreatment support materials

For thermal activation, Vulcan XC 72 from Cabot was heated at 500°C under a nitrogen stream for 4h and cooled down to room temperature in nitrogen atmosphere. For oxidative pretreatment, Vulcan XC72 was heated under reflux in ≥ 69 wt% HNO_3 for 2 h. The product was then filtered and washed with H_2O_{deion} until the filtrate was pH neutral and dried in air at 90°C. Catalysts with not pretreated Vulcan XC72 as support material were noted as C, with thermal pretreatment as C_{therm} and oxidative treatment as C_{ox}. Tubular CNFs (HRF150FF-LHT) with an average outer diameter of 150 nm were oxidised in nitric acid ≥ 69 wt% under reflux for 8 h. Afterwards the material was washed with deionised water until the filtrate was neutral. Catalysts with oxidative pretreated CNFs were noted with CNF_{ox}, with CNFs used as received are noted with the suffix CNF.

Catalyst preparation

Nickel(II)nitrate hexahydrate ($Ni(NO_3)_2*6H_2O$) and gold(III) chloride trihydrate ($AuCl_3*3H_2O$) were diluted with H_2O_{deion} to 0,1 M solutions. The pretreated or non-pretreated carbon support materials were dispersed in 0,2 M citric acid in the ultrasonic bath and an aqueous solution of the metal ion was added to reach nominally 30 wt% metal. This solution was heated until a temperature of 60°C was reached, then an excess of $NaBH_4$ was added and stirred for 6 h. Finally, the catalysts were washed with deionised water and dried at 80°C.

For the perovskite oxide La_2NiO_4, a citric acid sol-gel solution combustion was conducted [238]. To a 0,25 M aqueous solution of the $La(NO_3)_3*6H_2O$ and $Ni(NO_3)_2*6H_2O$ in the appropriate metal relation citric acid, ethylene glycol and a few drops of HNO_3 were added and slowly heated after a gel was formed. The heating to 100°C initiates the nitrate decomposition which reacts further with the fuel (ethylene glycol) and lead to high temperature combustion. The solid product was calcined at 600°C for 6 h.

The catalysts were dispersed in a solution of isopropanol and Nafion in the ultrasonic bath for 30 min. A distinct volume of this ink was transferred to a glassy carbon disk electrode and dried.

Characterization

The catalysts were examined electrochemically and physically. Electrochemical characterization was performed in 0,1 M KOH solutions with cyclic voltammography in order to calculate the surface area or in the case of Ni the surface charge. The catalytic activity towards the EOR was examined in 0,1 M KOH + 0,5 M EtOH solutions with CV and chronoamperometric measurements. The morphology of the catalysts was studied with SEM and the metal loadings were verified with ICP-OES.

5.2.3. Results

Metal loadings

Analysis of the ICP-OES results shows a great variance of the effectiveness of the metal deposition. Generally, the deposition efficiency of Ni on the carbon support material is rather low. From the aimed 30 wt% (300 mg g^{-1}) only 4% was deposited (Figure 41). Ni adhesion on CNF support material is significantly lower than on active carbon. Even though oxidative treatment multiplied the amount of deposited metal, it is still considerably lower than on active carbon (Table 5).

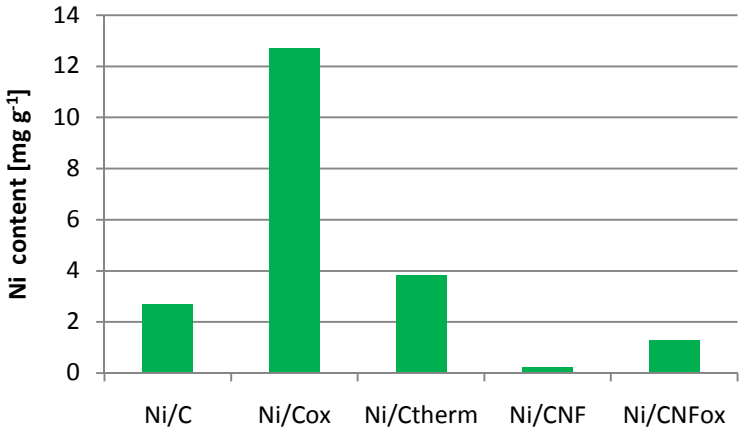

Figure 41: Ni loadings on carbon support

Chemical deposition of gold on active carbon yielded in 70 to 85 % of the aimed metal loadings (Figure 42). The highest gold loading was achieved with oxidative treated Vulcan Carbon XC72.

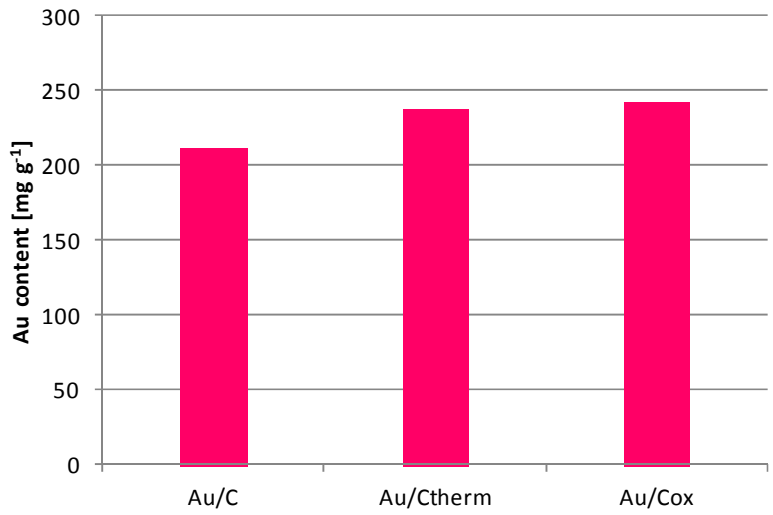

Figure 42: Au loadings on carbon support

Table 5: metal loading on carbon support

catalyst	mg g^{-1}
Ni/C	2,69 ± 0,08
Ni/C_{ox}	12,70 ± 0,08
Ni/C_{therm}	3,8 ± 0,1
Ni/CNF	0,23 ± 0,01
Ni/CNF_{ox}	1,267 ± 0,009
Au/C	211 ± 39
Au/C_{therm}	237 ± 4
Au/C_{ox}	242 ± 8

Morphology

Ni/C

SEM-EDX measurements disclose that Ni was hardly deposited on the carbon support but rather diffused into the carbon particle. Comparably to the indicated EDX diagram of Ni/C_{ox} (Figure 43), all examined Ni catalysts showed a very low amount of Ni on the surface.

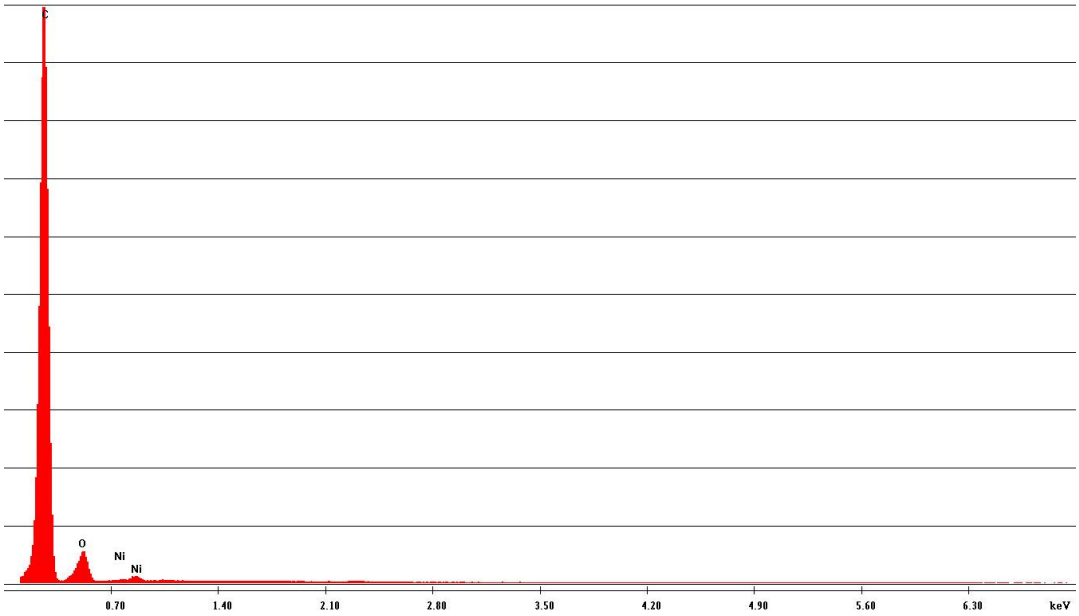

Figure 43: EDX diagram of Ni/C_{ox}

Examination of the catalysts revealed, that the fiber structure of the CNF catalyst was destroyed during the oxidative pretreatment step (Figure 44c), which indicates that the chosen pretreatment conditions were too harsh. The metal deposition step did not harm the fibrous morphology, since the carbon nano fibers of Ni/CNF are well visible in Figure 44d. The SEM measurements do not reveal any changes on the support morphology between thermal and oxidative treatment. As far as visible, the surface on both materials is fine grained, but according to ICP-OES results the Ni loading is higher on the acid pretreated carbon (Figure 41).

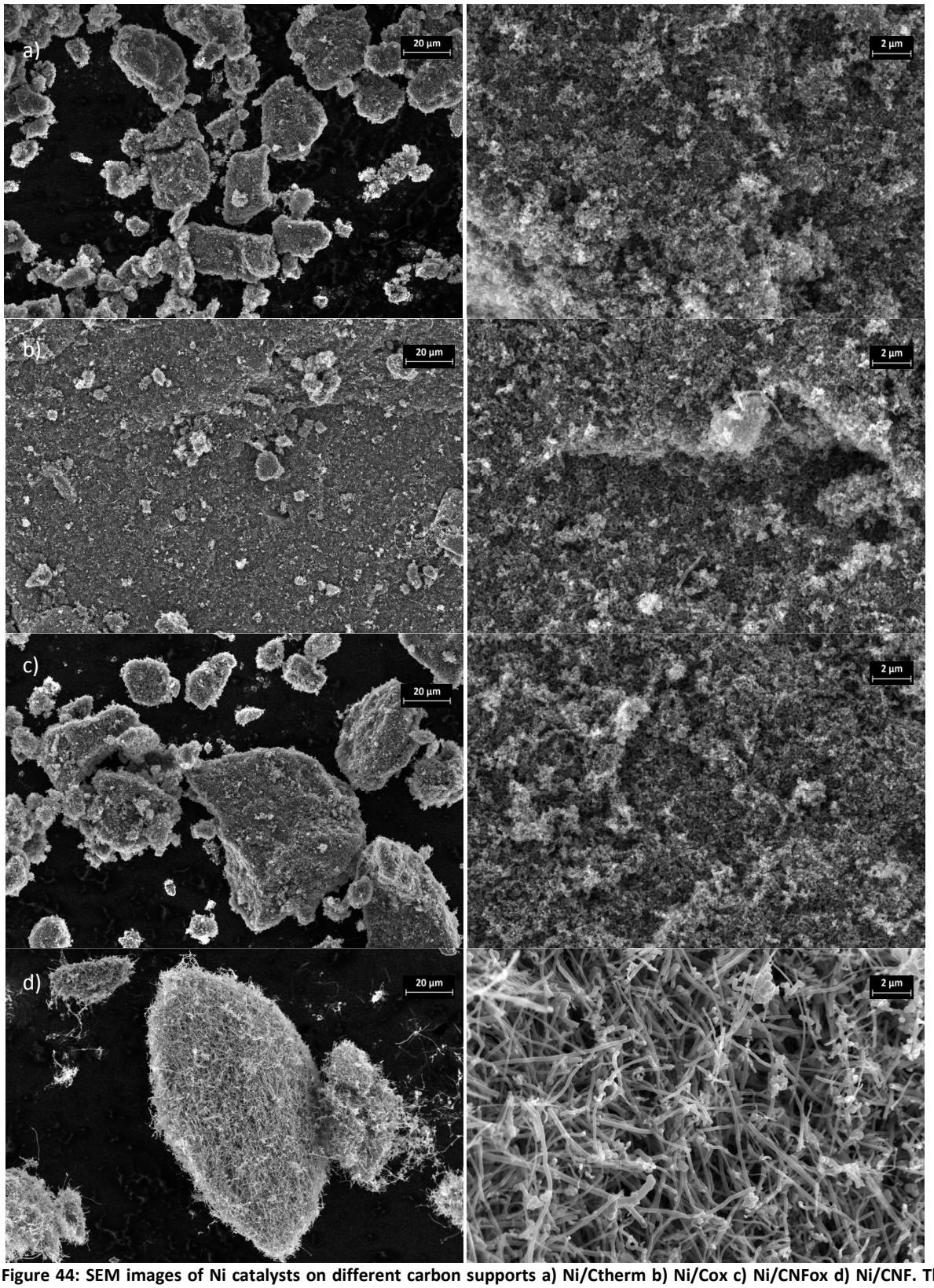

Figure 44: SEM images of Ni catalysts on different carbon supports a) Ni/Ctherm b) Ni/Cox c) Ni/CNFox d) Ni/CNF. The left image of each row represents an overview of the catalyst probe and on the lright side a detail study of the catalyst surface is given.

La_2NiO_4

Examination of the perovskite catalyst with SEM-EDX revealed rather coarse particles with high oxide content (Figure 45). Possible sources for the carbon fraction in the particle are residues of citric acid ethylene glycol from catalyst synthesis and contamination during sample preparation with the carbon tape from the specimen holder. Besides the high oxide content EDX analysis localizes the deposition of lanthan and nickel.

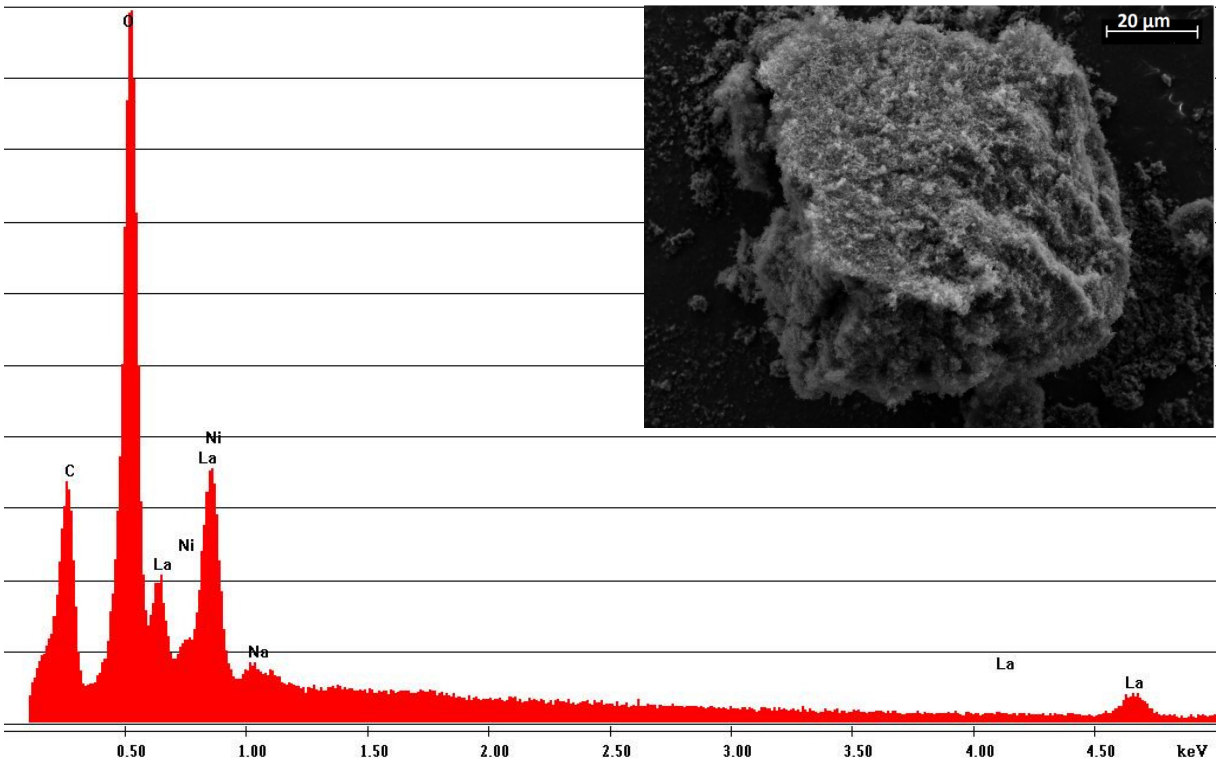

Figure 45: EDX diagram of La_2NiO_4 and a SEM image from a La_2NiO_4 particle (insert)

Au/C

Figure 46 shows SEM images from Au/C with different pretreated active carbon support. The left picture of each row was recorded with an InLens detector in order to display the fine structure of the sample. The image on the right side shows the identical detail recorded with an AsB detector in order to give information on the involved elements. The oxidative treatment of the carbon support before gold deposition (Figure 46c) caused a significantly smaller particle size and finer distribution on the surface compared to not pretreated material (Figure 46a).

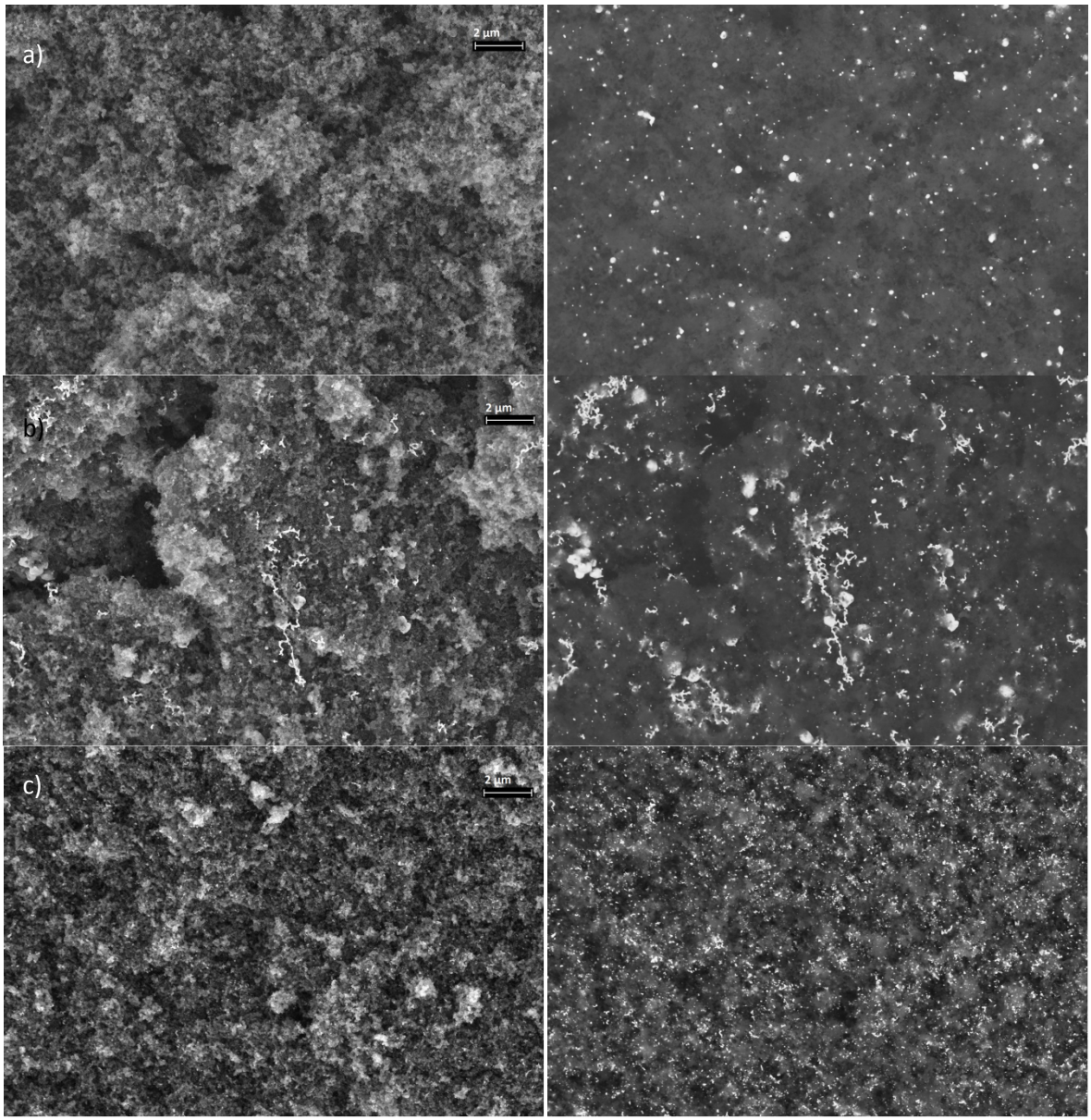

Figure 46: SEM images of gold on different support materials a) Au/C b) Au/Ctherm c) Au/Cox. The images on the left side were recorded with an InLens detector in order to display the fine structure of the sample, the image on the right side shows the identical detail recorded with an AsB detector.

Whereas gold on non pretreated and oxidative pretreated carbon deposited in dispersed particles with different size, the Au/C_{therm} catalyst exhibits various forms of deposits (Figure 46b). On the thermal pretreated carbon gold is formed to a great extent in coral like filaments. Additionally, two further forms can be observed. Larger gold accumulations in tablet form with hexagonal alignment are surrounded by finely dispersed gold particles comparably to Au/C_{ox} (Figure 47).

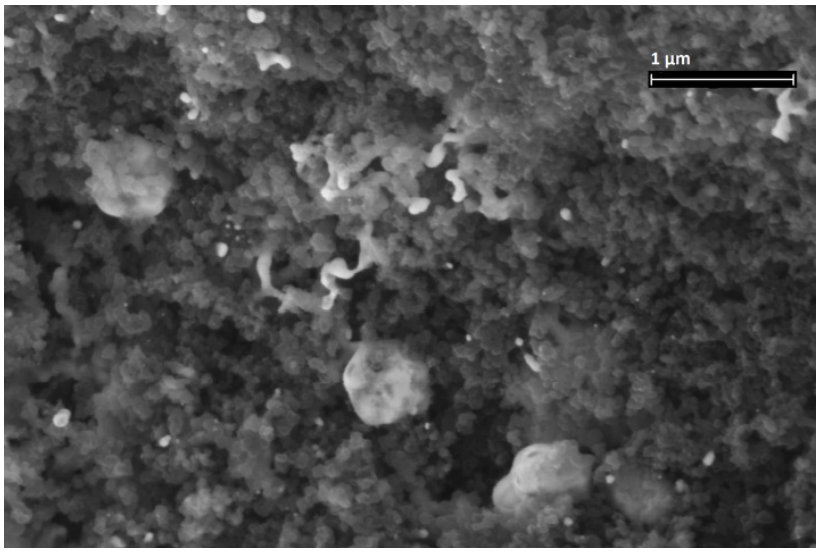

Figure 47: Detail SEM of Au/C_{therm}

Electrochemical characterization

Figure 48 displays CVs of the blank carbon supports in 0,1 M KOH at 50 mV/s. Although the capacitive currents on the thermal pretreated active carbon are notably higher, both support materials exhibit similar features from oxidation processes. Between 0 and 0,5 V oxygen adsorption and desorption processes constitute broad peaks on the forward and the back scan as well. At 1,5 V currents from oxygen evolution become visible.

The higher capacitive currents on C_{therm} suggest that the surface area of is significantly higher.

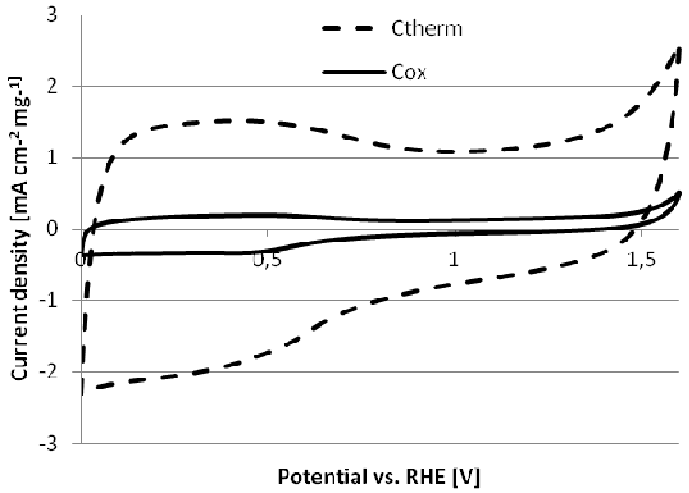

Figure 48: CV of C_{therm} (dashed line) and C_{ox} in 0,1 M KOH (continuous line) with scan rate 50 mV/s

Electrochemical active surface area (EASA)

Nickel

Since Ni does not adsorb hydrogen, the oxidation peaks were considered for calculation of the electric charge of the electrode. At the anodic scan the peaks for oxide formation and oxygen evolution overlap. On the reverse scan, the reduction peak is better separated therefore better suitable for surface normalizations. It has to be pointed out that this method is not appropriate for exact determinations of the EASA. Ni oxidation does not occur in monolayers and the composition of the oxide layer is strongly related to the history of the electrode, especially applied switch potentials and electrolytes. Therefore published constants for the charge per area for Ni seem not trustworthy. Nevertheless, for the sake of comparison the electric charge is calculated for each Ni catalyst. All catalysts were processed the same way and in the same electrolyte, therefore these influences can be excluded.

Table 6: Details for the calculation of the electric charge on Ni electrodes

catalyst	U interval (I_C) [V]	U interval (I_{red}) [V]	Q [mC]
Ni/C	1,15-1,25	1,25-1,5	0,0123048
Ni/CNF$_{ox}$	0,85-0,95	0,95-1,26	0,01035833
Ni/CNF		no reduction peak	
Ni/C$_{ox}$	1-1,1	1,1-1,4	0,05361421
Ni/C$_{therm}$	1,1-1,15	1,18-1,4	0,03850265
La$_2$NiO$_4$		no reduction peak	

The potential interval for calculation of the capacitive current (I_C) was adapted to the CV but was generally between 0,9 and 1,2 V. The range for the calculation of the reduction current (I_{red}) was between 1,2 and 1,4 V (Table 6). Comparison of all CVs of Ni on various support materials in 0,1 M KOH at scan rate 50 mV/s (Figure 49) reveals great differences of the surface currents. The perovskite type catalyst and Ni/CNF do not exhibit any reduction peaks and are therefore excluded from further analysis.

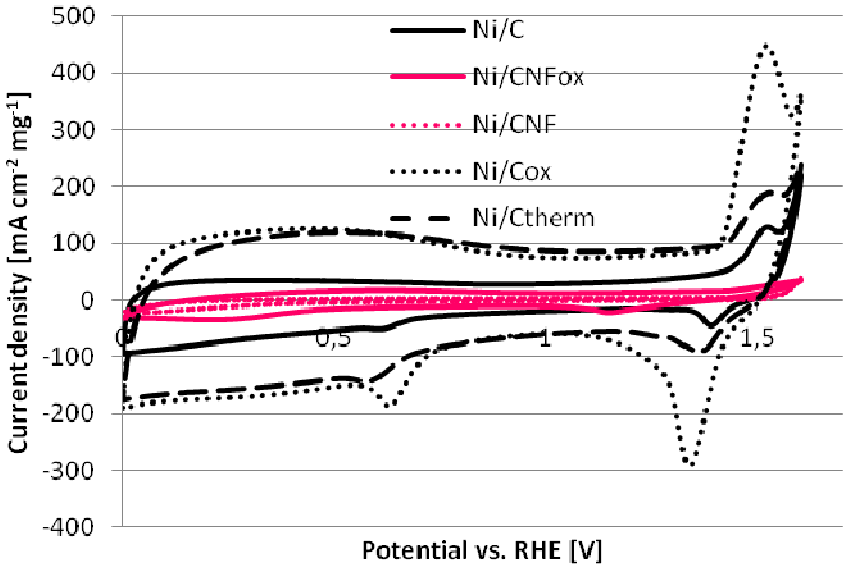

Figure 49: CV of Ni on various support materials in 0,1 M KOH at scan rate 50 mV/s

Generally, currents on CNF catalysts (pink lines in Figure 49) are significantly lower than on active carbon, both capacitive currents and peaks from reactions with oxygen. Similar conclusions can be drawn from the comparison of pretreated and non pretreated carbon support. The peaks between 0 and 0,5 V which were identified as oxidation processes from the carbon support in Figure 48 are about the same size, indicating that the surface of the thermal and oxidative pretreated carbons have the same surface area. Nevertheless, the electric charge from the Ni surface oxidation is much higher.

This order remains when the measured values are normalized to the real amount of Ni in the catalyst determined with ICP-OES. Figure 50 displays the differences of Q_1 in Coulomb per g Ni and Q_2 in mC per g catalyst, which means metal and support.

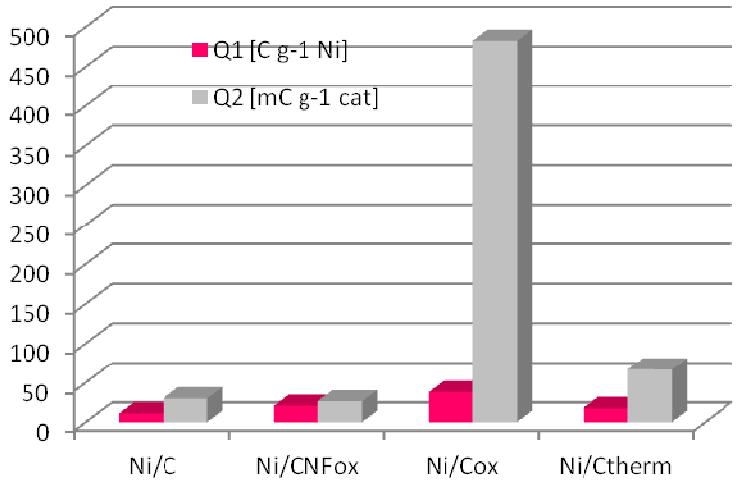

Figure 50: Comparison of the electric charge on Ni electrodes

Gold

Gold does not exhibit a hydrogen adsorption region and the oxide formation coincides with the oxygen evolution (Figure 51). Therefore calculations for the EASA were based on the reduction peak too. It was determined that the surface area of polycrystalline gold holds a charge of 386 µC/cm^2 [136]. On carbon supported gold catalysts the identification of the capacitive current is difficult because the gold surface oxide reduction is followed by the oxide reduction from the carbon support. As capacitive current the minimum reduction current between these two areas was determined (Figure 51, Table 7).

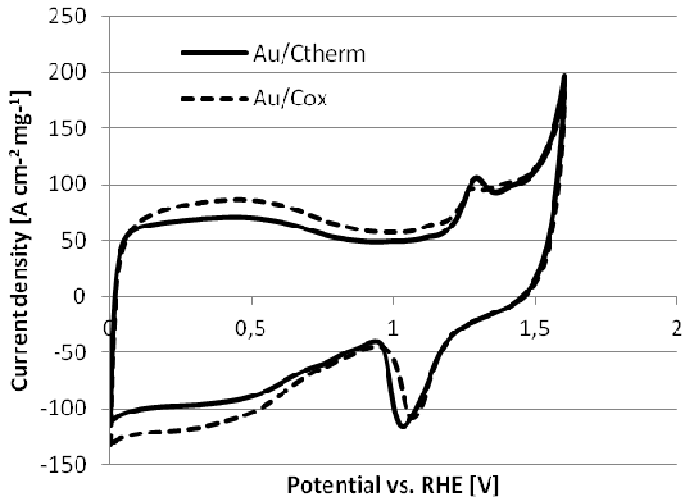

Figure 51: CV of Au/C in 0,1 M KOH at scan rate 50 mV/s

Calculation of the EASA reveals that Au/Ctherm exhibits a higher active area per mg catalyst (A_1 in Table 7) and taking into account that the metal loading on Au/Cox is slightly higher; the EASA (A_2 in Table 7) calculated per mg gold is even higher.

Table 7: Details on the EASA calculation of gold catalysts

catalyst	U (I_C) [V]	U (I_{red}) [V]	Q [mC mg^{-1} cat]	A_1 [cm^2 mg^{-1} cat]	A_2 [cm^2 mg^{-1} Au]
Au/C$_{therm}$	0,93	1,19	0,22	25,32	106,83
Au/C$_{ox}$	0,94	1,17	0,15	17,43	72,01

Despite the slightly higher EASA, the CV of thermal pretreated catalyst shows slightly changed peak characteristics compared to the oxidative pretreated catalyst. The first shoulder from the surface oxidation peaks is more distinct and clearly identifiable as peak in contrast to Au/Cox where the current from surface oxidation appears in plateau shape.

Ethanol oxidation on Ni

The comparison of supported Ni catalyst is rather difficult since the EOR peaks are not completely separated from the currents arising from oxygen evolution. At higher scan rates differentiation between the peaks is hardly possible and peaks are often only a shoulder (Figure 52). This makes it impossible to identify reproducible peak potentials and peak currents.

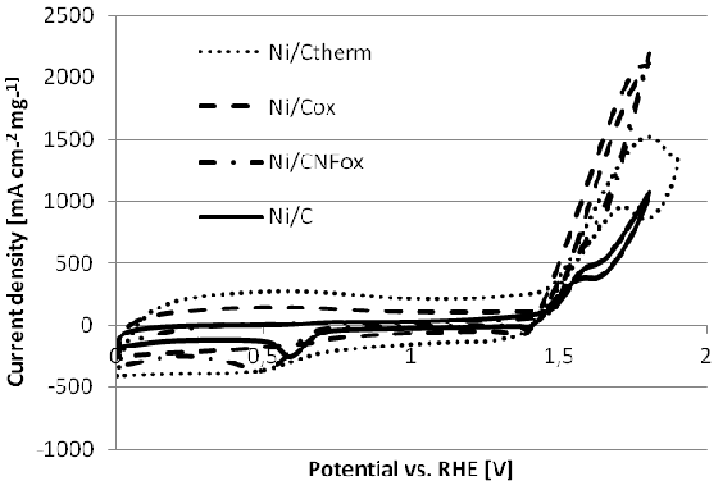

Figure 52: CV of Ni on various carbon supports in 0,1 M KOH + 0,5 M EtOH with 100 mV/s scan rate

The onset potential of the EOR (E_{onset}), which is according to literature supposed to start exactly with the oxide formation, deviates slightly from the start potentials of the oxide formation (E_{oxide}) in KOH solution without ethanol (Table 8, Figure 53). The onset potential on CNF supported Ni catalysts is significantly higher (over 1,4 V). The EOR peak on Ni/CNF exists only as small shoulder in the current from oxygen evolution but becomes visible with the first deviation of the potential-current density function.

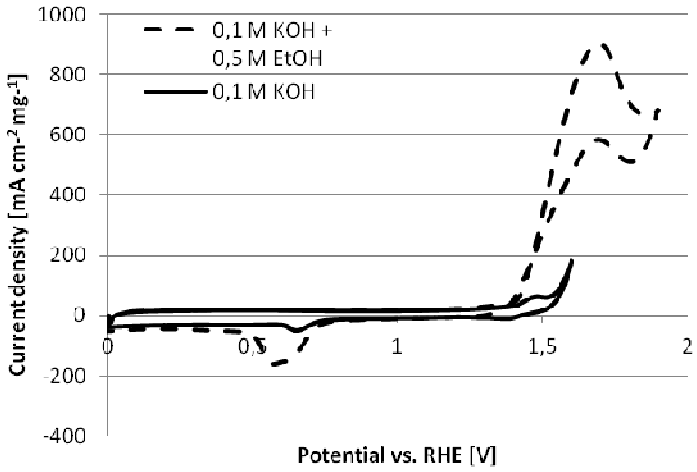

Figure 53: CV of Ni/C_{therm} in 0,1 M KOH (continuous line) and 0,1 M KOH + 0,5 M EtOH (dashed line) at scan rate 10 mV/s

Table 8: Characteristics of the EOR on carbon supported Ni catalysts

catalyst	E_{onset} [V]	E_{oxide} [V]
Ni/C	1,37	1,25
Ni/CNF$_{ox}$	1,41	1,36
Ni/CNF	1,40	not visible
Ni/C$_{ox}$	1,33	1,34
Ni/C$_{therm}$	1,18	1,26
La_2NiO_4	1,31	not visible

Ethanol oxidation on Au

Figure 54 shows a CV of carbon supported gold in 0,1 M KOH + 0,5 M ethanol solution with a scan rate of 10 mV/s. EOR on Au/C$_{ox}$ is clearly visible on sharp peaks on the forward and backward scan. The peak current densities of these oxidation waves are significantly higher than peaks from Au/C and Au/C$_{therm}$. The oxidation waves from Au/C and Au/C$_{therm}$ differ from Au/C$_{ox}$ not only in the height of the peak, but also the shape is dissimilar. The EOR peaks on Au/C and Au/C$_{therm}$ exhibit broad shoulders toward negative potentials, leading to reduced onset potentials (Table 9). The negative shift of the onset potential of 40 mV and the higher current densities at lower potentials can be ascribed to the different forms of gold deposit on Au/C$_{therm}$ and Au/C$_{ox}$. The fine uniformly dispersed gold particles in Au/C$_{ox}$ cause a high surface area and high current densities. The greater diversity of the shapes on Au/C$_{therm}$ leads to particles with different orientation of energy levels which initiate a start of the EOR on lower potentials. Since the high overpotential of the EOR on gold is one of the major obstacles, C$_{therm}$ was chosen was support material for further experiments as basis for a highly active catalyst with low onset potential.

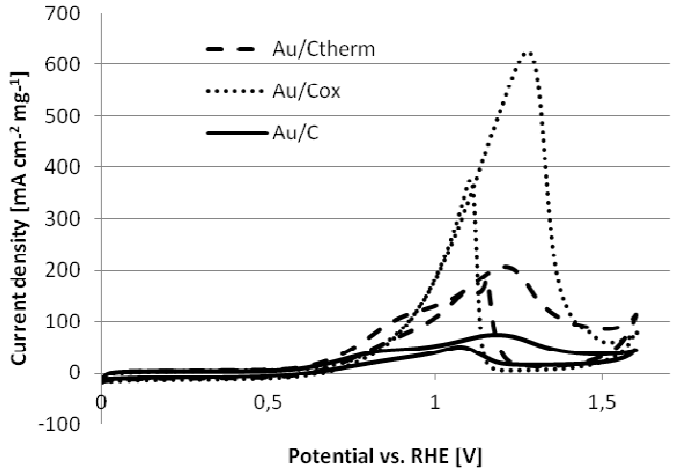

Figure 54: CV of Au/C (continuous line), Au/C$_{therm}$ (dashed line) and Au/C$_{ox}$ in 0,1 M KOH + 0,5 M EtOH with 10 mV/s scan rate

Table 9: Characteristics of the EOR on gold supported by active carbon

	E_{onset} [V]	E_{peak} (f) [V]	E_{peak} (b) [V]	j^{cat}_{peak} (f) [mA cm^{-2} mg^{-1} cat]	j^{Au}_{peak} (f) [mA cm^{-2} μg^{-1} Au]	j^{cat}_{peak} (b) [mA cm^{-2} mg^{-1} cat]	j^{Au}_{peak} (b) [mA cm^{-2} μg^{-1} Au]
Au/C_{therm}	0,50	1,21	1,15	206	0,87	184	0,75
Au/C_{ox}	0,54	1,27	1,11	625	2,58	375	1,55
Au/C	0,51	1,18	1,08	75	0,36	48	0,23

According to the determined peak current densities in CV, the current densities in chronoamperometric experiments on gold catalysts were recorded with oxidative pretreated carbon support (Figure 55). After a quick voltage drop all catalysts were stable for 20 min with degradation rates below 2,3 µA/s for the last 200 s of the experiment.

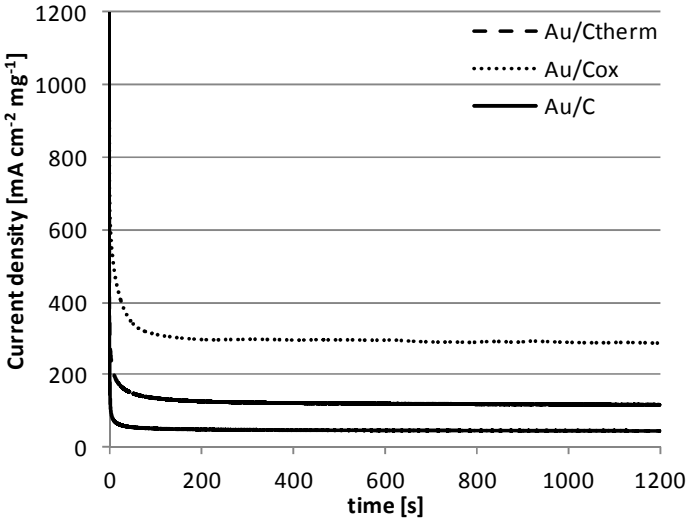

Figure 55: Chronoamperometric diagram of gold on different support materials at 1,2 V

The CA characteristics of Ni on oxidative pretreated support (on Vulcan XC72 and CNF) differ totally from its non or thermally pretreated correspondent (Figure 56 and Figure 57). Instead of a quick drop of the current densitiy as observed on Ni/C_{therm}, Ni/C and Ni/CNF, the current density of oxidative pretreated materials reaches a local maximum after 30 s and starts a continuous decay (Figure 58).

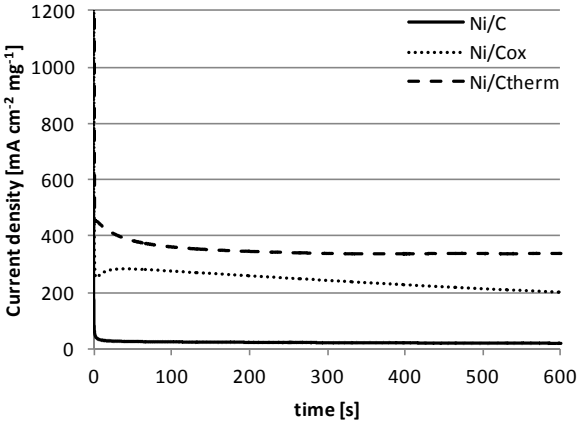

Figure 56: CA with Ni on Vulcan XC72 in 0,1 M KOH + 0,5 M at 1,6 V

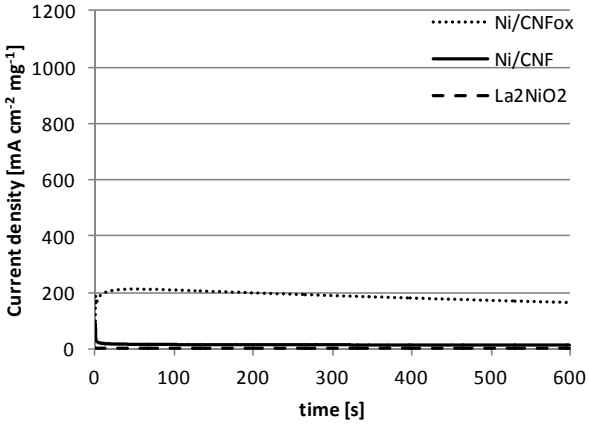

Figure 57: CA of Ni on CNFs and of La_2NiO_2 in 0,1 M KOH + 0,5 M EtOH at 1,6 V

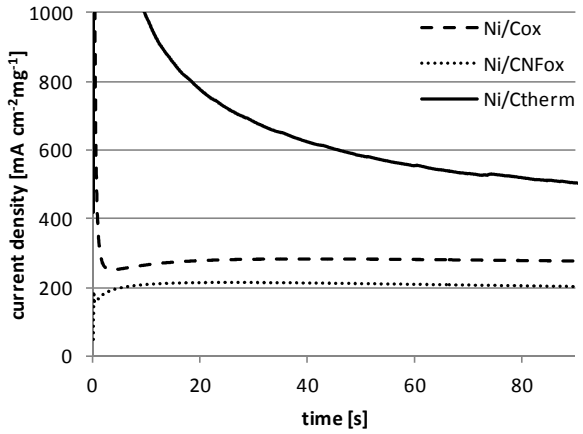

Figure 58: Focus on the first 90 s of the CA experiments of Ni/Ctherm, Ni/Cox and Ni/CNFox

Reasons for this atypical behavior can be found on different Ni phase depositions at different substrates. SEM images revealed that the oxidative pretreated supports are very fine. Additionally, the higher oxygen content on acid pretreated carbon brings a different pH environment on the surface which can cause deposition in a different phase.

Table 10: Limiting current densities from CA experiments of Ni an Au on different support materials

catalyst	applied voltage [V]	current denstiy [mA $cm^{-2}mg^{-1}$]
Au/C	1,2	46,7
Au/Cox	1,2	286,3
Au/Ctherm	1,2	117,3
Au/Cox	1,2	330,1
Au/Ctherm	1,2	106,0
Ni/C	1,5	17,2
Ni/Ctherm	1,5	336,1
Ni/Ctherm	1,8	365,6
Ni/Cox	1,5	198,7
Ni/CNF	1,5	13,3
Ni/CNFox	1,5	165,5

5.2.4. Conclusion

The pretreatment of the carbon support material has a great impact on the activity of the electrocatalyst. This impact is due to different particle sizes, structures and loadings of the metals. For both carbon support materials (Vulcan XC72 and CNFs) the pretreatment enhances the activity of the catalyst and the metal loading. The metal loading on CNFs was extremely low and as a consequence only low current densities were achieved. The conditions for the oxidative treatment of the CNFs were chosen too harsh since the fiber structure was destroyed during the pretreatment. Ni bound in a perovskite type structure did not show a significant activity for the EOR. Ni deposited on oxidative pretreated carbon support shows deviant characteristics in CA experiments. It can be assumed that this behavior can be ascribed to deposition of Ni on these support materials results in an α phase Ni hydroxide and the EOR is overlaid by a slow phase conversion. This assumption could not be proved with the applied methods.

Deposition of gold on different pretreated carbon support materials resulted in different metal structures and activities. Oxidative pretreatment led to a fine dispersion of nanoparticles and high current densities from the EOR. Deposition of gold on thermal pretreated support resulted in a plurality of structures on carbon. Coral like structures, nanoparticles and bigger gold agglomerations were detected. The onset potential of the EOR on C_{therm} lowered due to a higher amount of gold atoms with low orientation and high energy level. Although the peak current density was higher on Au/C_{ox}, C_{therm} was chosen as support material for the following electrocatalysts since the current densities as lower potentials were higher and Ni/C_{therm} exhibited the highest current densities.

5.3. Methods for catalyst preparation

5.3.1. Introduction

One of the most important tools to create an adequate surface for the electrooxidation of organic compounds is the synthesis of the electrocatalyst. Various methods have been developed to maximize the EASA and reduce the metal load. The presence of nanoparticles or similar nanostructured materials such as rods and forms is therefore important. Deposition of metals on carbon supports is mainly realized in electroless deposition techniques since electrodeposition is difficult on this pulverulent material and sputtering techniques are expensive [239]. Metal salts are used as precursors and the deposition of the metal ion on the support material is typically followed by a reduction step. This reduction can be executed in solution by addition of a reducing agent such as sodium borohydride ($NaBH_4$) and ethylene glycol (EG) or by reduction with an reducing gas such as hydrogen. The deposition of the metal on the carbon can be performed by impregnation or precipitation methods. Generally, both methods secure the wetting of the carbon with a solution of the electroactive metal [240].

Impregnation methods involve the distribution of the metal salt solution on the porous support material followed by the removal of the liquid and a calcination or reduction step. For incipient wetness impregnations (IWI) an exactly equal volume of the metal solution as the pore volume is added. This allows the metals to be soaked into the support material and deposit there. This method allows only a small scope to influence the particle shape and distribution and only a small total metal loading can be achieved [241].

Chemical deposition methods can be adapted to a broad spectrum of applications. Under relatively mild conditions and low temperature both supported and unsupported catalysts can be prepared. The precursor salt is reduced to a metallic state and precipitate from the solution [242]. For the production of supported electrocatalysts, the support material is added to the solution prior to the reduction. With the choice of the counter ion to the metal in the precursor salt side e.g. chloride, acetate or nitrate, effects such as surface contaminations can be regulated. Generally, unsupported catalysts exhibit a bigger particle size due to more rapid growth [242].

One important advancement of this method is the possibility to stabilize the metal particles in the solution and avoid therefore big clusters and precipitations. This stabilization of metal particles and as a result nanoparticles with small diameters up to a few nanometers can be achieved with several colloidal routes. Electrostatic stabilization is realized by the interaction of anions with the low coordinated metal surface atoms resulting in an electrical double layer which prevents the combination of neighboring metal clusters by coulombic repulsion [243]. Stabilisation of the metal particles with citrate is a typical example for this kind of stabilization. Steric stabilization is achieved by the introduction of bulky organic molecules. The nanometallic catalyst synthesis route with tetraalkylammonium halides as stabilization agent is generally known as Bönnemann method [244,245].

An effective way to reduce the size of the metal particles is the water in oil (w/o) microemulsion method [241]. A w/o microemulsion is a thermodynamically stable dispersion of an aqueous and an organic phase with a surfactant [246]. The aqueous phase is placed in nanosized micelles formed by the surfactant surrounded by a continuous organic phase. For the preparation of metal nanoparticles two of these microemulsions with one containing the metal salts in the aqueous phase and the other containing the reducing agent in the aqueous phase were mixed together. The hindered contact of the metal with the reducing agent results in slow particle growth and many nucleation sides and finally in highly dispersed nanoparticles (Figure 59).

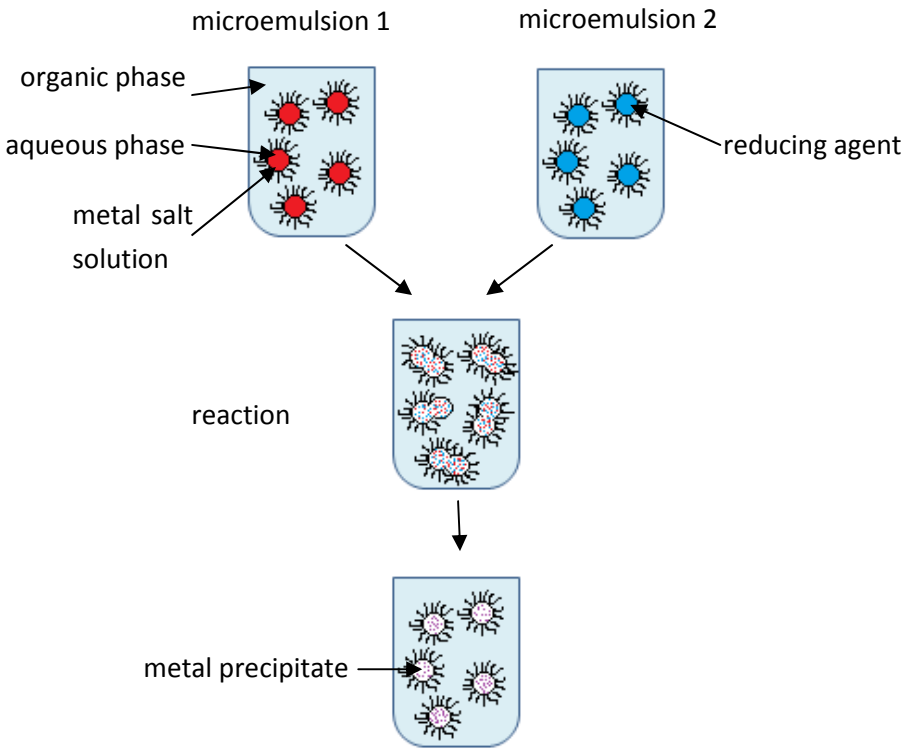

Figure 59: Scheme of the water in oil microemulsion preparation

5.3.2. Experimental

Catalyst preparation

For the one-step synthesis gold(III) chloride trihydrate ($AuCl_3*3H_2O$) and nickel(II)nitrate hexahydrate ($Ni(NO_3)_2*6H_2O$) were diluted with H_2O_{deion} to 0,1 M solutions. The pretreated or non-pretreated carbon support materials were dispersed in 0,2 M citric acid in the ultrasonic bath and an aqueous solution of the metal ion was added to reach nominally 30 wt% metal. This solution was heated until a temperature of 60°C was reached, then an excess of $NaBH_4$ was added and stirred for 6 hours. Finally, the catalysts were washed with deionised water and dried at 80°C.

For the two-step synthesis two microemulsions with the same water-oil- and surfactant composition were prepared. 1 ml of heptane forms the oil phase. The volumetric ratio between water and

surfactant was 4:1. 1,25 ml of Brij30 were as surfactant and 5 ml of deionised water (R= 18MΩ) were added. To one of the microemulsions the precursor salt gold(III) chloride trihydrate ($AuCl_3*3H_2O$) or nickel(II)nitrate hexahydrate ($Ni(NO_3)_2*6H_2O$) was added to form an approximate concentration of 0,2 M in the aqueous phase. In the second microemulsion $NaBH_4$ as reducing agent was added. The molar ratio of $NaBH_4$ to metal was 15:1. These two microemulsions were mixed together. As soon as the two gels got contact, the before colored metal solutions blackened. An appropriate amount of carbon support was added to form a metal loading of 30% wt%. The mix was stirred at room temperature for 3 hours. Subsequently, the substance was transferred onto a black ribbon filter paper and washed with acetone. After removal of the surfactant, the catalyst was washed with ethanol and water and dried at 80°C. The procedure was adapted from [247].

The catalysts were dispersed in a solution of isopropanol and Nafion in the ultrasonic bath for 30 min. A distinct volume of this ink was transferred to a glassy carbon disk electrode and dried.

Characterization

The catalysts were examined electrochemically and physically. Electrochemical characterization was performed in 0,1 M KOH solutions with cyclic voltammography in order to calculate the surface area or in the case of Ni the surface charge. The catalytic activity towards the EOR was examined in 0,1 M KOH + 0,5 M EtOH solutions with CV and chronoamperometric measurements. The morphology of the catalysts was studied with SEM and the metal loadings were verified with ICP-OES.

5.3.3. Results

Metal loading

The applied synthesis protocol has a great impact on the metal loading of the catalysts, but the impact is strongly dependent on the metal. The nickel loading was significantly enhanced by the application of the two-step protocol. The Ni deposition was tripled from the especial low value of 13 mg/g on C_{therm}. For gold the effect is contrary. Application of the two phase synthesis resulted in a significantly lower gold loading.

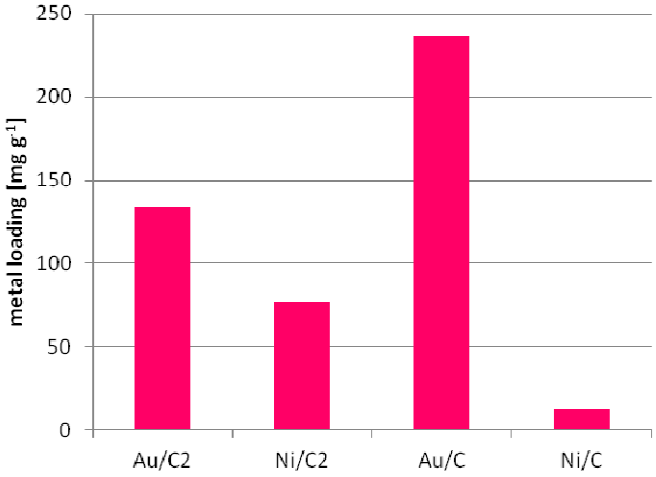

Figure 60: Metal loadings of Ni and Au catalysts prepared with one-step and two-step protocols. All catalysts were prepared on C_{therm}.

Morphology

SEM analysis of the gold catalysts showed that the metal deposition did not result in the desired fine distribution of gold nanoparticles, but in a partial coverage of the carbon particles with a nanostructured gold deposit (Figure 61). This film like coverage of random parts of the carbon particles exhibits a sponge like agglomeration of gold nanoparticles. A great number of pores is visible on the maginifed SEM image throughout the deposit.

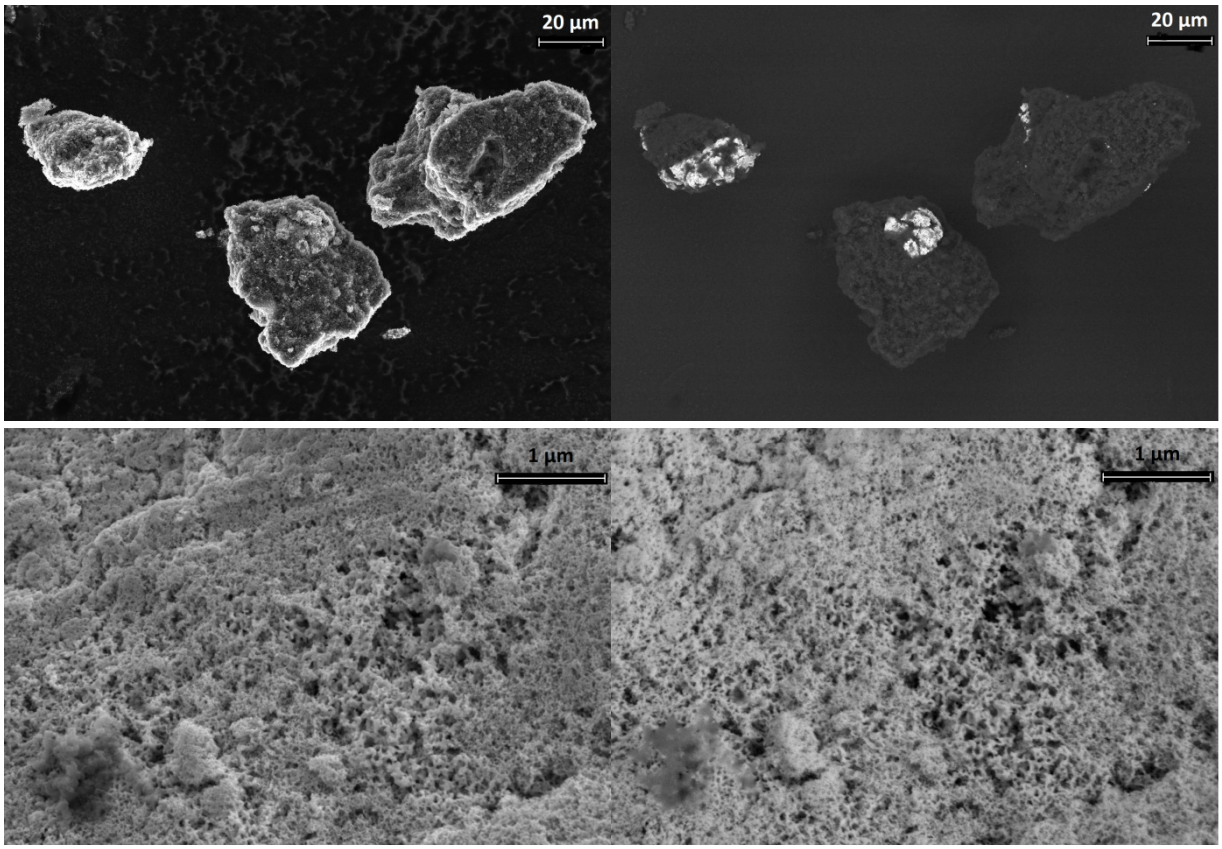

Figure 61: SEM images of the Au catalyst prepared with a two-step synthesis. The first row represents an overview of the catalyst probe and on the second a detail study of the catalyst surface. The images on the left side were recorded with an InLens detector in order to display the fine structure of the sample, the image on the right side shows the identical detail recorded with an AsB detector.

A better distribution of the gold deposit is preferable. An improvement of the method in order to receive a better distribution on the carbon particles can be achieved by a larger amount of microemulsion compared to the amount of carbon support material during the synthesis.

Electrochemical characterization

CV

The current densities arising from surface changes in 0,1 M KOH are significantly higher on the gold catalyst prepared by the two-step synthesis (Figure 62). Although this can be ascribed to the enhancement of the electrocatalytic surface area, it has to be kept in mind that the changed synthesis method resulted in partial coverage of the carbon particles instead of a fine distribution of gold particles. This implies that the amount of gold the small sample which is taken for the electrochemical characterizations may vary stronger. The quantitative results from the ICP-OES are more trustworthy since a bigger amount of catalyst was used which should adjust the unsteadiness. Nevertheless, comparing several CV measurements in KOH and EtOH, a significant gain in active gold surface can be ascertained.

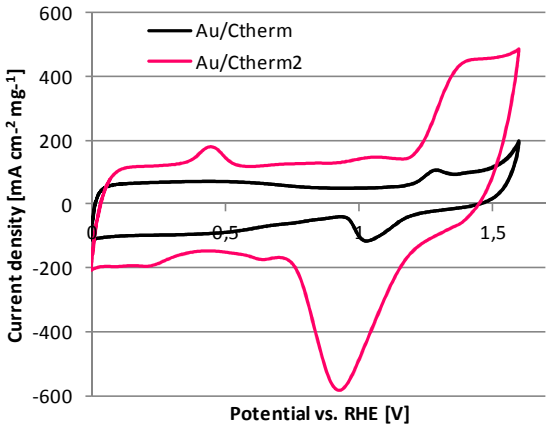

Figure 62: CV of Au/Ctherm and Au/C_{therm}2 in 0,1 M KOH with a scan rate of 50 mV/s

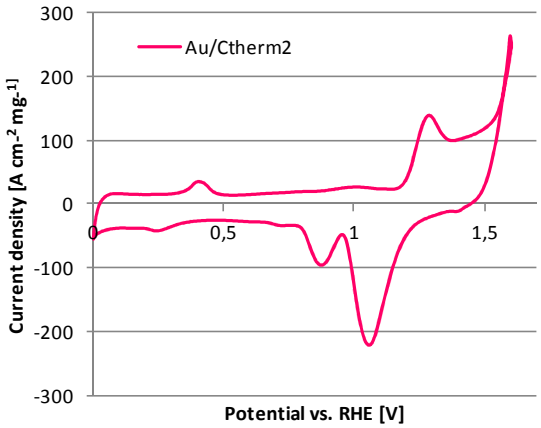

Figure 63: CV of Au/C_{therm}2 in 0,1 M KOH with a scan rate of 10 mV/s

The plurality of oxidation and reduction peaks is a sign of different orientation and oxidation states of the gold deposit. Starting at 1 V, the slight current increase can be attributed to the so-called premonolayer oxidation [127]. When scanned with a lower rate (10 mV), the gold oxide reduction peak separates into two (Figure 63). The size of the area of this peak is comparable to the enlarged first wave at the surface oxide formation plateau. Additionally to these reduction peak, a small single peak appears at 0,4 V in all electrolytes (Figure 62, Figure 63 and Figure 64) which is not visible at catalysts prepared by one step.

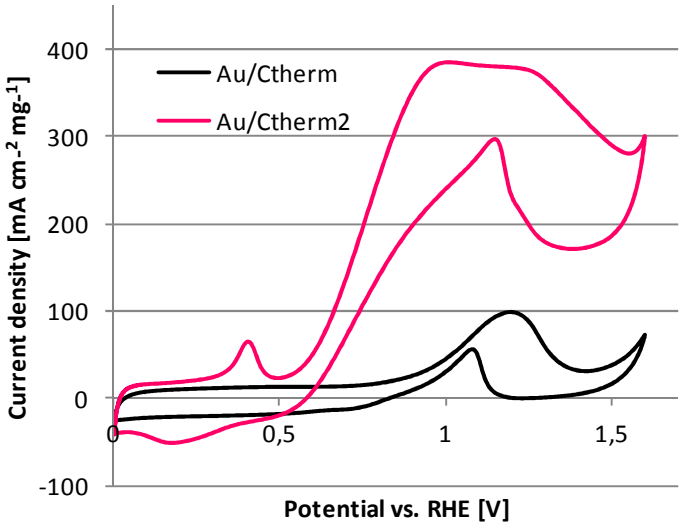

Figure 64: CV of Au/Ctherm and Au/C_{therm}2 in 0,1 M KOH 0,5 M EtOH with a scan rate of 50 mV/s

The start of the EOR is strongly shifted to lower potentials at Au/C_{therm}2. The onset potential is on 0,5 V. The currents from the EOR do not result in a distinct peak but in a plateau (Figure 64). The highest current density is nearly 4-fold compared to Au/C_{therm} and the potential range is doubled.

CA

All catalysts prepared on C_{therm} with a two-step synthesis are stable after 10 minutes (Figure 66). The highest limiting current density recorded on Au/C_{therm}2 (Table 11).

Table 11: Limiting current densities derived from CA experiments

catalyst	applied voltage [V]	current denstiy [mA $cm^{-2}mg^{-1}$]
Au/C_{therm}	1,2	117,3
Au/C_{therm}2	1,2	106,0
Au/C_{ox}2	1,2	110,6
Ni/C_{therm}2	1,6	121,1
Ni/C_{ox}2	1,6	111,5
Au/C_{therm}2	1,2	230,7

Compared to Au/C_{therm}, Au/C_{therm}2 exhibits not only a higher current density during CA, additionally the degradation rate is also significantly reduced (Figure 65). The limiting current density of Ni/C_{ox}2 is significantly lower than the gold catalysts and Ni/C_{therm}2. Ni/C_{therm}2 exhibits a similar performance as Au/C_{ox}2 but at a higher fixed potential. The best performance was attained by Au/C_{therm}2.

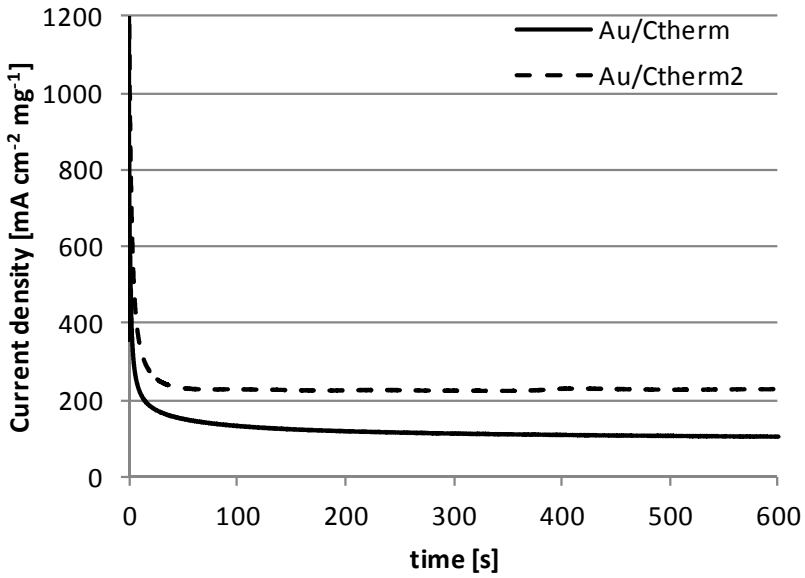

Figure 65: Comparison of Au/C prepared with a one-step synthesis and a two-step synthesis. The experiment was performed in 0,1 M KOH and 0,5 M EtOH at a fixed potential at 1,2 V.

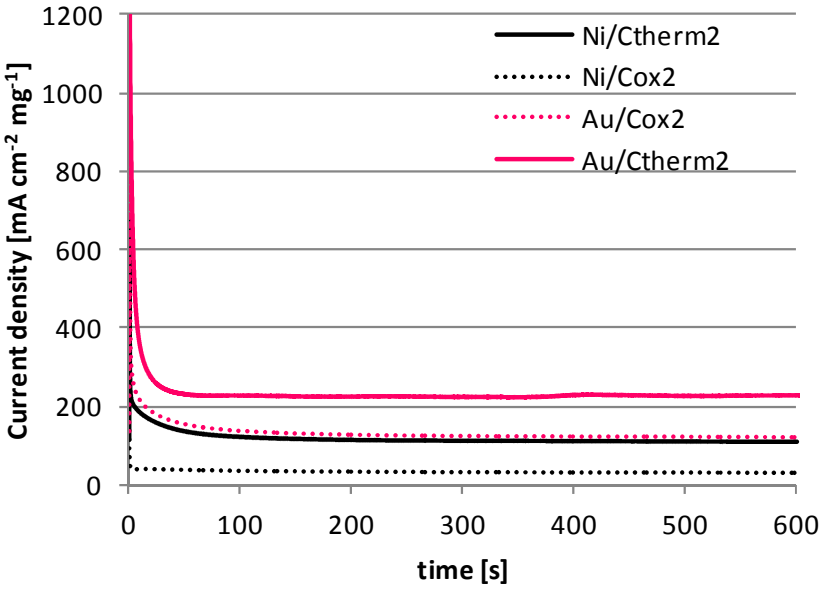

Figure 66: CA of Au/C and Ni/C catalysts prepared by the two-step synthesis. The experiment was performed in 0,1 M KOH and 0,5 M EtOH at a fixed potential at 1,6 V for Ni and 1,2V for Au.

5.3.4. Conclusion

Although the method is not fully developed and optimized, an enhancement in stability and higher currents can be achieved by application of the two-step synthesis. The structured surface of gold deposits enlarges the active surface and results in higher currents. The impact on Ni deposition is not as pronounced as on gold since Ni deposits are not as compact as gold. The Ni loading on Ni/$C_{therm}2$ is significantly higher than on Ni/C_{therm}. The highest limiting current densities were achieved on Au/$C_{therm}2$. But still the method needs further optimization and adaption of the amount of material to the volume of the microemulsion.

5.4. Bimetallic catalysts

5.4.1. Introduction

The electrocatalysis of the EOR has still much space for improvements. Since no single metal is capable to fulfill all requirements for an efficient oxidation reaction it seems intuitive to combine different kinds of metals in order to take advantage of their specific properties. Catalysts for the DEFC have to break a C-C bond, a C-O bond and have to withstand poisoning by CO species. In order to perform this task, a multifunctional catalyst has to be employed. PtRu is the most popular bimetallic catalyst system for fuel cells. Pt is known to be rapidly poisoned by adsorbing species such as CO from fuel impurities or mediates. The presence of Ru promotes the oxidation of CO to CO_2 by increased OH adsorption. PtRu is widely used for fuel cells operated with methanol or reformate [242]. In contrast to the MOR, the EOR is only poorly improved by the addition of Ru to Pt [248]. For acid DEFCs, PtSn catalyst show great promise for improved reaction kinetics [96,248,249].

Bimetallic catalysts exist as alloys and two-phase catalysts. Alloys exhibit a homogeneous distribution of the metals at the atomic level. The lattices of the metals have to be compatible to an alloy. Information on miscible gaps and the existence of bulk alloys is provided for interesting combinations of metals in phase diagrams. Alloying changes the reactivity of the metal compared to the pure state by changing the electronic structure and the d-band center [249].

The AuNi phase diagram is dominated by a large miscibility gap in the solid state [250]. At temperatures below 227°C the bulk phase is immiscible [251]. Low temperature catalyst preparation methods therefore lead to a mixture of monometallic nanoparticles rather than homogeneous alloys on atomic level. However, the composition on the surface can be substantially different than on the bulk.

The application of both metals as alloy or co-deposit solves several problems of the catalysis of the EOR at once. The peak current of the EOR catalyzed by gold occurs earlier than by nickel, but the produced current is considerably lower as compared to nickel. The combination of these two metals allows the EOR to take place at a broader potential range.

The preparation of bimetallic catalysts can be conducted via one-step and two-step synthesis methods [242]. A typical method is the codeposition of two metals. Codeposition involves the simultaneous reduction of two solved precursor salts by a strong reducing agent leading to a homogeneous distribution of the metals on the support surface. A very rapid and simultaneous reduction of the metals is a prerequisite for a uniform distribution and is realized by a large excess of a strong reducing agent. Application of a two-phase synthesis is more likely to result in a phase segregated catalyst. Considerations on the nobility and the redox potentials of the metals are important. A two phase synthesis is conducted via the subsequent reduction of the precursor salts. If the second metal is nobler than the already deposited metal, the deposition of the second metal can also be performed via a redox reaction or also often referred to as galvanic replacement reaction. This methods are based on the spontaneous replacement of the less noble metal by a more noble

metal [252]. The inexpensive metal is deposited by any conventional methods on the support metal and subsequently immersed in a solution of the precursor salt of the second metal [253]. This leads to the following reaction:

$$3\ Ni/C\ + 2\ AuCl_3\ \rightarrow 2\ Au(Ni)/C\ + 2\ Ni^{2+} + \ 6\ Cl^-$$

The surface of the catalyst is then covered with a layer of the more noble metal in a solution of the less noble metal.

In this chapter all three methods were applied on the AuNi/C system and characterized.

5.4.2. Experimental

Catalyst preparation

AuNi/C catalysts were synthesized with different methods and support materials. The in chapter 5.2. described oxidative and thermal pretreated Vulcan XC72 support materials (C_{ox} and C_{therm}) were used. For the codeposited bimetallic catalyst (AuNi/C_{co}) the precursor salts gold (III) chloride trihydrate ($AuCl_3$*$3H_2O$) and nickel (II) nitrate hexahydrate ($Ni(NO_3)_2$*$6H_2O$) were mixed together in equal weight amounts and reduced simultaneously either by a one-step synthesis or a two-step synthesis as described in the previous chapter. The aimed metal loads were 15% Ni and 15% Au.

AuNi/C catalysts prepared by subsequent reduction of the metals are named with the suffix on. First a Ni/C catalyst with a nominal metal loading of 21,4 % was prepared with either a one-step or two-step synthesis method. On this material the same amount of Au was deposited with the same method in order to reach a total metal loading of 30% on the carbon support material with half Au and half Ni.

For the AuNi/C catalyst prepared via an electroless replacement reaction, a 30% Ni/C catalyst was prepared by a two-step synthesis. 100 mg of this Ni/C catalyst were placed in a beaker with 20 ml of H_2O_{deion} and 2 ml of 25% HCl and $AuCl_3$*$3H_2O$ were added. After one hour the greenish liquid was removed and the catalyst dried in an oven at 80°C.

Table 12: Preparation of bimetallic catalysts

catalyst	support	steps synthesis	method	Nominal metal loading [w%]	
				Au	Ni
AuNi/C_{therm}co	C_{therm}	1	co	15	15
AuNi/C_{therm}on	C_{therm}	1	on	15	15
AuNi/C_{therm}gal	C_{therm}	1	gal	15	15
AuNi/C_{therm}2co	C_{therm}	2	co	15	15
AuNi/C_{therm}2on	C_{therm}	2	on	15	15
AuNi/C_{therm}2gal	C_{therm}	2	gal	15	15

AuNi/C_{ox}2on	C_{ox}	2	on	15	15
AuNi/C_{ox}2co	C_{ox}	2	co	15	15

For the electrochemical characterization the catalysts were dispersed in a solution of isopropanol and Nafion in the ultrasonic bath for 30 min. A distinct volume of this ink was transferred to a glassy carbon disk electrode and dried at room temperature.

Characterization

The catalysts were examined electrochemically and physically. Electrochemical characterization was performed in 0,1 M KOH solutions with cyclic voltammography in order to calculate the surface area or in the case of Ni the surface charge. The catalytic activity towards the EOR was examined in 0,1 M KOH + 0,5 M EtOH solutions with CV and chronoamperometric measurements. The morphology of the catalysts was studied with SEM and the metal loadings were verified with ICP-OES.

5.4.3. Results

Metal loading

Elemental analysis of the catalysts with ICP OES reveals that the metal loading of both Ni and Au is very low on catalysts prepared with codeposition (Figure 67). The subsequent reduction of metal salts (AuNi/C_{therm2}on) yields in higher metal loadings for both Ni and Au. Remarkable is the reduction of the Ni content (termed Ni(pre) in Figure 67) of the Ni/C precursor by the deposition of Au. Similar can be observed with the Ni/C precursor for AuNi/C_{therm2}gal, but in contrary to AuNi/C_{therm2}on this effect is deliberate. In comparison, the by far highest Au loadings were obtained by galvanic replacement of Ni.

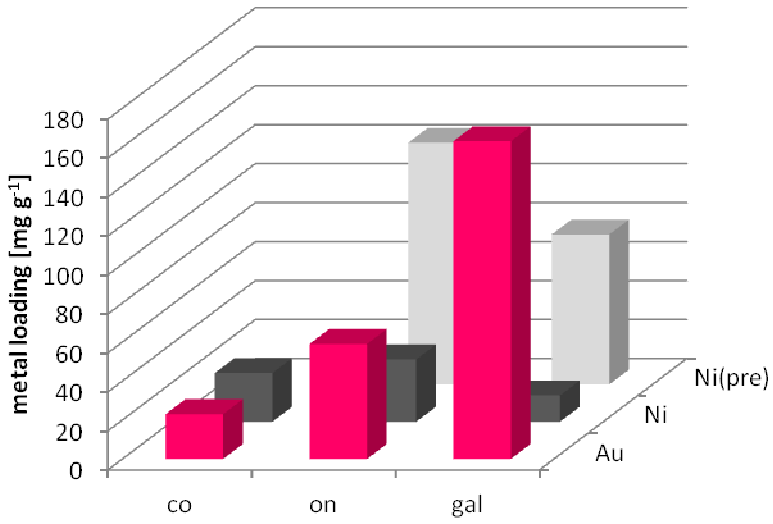

Figure 67: Metal loadings of Au and Ni on codeposited AuNi on C_{therm} with a two-step synthesis (AuNi/C_{therm2}co), subsequently deposited AuNi on C_{therm} with a two-step synthesis (AuNi/C_{therm2}on) and galvanically deposited Au on Ni/C_{therm} (AuNi/C_{therm2}gal). Ni(pre) shows the Ni content of the Ni/C precursor materials for the bimetallic catalysts.

Morphology

Investigation of the bimetallic catalysts with SEM and EDX shows that gold and nickel do not form homogeneously distributed bimetallic catalysts but form well specifiable deposits. Ni is hardly detectable in the SEM images, but EDX analysis proofed the existence of Ni deposits (Figure 68). The detection of small amounts of Ni all over the carbon support leads to the assumption, that the carbon support is soaked with the metal and is covered with a very thin Ni film.

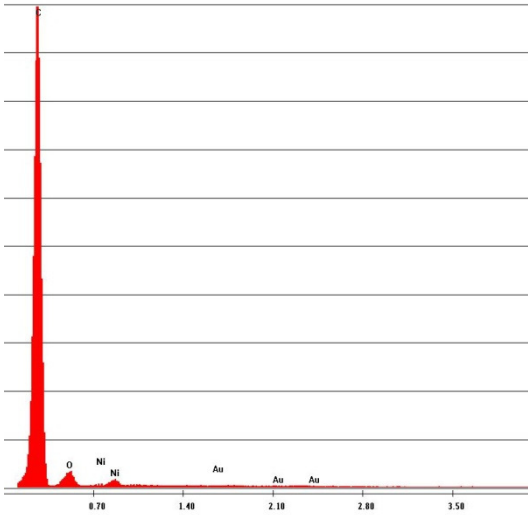

Figure 68: EDX pattern of the carbon support of AuNi/C_{on}.

Examination of the gold deposit morphologies revealed that the influence of the carbon support is despite different preparation methods decisive. Co- and subsequentially deposited AuNi/C showed the same phenomena of gold on thermally pretreated carbon support as described in chapter 5.2. Gold deposits are visible in form of fine dispersed nanoparticles, coral like structures and metal plates (Figure 69). EDX analysis of these structures confirmed that no Ni is present in this agglomerates. The light grey colors on the AsB detected SEM pictures (left row in Figure 69) indicate the presence on Ni throughout the particle, except of a few black areas. The gold deposition of AuNi/C_{on} is very inhomogeneous.

The metal deposition of the galvanically deposited AuNi/C exhibits a strongly different behavior (e and f in Figure 69). The dark background of the AsB detected SEM picture indicates hardly any Ni depositions are present. Gold is deposited in large spherical particles with diameters up to 500 nm.

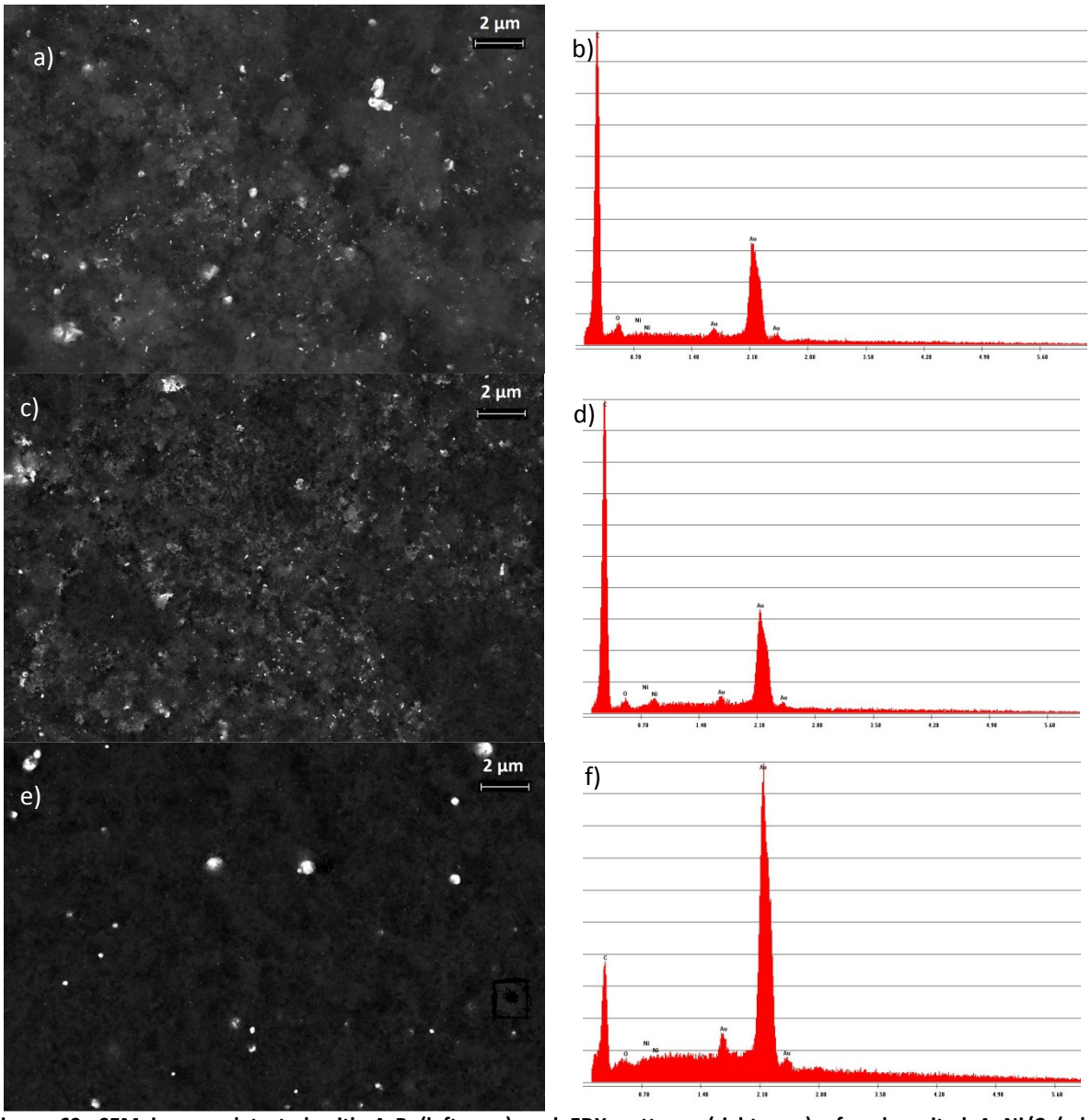

Figure 69: SEM images detected with AsB (left row) and EDX patterns (right row) of codeposited AuNi/C (a,b), subsequentially deposited AuNi/C (c,d) and galvanically deposited AuNi/C (e,f) with a one-step synthesis. Thermally pretreated Vulcan XC72 was used for all samples.

Electrochemical characterization

CV

Characterization of AuNi/C in 0,1 M KOH with CV shows that the bimetallic catalyst combines the characteristica of both metals (Figure 70). The oxidation and reduction peaks according to the Ni oxidation reaction at 1,5 V and 1,4 V are as well visible as the peaks according to the gold oxidation an reduction at 1,3 and 1 V.

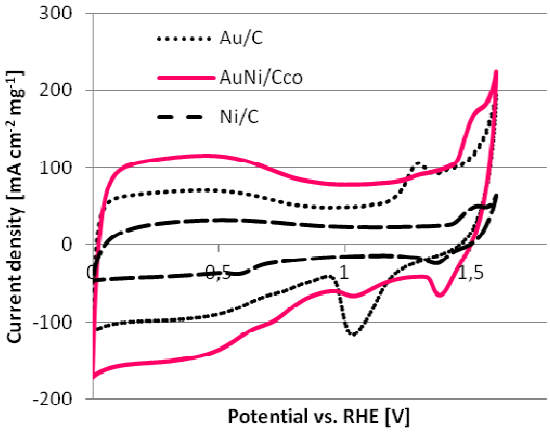

Figure 70: Comparison of the CV characteristica of Au/C and Ni/C with AuNi/C_{co} in 0,1 M KOH with 50 mV/s scan rate. Thermally pretreated Vulcan XC72 was used as carbon support for all three catalysts.

Comparison of the preparation method of the bimetallic catalyst requests a differentiation between the application of the one step synthesis and the two step synthesis. For bimetallic catalysts prepared within one step, the subsequentially deposited Au on Ni/C exhibits the most striking features (left diagram of Figure 71). The pronounced Ni surface oxidation and reduction peaks dominate the CV in KOH. Au surface oxidation is only slightly remarkable as shoulders at lower potential regions. As already indicated by SEM investigations, currents of surface reactions on galvanically deposited Au on Ni/C are rather low due to low Ni deposition and strong Au agglomeration.

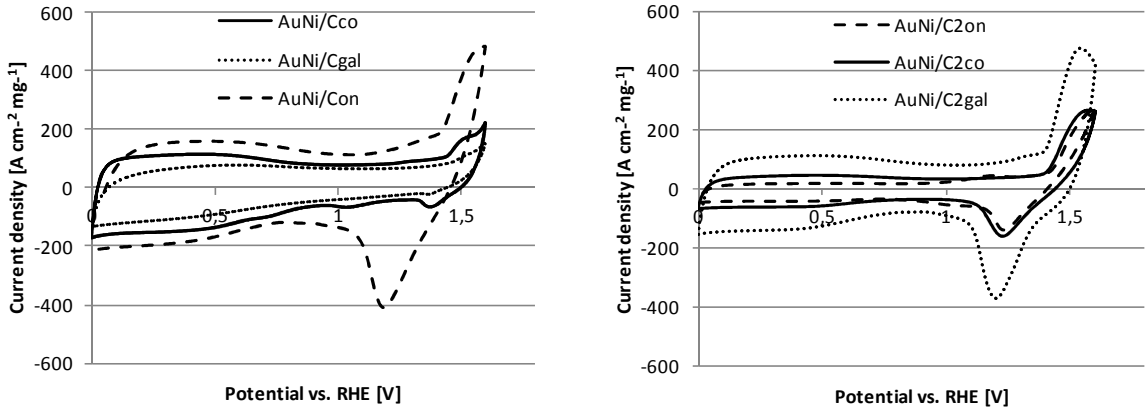

Figure 71: CVs of AuNi/C prepared by different methods in 0,1 M KOH with 50 mV scan rate. The left diagram shows a CV of AuNi/C prepared with a one-step synthesis, the CV on the right side shows a CV of AuNi/C prepared by a two-step synthesis. Thermally pretreated Vulcan XC72 was used as carbon support for all three catalysts.

For bimetallic catalysts prepared with a two-step synthesis, the galvanically deposited Au on Ni/C catalyst exhibits the highest surface oxidation and reduction currents. Ni surface oxidation currents are very high, despite the low Ni loading measured with ICP-OES (Figure 67). CVs for AuNi/$C2_{on}$ and AuNi/$C2_{co}$ are similar. As expected, AuNi/$C2_{on}$ shows slightly higher oxidation currents from gold compared to AuNi/$C2_{co}$.

Ethanol oxidation on AuNi/C catalysts takes place on the same potential ranges as the single metals do. In this case it means that the EOR takes place between 0,6 V and the oxygen evolution region with a short interruption at 1,4. Figure 72 shows the influences of the preparation method on the EOR activity. The highest peak current densities were achieved according to the highest current densities from the surface oxide formation: AuNi/Con prepared with a one-step synthesis and AuNi/C_{gal} prepared with a two-step synthesis.

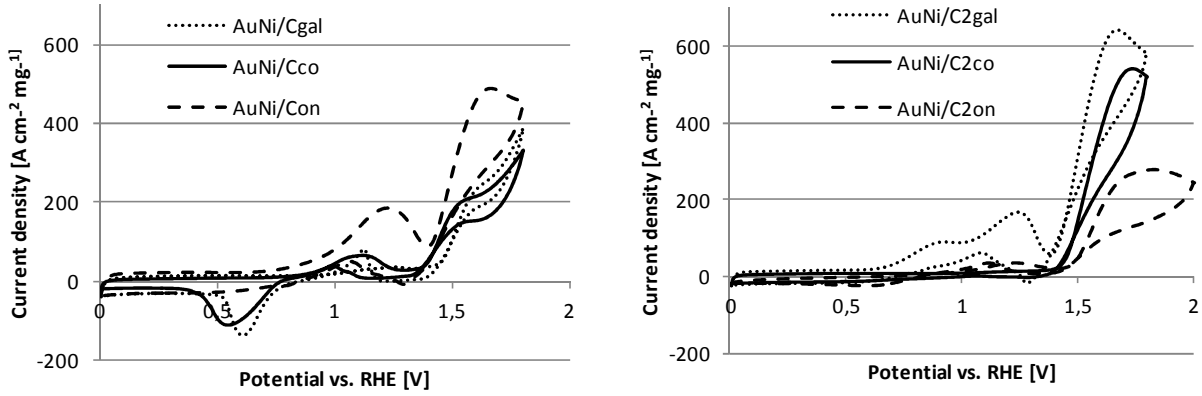

Figure 72: CVs of AuNi/C prepared by different methods in 0,1 M KOH + 0,5 M EtOH with 10 mV scan rate. The left diagram shows a CV of AuNi/C prepared with a one-step synthesis, the CV on the right side shows a CV of AuNi/C prepared by a two-step synthesis. Thermally pretreated Vulcan XC72 was used as carbon support for all three catalysts.

Comparison of this two catalysts shows that the onset potential for the bimetallic catalyst prepared with a two-step synthesis is shifted to a lower potential region. The peak current density at the gold region is slightly higher at AuNi/C_{therm}on, but the peak current densities in the nickel region are higher on AuNi/C_{therm}2gal (Figure 73). Regarding the EOR onset potentials, AuNi/C_{therm}2co and AuNi/C_{therm}gal exhibit exceptional high values for the beginning of the reaction (Table 13). A closer look at the CVs of AuNi/C_{therm}2co reveals that this catalyst is lacking a gold region and the determined value can be ascribed to the onset potential on the Ni part of the catalyst. The high onset potential on AuNi/C_{therm}gal can be explained by the high particle size of the gold deposits (Figure 69e).

Table 13: Onset potentials of AuNi/C catalysts

catalyst	E_{on} [V]
AuNi/C_{therm}co	0,61
AuNi/C_{therm}on	0,62
AuNi/C_{therm}gal	0,82
AuNi/C_{therm}2co	1,32
AuNi/C_{therm}2on	0,72
AuNi/C_{therm}2gal	0,54

The high peak current density of AuNi/C_{therm}2gal can be explained by the preparation method. The two-step protocol yields in high nickel loadings. As shown on SEM images in chapter 5.3. , the metal deposits exhibit foam like structure. This nickel sponge structure offers a big surface area for the galvanic replacement reaction with gold and can additionally capture gold ions from the solution.

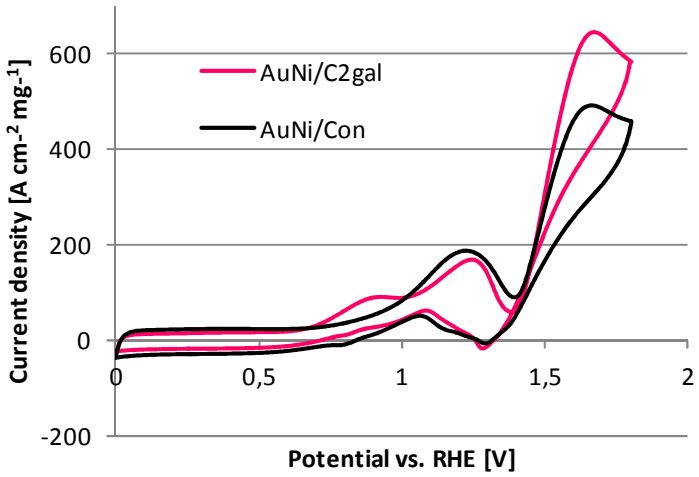

Figure 73: Comparison of CVs of AuNi/C2gal and AuNi/Con in in 0,1 M KOH + 0,5 M KOH (red line) with 10 mV/s scan rate.

All CVs exhibit a potential region with inhibited EOR (Figure 74). This region can be described as the potentials right before the start of the NiOOH formation. Shoulders in the gold EOR peaks on the backward scans originate from overlaps with surface oxide reduction peaks from both Ni and Au.

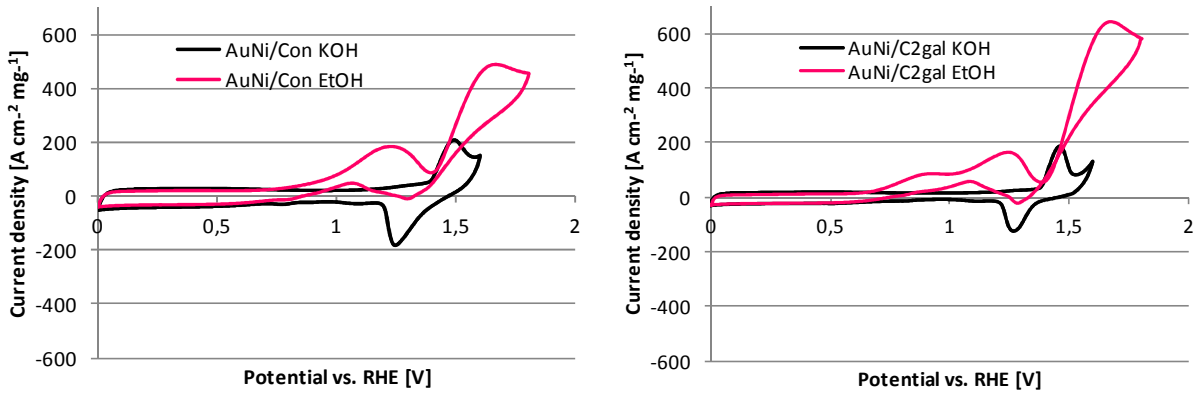

Figure 74: AuNi/Con (left diagram) and AuNi/C2gal (right diagram) in 0,1 M KOH (black line) and in 0,1 M KOH + 0,5 M KOH (red line).

When compared to the CVs of the single metals, the bimetallic catalyst reveals several positive changes (Figure 75). The peak current densities of both the Ni and Au regions are higher, although only half of the mount of the metal is used for the preparation. The onset potential on the Ni region is shifted to significantly lower potentials then on the single metal.

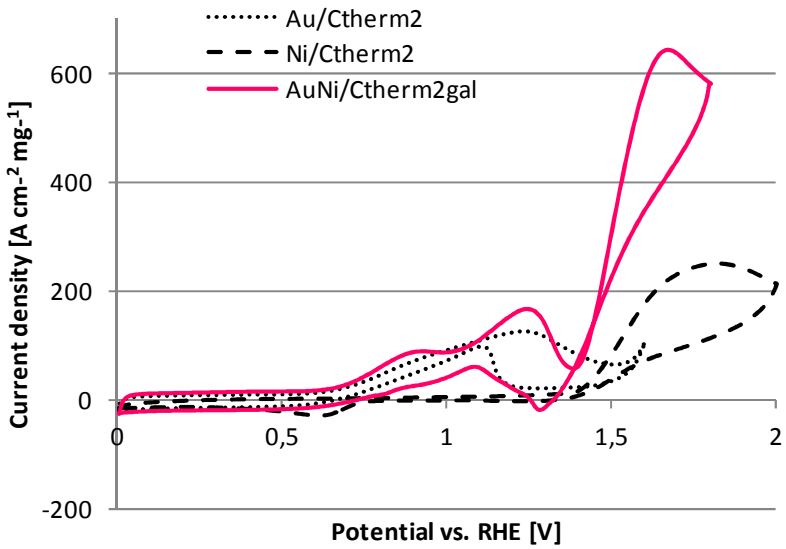

Figure 75: CV of AuNi/C in comparison with Au/C and Ni/C in 0,1 M KOH and 0,5 M EtOH with a scan rate of 10 mV/s

CA

Similar characteristics of the EOR on AuNi/C catalysts can be observed at the characterization with chronoamperometric methods (Figure 76 and Figure 77). The potential was set at 1,6 V and the current density was recorded for 10 min. After a quick current drop at the start of the measurement, the AuNi/C_{therm}2 catalysts reached a stable value and the current density does not further decrease. AuNi/C_{therm} catalysts had not reached a stable level after 600s and a slight decrease is still visible. The order of the catalysts regarding the preparation method which reached the highest current densities did not change compared to result from CV measurements.

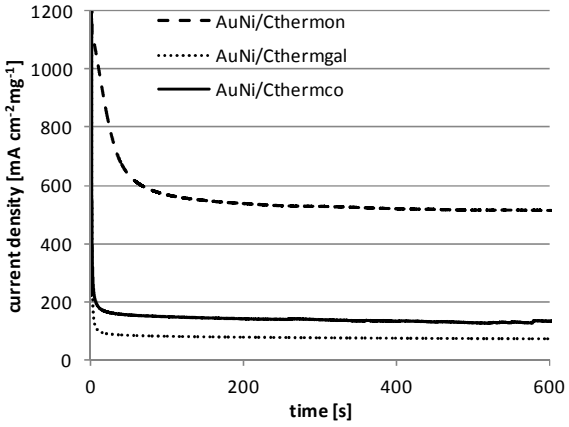

Figure 76: CA with AuNi/Ctherm catalysts prepared by a one-step synthesis at 1,6 V

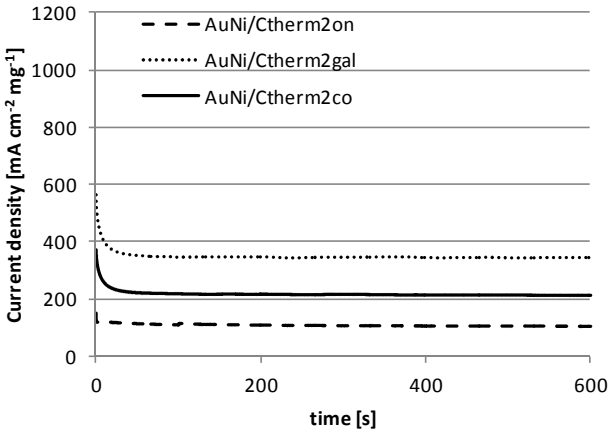

Figure 77: CA with AuNi/Ctherm catalysts prepared by a two-step synthesis at 1,6 V

Especially for bimetallic the limiting current density is not only interesting for one single potential which only displays the area of influence of one part of the catalyst. Therefore, the limiting current density was determined for potentials between 0,4 V and 1,8 V. The limiting current densities were calculated by the arithmetic mean of the last 100s.

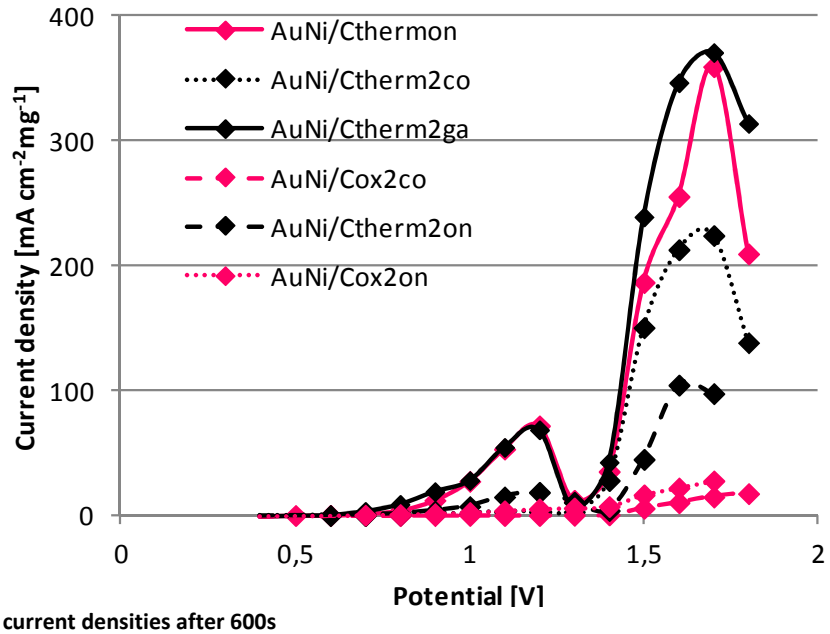

Figure 78: Limiting current densities after 600s

The shape of the interpolated limiting current densities resembles the shape of the according CVs with lower current densities due to the strong catalyst deactivation after the first seconds. Between the two peaks according to the peak region of Ni and Au a minimum with current densities near zero can be observed.

5.4.4. Conclusion

The application of two different metals with different EOR active potential regions in one electrocatalyst results in a broader potential range for the EOR. Additionally, the use of Au and Ni simultaneously delivered higher amounts of current than with single metals even though only half of the amount of metal was used for preparation. Although the onset potential on Ni is strongly lowered, the overpotential is still very high. Regarding the cost of the metals, the use of bimetallic catalysts is still reasonable because gold can be replaced to a certain extent by the cheap metal nickel without loss on activity. CA experiments showed that the AuNi are stable and do not decrease further after a quick voltage drop at the start for 10 min during EOR.

6. Conclusion

This thesis investigated PGM free catalysts for the electrocatalysis of the EOR in alkaline DEFCS. Summing up, the theoretic work can be divided in four big chapters:

- AFCs
- DAFCs
- Ethanol production
- Electrocatalysts for the EOR

Basic knowledge on alkaline fuel cells and direct alcohol fuel cells are covered and the possibilities for a sustainable ethanol production were investigated. In theory, alkaline fuel cells offer significant advantages over its acid correspondents, but a lack of research in particular in the development of adequate materials prevent this technology from an economical implementation. For a successful application of a DEFC new materials are required. The main advantage of operation in alkaline environment is the improvement of the electrokinetic properties in particular of the oxygen reduction. Additionally, the choice of the catalyst material is not bound on Pt and Pd which are the only metals which exhibit a reasonable stability in acid media, but is free for all transition metals and main group elements. The facilitation of oxidation and reduction reactions allows the direct electrochemical conversion of more complex fuels such as ethanol. Direct alcohol fuel cells generate electricity by direct oxidation of organic compounds without a preceding reforming step of the fuel. The direct use of alcohols in fuel cells opens up the opportunity to avoid efficiency losses from fuel processing, in particular the production of hydrogen. Additionally, the simple system set up at low temperatures and no pressurized tanks make DAFCs perfectly suitable for portable applications. Efficient direct oxidation of ethanol leads to fuel cells with convenient storable fuel and to a system with high energy density and low emissions. Ethanol is an eligible fuel since it is not toxic, has a high energy density of 8,01 kWh kg^{-1} and can be produced from renewable resources. Lignocellulosic biomass is a promising source for ethanol because of the high content of cellulose and hemicelluloses and their abundance almost all over the world. However, from a technological point of view, conversion of lignocellulosic materials to ethanol is much more difficult than that of sugar or starch containing materials. Currently, production costs for lignocellulosic ethanol are 2,5 to 3 times higher than for ethanol derived from starch or sugar containing plants, which implies that second generation ethanol is economically not yet competitive to first generation ethanol.

With the implementation of ethanol as fuel, a much more complex molecule and following a much more complex oxidation reaction compared to the simple oxyhydrogen reaction has to be catalysed. The direct oxidation of ethanol proceeds via multiple pathways and intermediates. The high number of atoms increases the number of electrooxidation steps and creates a network of reactions leading to different products. Catalysis plays an important role in order lead the molecule to the desired complete oxidation which gains the maximum of energy.

The key to control the reaction and particularly the formation of adsorbed intermediates are the catalytic properties of the electrode material and hence it is a prerequisite to identify the processes

on the electrode surface in order to align the reaction to complete oxidation. The literature in recent years has concentrated on nickel and gold as potential non-PGM catalysts for the EOR. The electrocatalytic activity towards the oxidation of small organic molecules at high pH of non platinum group metals such as nickel and gold are well explored. For heterogeneous catalysis on gold, the strong influence of the support material and the metal particle size on the catalytic properties are well understood. Based on existing results in literature, assumptions on the reaction mechanism of the electrocatalysis of the EOR on gold were made. The literature on nickel as an electrocatalyst is not so well reviewed, although results on alcohol oxidation have been published for 50 years. These promising results warrant a closer look at the complex electrochemistry of nickel. Most of the scientific literature on electrocatalysis of nickel report on bulk nickel sheets or grids, but hardly discuss carbon supported Ni catalysts with small particle sizes.

The aim of the experimental work was to develop PGM free highly active anode catalysts for ADEFCs. Implementation of alkaline DEFCs requires active and stable catalysts. A screening for activity towards the EOR was performed among transition metals and compounds in order to pick out the most active metals for further investigations. The most auspicious results were obtained with nickel and gold catalysts. Supported nickel and gold catalyst systems represent a promising alternative to expensive and rare Pt group metals.

Since electrocatalytic reactions take place on the surface of the catalyst, they are very sensitive to the heterogeneous interface. This interface is not only influenced by the catalyst surface, electrolyte ions and reaction products are also involved in this dynamic interplay of the active site of the catalyst. The focus was therefore set to optimize the surface of the catalyst and adapt the preparation methods and materials. Three main topics can be identified in order to develop an active anode electrocatalyst for DEFCS:

- Support materials
- Preparation method
- Bimetallic catalysts

Oxidation of ethanol on various catalysts has been studied. Nickel as well as gold exhibits a strong activity towards the EOR in alkaline medium. The pretreatment of the carbon support material has a great impact on the activity of the electrocatalyst. This impact is due to different particle sizes, structures and loadings of the metals. For both carbon support materials (Vulcan XC72 and CNFs) the pretreatment enhances the activity of the catalyst and the metal loading. Several nickel and one gold catalysts supported on different carbon materials with varied pretreatment have been prepared and their activity and stability towards the ethanol oxidation reaction has been examined.

Deposition of gold on different pretreated carbon support materials resulted in different metal structures and activities. Oxidative pretreatment led to a fine dispersion of nanoparticles and high current densities from the EOR. Deposition of gold on thermally pretreated support (C_{therm}) resulted in a plurality of structures on carbon. Coral like structures, nanoparticles and bigger gold agglomerations were detected. The onset potential of the EOR on C_{therm} lowered due to a higher amount of gold atoms with low orientation and high energy level.

The choice of the support material of nickel catalyst is of great interest due to its ability to influence the phase transitions of the metal and therefore to facilitate the targeted oxidation. Nickel deposition on $C_{therm.}$ Based on these results C_{therm} was chosen as support material for the following electrocatalysts.

One of the most important tools to create an adequate surface for the electrooxidation of organic compounds is the synthesis of the electrocatalyst. Two different methods were applied. Furthermore, the choice of the synthesis protocol has a great impact on the metal loading of the catalysts, but the impact is strongly dependent on the metal. The nickel loading was significantly enhanced by the application of a w/o microemulsion method, on gold the effect was contrary. This method causes an enhancement in stability and higher currents. The structured surface of gold deposits enlarges the active surface and results in higher currents despite the lower actual metal loading. The impact on Ni deposition is not as pronounced as on gold.

The application of both metals as alloy or co-deposit can solve several problems of the catalysis of the EOR at once. The peak current of the EOR catalyzed by gold occurs earlier than by nickel, but the produced current is considerably lower as compared to nickel. The combination of these two metals allows the EOR to take place at a broader potential range. Different methods for the preparation of bimetallic catalysts were applied: codeposition, subsequent deposition and a galvanic replacement reaction. The use of Au and Ni simultaneously delivered higher amounts of current than with single metals even though only half of the amount of metal was used for preparation. Although the onset potential on Ni is strongly lowered, the overpotential is still very high. The highest activity was recorded with an AuNi catalyst deposited with a w/o microemulsion synthesis and a subsequent galvanic replacement on thermally pretreated Vulcan XC72. The onset potential of the EOR was reduced to 0,54 V and a limiting current density of 374 mA/cm^2 was determined with chronoamperometric experiments. Regarding the cost of the metals, the use of bimetallic catalysts is still reasonable because gold can be replaced to a certain extent by the cheap metal nickel without loss on activity.

7. Literature

[1] New Energy World-IG, Fuel Cell and Hydrogen Technologies in Europe- Financial and Technology Outlook on the European Sector Ambition 2014-2020, 2011.

[2] Platinum Today Price Charts, Http://www.platinum.matthey.com/prices/price-charts, Accessed on 25.4.2013, 2013.

[3] Precious Metals and Commodity Metal Daily Price Chart, Http://www.vincentmetals.com/metal-price-data, Accessed on 25.4.2013, 2013.

[4] E. Gülzow, Journal of Power Sources 61 (1996) 99-104.

[5] M. Cifrain, K. Kordesch, in:, W. Vielstich, A. Lamm, H. Gasteiger (Eds.), Handbook of Fuel Cells-Fundametnals, Technology and Applications Volume 1: Fundamentals and Survey of Systems, John Wiley & Sons Ltd, Quichester, Great Britain, 2003, pp. 267-280.

[6] M. Warshay, P. Prokopius, Journal of Power Sources 29 (1990) 193-200.

[7] K. Kordesch, V. Hacker, J. Gsellmann, M. Cifrain, G. Faleschini, P. Enzinger, R. Fankhauser, M. Ortner, M. Muhr, R.R. Aronson, Journal of Power Sources 86 (2000) 162-165.

[8] S.D. Fraser, V. Hacker, K. Kordesch, Encyclopedia of Electrochemical Power Sources, Volume II (2009) 344-352.

[9] B.Y.S. Lin, D.W. Kirk, S.J. Thorpe, Journal of Power Sources 161 (2006) 474-483.

[10] M. Schulze, E. Gülzow, Encyclopedia of Electrochemical Power Sources, Volume II (2009) 353-361.

[11] J.R. Varcoe, J.P. Kizewski, D.M. Halepoto, S.D. Poynton, R.C.T. Slade, F. Zhao, Encyclopedia of Electrochemical Power Sources, Volume II (2009) 329-342.

[12] S. Markgraf, M. Hörenz, T. Schmiel, W. Jehle, J. Lucas, N. Henn, Journal of Power Sources 201 (2012) 236-242.

[13] G. McLean, T. Niet, S. Prince-Richard, N. Djilali, International Journal of Hydrogen Energy 27 (2002) 507-526.

[14] E. Agel, J. Bouet, J. Fauvarque, H. Yassir, Annales De Chimie: Science Des Materiaux 26 (2001) 59-68.

[15] E. Agel, J. Bouet, J.F. Fauvarque, Journal of Power Sources 101 (2001) 267-274.

[16] G. Merle, M. Wessling, K. Nijmeijer, Journal of Membrane Science 377 (2011) 1-35.

[17] B. Bauer, H. Strathmann, Desalination 79 (1990) 125-144.

[18] C.G. Arges, V. Ramani, P.N. Pintauro, The Electrochemical Society Interface 19 (2010) 31-35.

[19] W. Jaeger, J. Bohrisch, A. Laschewsky, Progress in Polymer Science 35 (2010) 511-577.

[20] G. Couture, A. Alaaeddine, F. Boschet, B. Ameduri, Progress in Polymer Science 36 (2011) 1521-1557.

[21] L. Jörissen, V. Gogel, Encyclopedia of Electrochemical Power Sources, Volume II (2009) 370-380.

[22] E.H. Yu, X. Wang, U. Krewer, L. Li, K. Scott, Energy & Environmental Science 5 (2012) 5668.

[23] J.R. Varcoe, R.C.T. Slade, Fuel Cells 5 (2005) 187-200.

[24] T.S. Zhao, Z.X. Liang, J.B. Xu, Encyclopedia of Electrochemical Power Sources, Volume II (2009) 362-369.

[25] E.H. Yu, U. Krewer, K. Scott, Energies 3 (2010) 1499-1528.

[26] U.B. Demirci, Journal of Power Sources 169 (2007) 239-246.

[27] W. Zhou, Z. Zhou, S. Song, W. Li, G. Sun, P. Tsiakaras, Q. Xin, Applied Catalysis B: Environmental 46 (2003) 273-285.

[28] L. Jiang, G. Sun, Encyclopedia of Electrochemical Power Sources, Volume II (2009) 390-401.

[29] P.W. Atkins, Physikalische Chemie, 3rd ed., Oxford University Press, Weinheim, Germany, 1987.

[30] N. Sarkar, S.K. Ghosh, S. Bannerjee, K. Aikat, Renewable Energy 37 (2011) 19-27.

[31] C. Hamelinck, G. Hooijdonk, A. Faaij, Biomass and Bioenergy 28 (2005) 384-410.

[32] A. Demirbas, Progress in Energy and Combustion Science 33 (2007) 1-18.

[33] Biokraftstoffe Im Verkehrssektor 2011, Bundesministerum Für Land- Und Forstwirtschaft, Umwelt- Und Wasserwirtschaft, 2011.

[34] N. Schmitz, Schriftenreihe Nachwachsende Rohstoffe, Deutsches Bundesministerium Für Verbraucherschutz, Ernährunf Und Landwirtschaft 21 (2003).

[35] Statistik Austria, Statistisches Jahrbuch 2011.

[36] M. Balat, H. Balat, C. Öz, Progress in Energy and Combustion Science 34 (2008) 551-573.

[37] J.J. Cheng, G.R. Timilsina, Renewable Energy 36 (2011) 3541-3549.

[38] G. Sivakumar, D.R. Vail, J. Xu, D.M. Burner, J.O. Lay, X. Ge, P.J. Weathers, Engineering in Life Sciences 10 (2010) 8-18.

[39] B. Kamm, M. Kamm, Applied Microbiology and Biotechnology 64 (2004) 137-45.

[40] Y. Sun, J. Cheng, Bioresource Technology 83 (2002) 1-11.

[41] A.C. O'Sullivan, Cellulose 4 (1997) 173–207.

[42] D. Klemm, B. Heublein, H.-P. Fink, A. Bohn, Angewandte Chemie (International Ed. in English) 44 (2005) 3358-93.

[43] B.C. Saha, Journal of Industrial Microbiology & Biotechnology 30 (2003) 279-91.

[44] G. Neutelings, Plant Science: an International Journal of Experimental Plant Biology 181 (2011) 379-86.

[45] S. Kim, B. Dale, Biomass and Bioenergy 26 (2004) 361-375.

[46] B. Hahn-Hägerdal, M. Galbe, M.F. Gorwa-Grauslund, G. Lidén, G. Zacchi, Trends in Biotechnology 24 (2006) 549-56.

[47] K. Hoyer, M. Galbe, G. Zacchi, Journal of Chemical Technology Biotechnology 84 (2009) 570-577.

[48] W.E. Mabee, D.J. Gregg, C. Arato, A. Berlin, R. Bura, N. Gilkes, O. Mirochnik, X. Pan, E.K. Pye, J.N. Saddler, Applied Biochemistry and Biotechnology 129-132 (2006) 55-70.

[49] M.J. Taherzadeh, K. Karimi, International Journal of Molecular Sciences 9 (2008) 1621-51.

[50] E. a Bayer, R. Lamed, M.E. Himmel, Current Opinion in Biotechnology 18 (2007) 237-45.

[51] V. Jafari, S.R. Labafzadeh, A. Jeihanipour, K. Karimi, M.J. Taherzadeh, Renewable Energy 36 (2011) 2771-2775.

[52] D.H. Cho, S.-J. Shin, Y. Bae, C. Park, Y.H. Kim, Bioresource Technology 102 (2011) 4439-43.

[53] M. Balat, Energy Conversion and Management 52 (2011) 858-875.

[54] A.L. Villanueva Perales, C. Reyes Valle, P. Ollero, A. Gómez-Barea, Energy 36 (2011) 4097-4108.

[55] A. Limayem, S.C. Ricke, Progress in Energy and Combustion Science 38 (2012) 449-467.

[56] M. Galbe, G. Zacchi, Advances in Biochemical Engineering/biotechnology 19 (2007) 41-65.

[57] P. Kumar, D.M. Barrett, M.J. Delwiche, P. Stroeve, Industrial & Engineering Chemistry Research 48 (2009) 3713–3729.

[58] A.D. Rosa, A.D. Mines, R. Banzon, Z. Simbul-Nuguid, Radiation Physics and Chemistry 22 (1983) 861-867.

[59] F. Carvalheiro, L.C. Duarte, F.M. Gìrio, Journal of Scientific & Industrial Research 67 (2008) 849–864.

[60] R. Gupta, Y. Lee, Biotechnology Progress 25 (2009) 357–364.

[61] C.S. Gong, N.J. Cao, J. Du, G.T. Tsao, Advances in Biochemical Engineering/biotechnology 65 (1999) 207-41.

[62] T.H. Kim, Y.Y. Lee, Bioresource Technology 96 (2005) 2007-13.

[63] B. Yang, C.E. Wyman, Biofuels, Bioproducts and Biorefining 2 (2008) 26–40.

[64] C. Maes, J.A. Delcour, Journal of Cereal Science 34 (2001) 29-35.

[65] P. Martel, J.M. Gould, Journal of Applied Polymer Science 39 (1990) 707-714.

[66] G. Banerjee, S. Car, J.S. Scott-Craig, D.B. Hodge, J.D. Walton, Biotechnology for Biofuels 4 (2011) 16.

[67] M.J. Taherzadeh, K. Karimi, BioResources 2 (2007) 707-738.

[68] M.A.T. García-Cubero, G. González-Benito, I. Indacoechea, M. Coca, S. Bolado, Bioresource Technology 100 (2009) 1608-13.

[69] K. Shill, S. Padmanabhan, Q. Xin, J.M. Prausnitz, D.S. Clark, H.W. Blanch, Biotechnology and Bioengineering 108 (2011) 511-20.

[70] D. Fu, G. Mazza, Bioresource Technology 102 (2011) 7008-11.

[71] A. Brandt, M.J. Ray, T.Q. To, D.J. Leak, R.J. Murphy, T. Welton, Green Chemistry 13 (2011) 2489.

[72] H.W. Blanch, B. a Simmons, D. Klein-Marcuschamer, Biotechnology Journal 6 (2011) 1086-102.

[73] P. Alvira, E. Tomás-Pejó, M. Ballesteros, M.J. Negro, Bioresource Technology 101 (2010) 4851-61.

[74] N. Mosier, C. Wyman, B. Dale, R. Elander, Y.Y. Lee, M. Holtzapple, M. Ladisch, Bioresource Technology 96 (2005) 673-86.

[75] S.P.S. Chundawat, B. Venkatesh, B.E. Dale, Biotechnology and Bioengineering 96 (2007) 219–231.

[76] N. Narayanaswamy, A. Faik, D.J. Goetz, T. Gu, Bioresource Technology 102 (2011) 6995-7000.

[77] M. Galbe, G. Zacchi, Applied Microbiology and Biotechnology 59 (2002) 618-28.

[78] C.E. Wyman, Bioresource Technology 50 (1994) 3-15.

[79] J. McMillan, Renewable Energy 10 (1997) 295-302.

[80] J.D. Stephen, W.E. Mabee, J.N. Saddler, Biofuels, Bioprod. Bioref. 6 (2012) 159-176.

[81] J. Lane, BiofuelsDigest (2012).

[82] V. Menon, M. Rao, Progress in Energy and Combustion Science 38 (2012) 522-550.

[83] E. Antolini, Journal of Power Sources 170 (2007) 1-12.

[84] F. Vigier, S. Rousseau, C. Coutanceau, J.-M. Leger, C. Lamy, Topics in Catalysis 40 (2006) 111-121.

[85] C. Lamy, E. Belgsir, J. Leger, Journal of Applied Electrochemistry 31 (2001) 799–809.

[86] H. Hitmi, E.M. Belgsir, J.-M. Léger, C. Lamy, R.O. Lezna, Electrochimica Acta 39 (1994) 407-415.

[87] E.L. Gyenge, in:, J. Zhang (Ed.), PEM Fuel Cell Electrocatalysts and Catalyst Layers, Springer-Verlag London Limited, London, 2008, pp. 165-287.

[88] J. Willsau, J. Heitbaum, Journal of Electroanalytical Chemistryl 194 (1985) 27-35.

[89] H. Wang, Z. Jusys, R.J. Behm, The Journal of Physical Chemistry B 108 (2004) 19413-19424.

[90] G. a. Camara, T. Iwasita, Journal of Electroanalytical Chemistry 578 (2005) 315-321.

[91] J. Mann, N. Yao, A.B. Bocarsly, Langmuir□: the ACS Journal of Surfaces and Colloids 22 (2006) 10432-6.

[92] S.C.S. Lai, M.T.M. Koper, Physical Chemistry Chemical Physics: PCCP 11 (2009) 10446-10456.

[93] B. Braunchweig, D. Hibbitts, M. Neurock, a. Wieckowski, Catalysis Today 202 (2013) 197-209.

[94] T. Iwasita, E. Pastor, Electrochimica Acta 39 (1994) 531-537.

[95] U. Krewer, T. Vidakovic-Koch, L. Rihko-Struckmann, Chemphyschem□: a European Journal of Chemical Physics and Physical Chemistry 12 (2011) 2518-44.

[96] J. Leger, S. Rousseau, C. Coutanceau, F. Hahn, C. Lamy, Electrochimica Acta 50 (2005) 5118-5125.

[97] D. Bayer, S. Berenger, M. Joos, C. Cremers, J. Tübke, International Journal of Hydrogen Energy 35 (2010) 12660-12667.

[98] E.R. Gonzalez, E. Antolini, in:, J. Garche, C.K. Dyer, P.T. Moseley, Z. Ogumi, D.A.J. Rand, B. Scrosati (Eds.), Encyclopedia of Electrochemical Power Sources, Volume II, Elsevier B.V., Amsterdam, The Netherlands, 2009, pp. 402-411.

[99] E. Antolini, E.R. Gonzalez, Journal of Power Sources 195 (2010) 3431-3450.

[100] C. Bianchini, P.K. Shen, Chemical Reviews 109 (2009) 4183-4206.

[101] C. Bezerra, L. Zhang, K. Lee, H. Liu, a Marques, E. Marques, H. Wang, J. Zhang, Electrochimica Acta 53 (2008) 4937-4951.

[102] L. Zhang, J. Zhang, D. Wilkinson, H. Wang, Journal of Power Sources 156 (2006) 171-182.

[103] N. Park, T. Shiraishi, K. Kamisugi, Y. Hara, K. Iizuka, T. Kado, S. Hayase, Journal of Applied Electrochemistry 38 (2007) 371-375.

[104] Z.X. Liang, T.S. Zhao, J.B. Xu, L.D. Zhu, Electrochimica Acta 54 (2009) 2203-2208.

[105] D.T. Shieh, B.J. Hwang, Journal of the Electrochemical Society 142 (1995) 816.

[106] J. Kim, S.-M. Park, Journal of the Electrochemical Society 146 (1999) 1075-1080.

[107] M.R. Tarasevich, Z.R. Karichev, V. a. Bogdanovskaya, E.N. Lubnin, a. V. Kapustin, Electrochemistry Communications 7 (2005) 141-146.

[108] Q. He, S. Mukerjee, B. Shyam, D. Ramaker, S. Parres-Esclapez, M. Illán-Gómez, A. Bueno-López, Journal of Power Sources 193 (2009) 408–415.

[109] G.C. Bond, D.T. Thompson, Catalysis Reviews-Sci Eng 41 (1999) 319-388.

[110] B. Hammer, J. Norskov, Nature 376 (1995) 238–240.

[111] A. Holleman, E. Wiberg, Lehrbuch Der Anorganischen Chemie, 101st ed., Walter de Gruyter, Berlin, New York, 1995.

[112] R. Meyer, C. Lemire, S.K. Shaikhutdinov, H.J. Freund, Gold Bulletin 37 (2004) 72–124.

[113] G.C. Bond, Gold Bulletin 34 (2001) 117-119.

[114] L.M. Molina, B. Hammer, Applied Catalysis A: General 291 (2005) 21-31.

[115] M. Haruta, Catalysis Surveys from Japan 1 (1997) 61–73.

[116] D. Thompson, Gold Bulletin 31 (1998) 111–118.

[117] D. Cameron, R. Holliday, D. Thompson, Journal of Power Sources 118 (2003) 298-303.

[118] D.T. Thompson, Platinum Metals Review 48 (2004) 169-172.

[119] M. Haruta, M. Daté, Applied Catalysis A: General 222 (2001) 427-437.

[120] M. Haruta, A. Ueda, S. Tsubota, R.M. Torres Sanchez, Catalysis Today 29 (1996) 443-447.

[121] M. Haruta, Gold Bulletin 37 (2004) 27-36.

[122] M. Haruta, Cattech 6 (2002) 102-115.

[123] M. Haruta, Catalysis Today 36 (1997) 153-166.

[124] C.W. Corti, R.J. Holliday, D.T. Thompson, Topics in Catalysis 44 (2007) 331-343.

[125] Y. Kwon, S.C.S. Lai, P. Rodriguez, M.T.M. Koper, Journal of the American Chemical Society 133 (2011) 6914-7.

[126] L.D. Burke, D.T. Buckley, J.A. Morrissey, The Analyst 119 (1994) 841.

[127] L. Burke, P. Nugent, Gold Bulletin 30 (1997) 43–53.

[128] S.C.S. Lai, S.E.F. Kleijn, F.T.Z. Öztürk, V.C. van Rees Vellinga, J. Koning, P. Rodriguez, M.T.M. Koper, Catalysis Today 154 (2010) 92-104.

[129] P. Ocon, C. Alonso, R. Celdran, J. Gonzalez-Velasco, Journal of Electroanalytical Chemistry 206 (1986) 179-196.

[130] M. Beltowska-Brzezinska, Electrochimica Acta 24 (1979) 409–413.

[131] A. Chen, J. Lipkowski, The Journal of Physical Chemistry B 103 (1999) 682-691.

[132] K.A. Assiongbon, D. Roy, Surface Science 594 (2005) 99-119.

[133] G. Tremiliosi-Filho, E.. Gonzalez, A.J. Motheo, E.. Belgsir, J.-M. Léger, C. Lamy, Journal of Electroanalytical Chemistry 444 (1998) 31-39.

[134] B. Beden, I. Cetin, A. Kahyaoglu, D. Takky, C. Lamy, Journal of Catalysis 104 (1987) 37–46.

[135] D.A.J. Rand, R. Woods, Journal of Electroanalytical Chemistry and Interfacial Electrochemistry 31 (1971) 29-38.

[136] G. Tremiliosi-Filho, L.H. Dall' Antonia, G. Jerkiewicz, Journal of Electroanalytical Chemistry 422 (1997) 149-159.

[137] H. Kita, H. Nakajima, K. Hayashi, Journal of Electroanalytical Chemistry and Interfacial Electrochemistry 190 (1985) 141–156.

[138] Z. Borkowska, Electrochimica Acta 49 (2004) 2613-2621.

[139] Z. Borkowska, Electrochimica Acta 49 (2004) 1209-1220.

[140] A.P. O'Mullane, S.J. Ippolito, Y.M. Sabri, V. Bansal, S.K. Bhargava, Langmuir: the ACS Journal of Surfaces and Colloids 25 (2009) 3845-3852.

[141] M. Beltowska-Brzezinska, W. Vielstich, Electrochimica Acta 22 (1977) 1313–1314.

[142] D. Takky, B. Beden, J.M. Leger, C. Lamy, Journal of Electroanalytical Chemistry 145 (1983) 461-466.

[143] P. Rodriguez, Y. Kwon, M.T.M. Koper, Nature Chemistry (2011) 1-6.

[144] F. Kadirgan, E. Bouhier-Charbonnier, C. Lamy, J.M. Léger, B. Beden, Journal of Electroanalytical Chemistry 286 (1990) 41-61.

[145] B. Beden, F. Kadirgan, A. Kahyaoglu, C. Lamy, Journal of Electroanalytical Chemistry 135 (1982) 329-334.

[146] J. Zhang, Y. Liang, N. Li, Z. Li, C. Xu, S. Jiang, Electrochimica Acta (2011) 8-11.

[147] Y. Kwon, K.J.P. Schouten, M.T.M. Koper, ChemCatChem 3 (2011) 1176-1185.

[148] A. Habrioux, K. Servat, T. Girardeau, P. Guérin, T.W. Napporn, K.B. Kokoh, Current Applied Physics 11 (2011) 1149-1152.

[149] P. Parpot, S.G. Pires, A. Bettencourt, Journal of Electroanalytical Chemistry 566 (2004) 401-408.

[150] K. Yahikozawa, K. Nishimura, M. Kumazawa, N. Tateishi, Y. Takasu, K. Yasuda, Y. Matsuda, Electrochimica Acta 37 (1992) 453-455.

[151] M. BeLtowska-Brzezinska, Electrochimica Acta 30 (1985) 1193-1198.

[152] R. De Lima, H. Varela, Gold Bulletin 41 (2008) 15–22.

[153] J. Hernandez, J. Sollagullon, E. Herrero, A. Aldaz, J. Feliu, Electrochimica Acta 52 (2006) 1662-1669.

[154] S. Yongprapat, A. Therdthianwong, S. Therdthianwong, Journal of Applied Electrochemistry (2012).

[155] D.H. Nagaraju, V. Lakshminarayanan, The Journal of Physical Chemistry C 113 (2009) 14922-14926.

[156] B.N. Zope, D.D. Hibbitts, M. Neurock, R.J. Davis, Science (New York, N.Y.) 330 (2010) 74-8.

[157] J. Gong, Chemical Reviews 112 (2012) 2987-3054.

[158] R. Holze, T. Luczak, M. Bełtowska-Brzezinska, Electrochimica Acta 39 (1994) 485-489.

[159] A.M.A. Ouf, A.M. Abd Elhafeez, A. El-Shafei, Journal of Solid State Electrochemistry 12 (2008) 601–607.

[160] Z. Xu, J. Yu, G. Liu, Electrochemistry Communications 13 (2011) 1260-1263.

[161] M.-C. Daniel, D. Astruc, Chemical Reviews 104 (2004) 293-346.

[162] S.-P. Tung, T.-K. Huang, C.-Y. Lee, H.-T. Chiu, RSC Advances 2 (2012) 1068.

[163] N. Tateishi, K. Nishimura, K. Yahikozawa, M. Nakagawa, M. Yamada, Y. Takasu, Journal of Electroanalytical Chemistry 352 (1993) 243–252.

[164] R.K. Pandey, V. Lakshminarayanan, Applied Catalysis B: Environmental 125 (2012) 271-281.

[165] M. Tominaga, T. Shimazoe, M. Nagashima, I. Taniguchi, Electrochemistry Communications 7 (2005) 189-193.

[166] Y. Chen, L. Zhuang, J. Lu, Chinese Journal of Catalysis 28 (2007) 870-874.

[167] J. Garche, ed., Encyclopedia of Electrochemical Power Sources, Volume I, Elsevier B.V., 2009.

[168] A. Seghiouer, J. Chevalet, A. Barhoun, F. Lantelme, Journal of Electroanalytical Chemistry 442 (1998) 113-123.

[169] H. Bode, K. Dehmelt, J. Witte, Electrochimica Acta 11 (1966) 1079-1087.

[170] J. Marinas, J. Campelo, D. Luna, Studies in Surface Science And 27 (1986) 411-457.

[171] M. Fleischmann, K. Korinek, D. Pletcher, Journal of Electroanalytical Chemistry and Interfacial Electrochemistry 31 (1971) 39-49.

[172] W. Visscher, E. Barendrecht, Journal of Electroanalytical Chemistry 154 (1983) 69-80.

[173] P. Oliva, J. Leonardi, J. Laurent, C. Delmas, J. Braconnier, M. Figlarz, F. Fievet, A. Guibert, Journal of Power Sources 8 (1982) 229–255.

[174] M. Rajamathi, P. Vishnu Kamath, Journal of Power Sources 70 (1998) 118–121.

[175] R. Huggins, H. Prinz, M. Wohlfahrt-Mehrens, L. Jörissen, W. Witschel, Solid State Ionics 70 (1994) 417-424.

[176] G. Barral, S. Maximovitch, F. Njanjo-Eyoke, Electrochimica Acta 41 (1996) 1305-1311.

[177] B.E. Conway, M.A. Sattar, D. Gilroy, Electrochimica Acta 14 (1969).

[178] B. Beden, A. Bewick, Electrochimica Acta 33 (1988) 1695-1698.

[179] J. Desilvestro, D.A. Corrigan, M.J. Weaver, Journal of the Electrochemical Society 135 (1988) 885-892.

[180] P. Häring, R. Kötz, Journal of Electroanalytical Chemistry 385 (1995) 273-277.

[181] W. Sung, J.W. Choi, Journal of Power Sources 172 (2007) 198–208.

[182] W. Visscher, E. Barendrecht, Electrochimica Acta 25 (1980) 651-655.

[183] F. Hahn, B. Beden, M. Croissant, C. Lamy, Electrochimica Acta 31 (1986) 335-342.

[184] L.M.M.D. Souza, F.P. Kong, F.R. McLarnont, R.H. Muller, Electrochimica Acta 42 (1997) 1253-1267.

[185] S.L. Medway, C.A. Lucas, A. Kowal, R.J. Nichols, D. Johnson, Journal of Electroanalytical Chemistry 587 (2006) 172-181.

[186] F. Hahn, D. Floner, B. Beden, C. Lamy, Electrochimica Acta 32 (1987) 1631-1636.

[187] M. Fleischmann, K. Korinek, D. Pletcher, J. Chem. Soc., Perkin Trans. 2 (1972) 1396–1403.

[188] A.A. El-Shafei, Journal of Electroanalytical Chemistry 471 (1999) 89-95.

[189] A. Ehsani, M.G. Mahjani, M. Jafarian, A. Naeemy, Electrochimica Acta 71 (2012) 128-133.

[190] M. Schulze, E. Gülzow, Journal of Power Sources 127 (2004) 252-263.

[191] M. Schulze, E. Gülzow, G. Steinhilber, Applied Surface Science 179 (2001) 251-256.

[192] S. Gultekin, M. Al-Saleh, A. Al-Zakri, K.A.A. Abbas, International Journal of Hydrogen Energy 21 (1996) 485-489.

[193] S.A.S. Machado, J. Tiengo, P. de Lima Neto, L. a. Avaca, Electrochimica Acta 39 (1994) 1757-1761.

[194] R. Solmaz, G. Kardaş, Electrochimica Acta 54 (2009) 3726-3734.

[195] M.R. da Silva, A.C.D. Ângelo, Quim. Nova 33 (2010) 2027–2031.

[196] N.A. Choudhry, C.E. Banks, Analytical Methods 3 (2011) 74.

[197] A. Kowal, S.N. Port, R.J. Nichols, Catalysis Today 38 (1997) 483-492.

[198] S. Berchmans, H. Gomathi, G. Prabhakara Rao, Journal of Electroanalytical Chemistry 394 (1995) 267-270.

[199] Y. Hori, A. Murata, Electrochimica Acta 35 (1990) 1777-1780.

[200] I. Danaee, M. Jafarian, F. Forouzandeh, F. Gobal, M. Mahjani, International Journal of Hydrogen Energy 33 (2008) 4367–4376.

[201] M. Dmochowska, A. Czerwinski, Journal of Solid State Electrochemistry (1998) 16-23.

[202] M. Zhao, K. Wang, D.A. Scherson, Journal of Physical Chemistry 97 (1993) 4488-4490.

[203] R. van Effen, D. Evans, Journal of Electroanalytical Chemistry 103 (1979) 383-397.

[204] S.C. Chang, Y. Ho, M.J. Weaver, Journal of the American Chemical Society 113 (1991) 9506-9513.

[205] P. Robertson, Journal of Electroanalytical Chemistry and Interfacial Electrochemistry 111 (1980) 97-104.

[206] H. Hassan, Z. Abdel Hamid, International Journal of Hydrogen Energy 36 (2011) 5117-5127.

[207] N.M. Suleimanov, S.M. Khantimerov, E.F. Kukovitsky, V.L. Matukhin, Journal of Solid State Electrochemistry 12 (2008) 1021-1023.

[208] C. Xu, Y. Hu, J. Rong, S.P. Jiang, Y. Liu, Electrochemistry Communications 9 (2007) 2009-2012.

[209] G.-P. Jin, R. Baron, L. Xiao, R.G. Compton, Journal of Nanoscience and Nanotechnology 9 (2009) 2719-2725.

[210] Y. Yi, S. Uhm, J. Lee, Electrocatalysis 1 (2010) 104-107.

[211] J.B. Raoof, N. Azizi, R. Ojani, S. Ghodrati, M. Abrishamkar, F. Chekin, International Journal of Hydrogen Energy 36 (2011) 13295-13300.

[212] Z. Mojović, P. Banković, N. Jović-Jovičić, A. Milutinović-Nikolić, A. Abu Rabi-Stanković, D. Jovanović, International Journal of Hydrogen Energy 36 (2011) 13343-13351.

[213] A. Ciszewski, G. Milczarek, Journal of Electroanalytical Chemistry 413 (1996) 137-142.

[214] W.S. Cardoso, V.L.N. Dias, W.M. Costa, I. Araujo Rodrigues, E.P. Marques, A.G. Sousa, J. Boaventura, C.W.B. Bezerra, C. Song, H. Liu, J. Zhang, A.L.B. Marques, Journal of Applied Electrochemistry 39 (2008) 55-64.

[215] G. Roslonek, J. Taraszewska, Journal of Electroanalytical Chemistry 325 (1992) 285-300.

[216] K.L. Nagashree, M.F. Ahmed, Journal of Solid State Electrochemistry 14 (2010) 2307-2320.

[217] M. Jafarian, M. Babaee, F. Gobal, M.G. Mahjani, Journal of Electroanalytical Chemistry 652 (2011) 8-12.

[218] R. Hameed, K. El-Khatib, International Journal of Hydrogen Energy 35 (2010) 2517–2529.

[219] P.F. Luo, T. Kuwana, D.K. Paul, P.M. Sherwood, Analytical Chemistry 68 (1996) 3330-7.

[220] P.F. Luo, T. Kuwana, Analytical Chemistry 66 (1994) 2775-2782.

[221] S. Maximovitch, G. Bronoel, Electrochimica Acta 26 (1981) 1331-1338.

[222] M. Jafarian, R.B. Moghaddam, M.G. Mahjani, F. Gobal, Journal of Applied Electrochemistry 36 (2006) 913-918.

[223] Y. Wang, D. Zhang, W. Peng, L. Liu, M. Li, Electrochimica Acta 56 (2011) 5754-5758.

[224] J.M. Marioli, L.E. Sereno, Electrochimica Acta 40 (1995) 983-989.

[225] Y.L. Lo, B.J. Hwang, Journal of the Electrochemical Society 142 (1995).

[226] Y.L. Lo, B.J. Hwang, Langmuir 14 (1998) 944-950.

[227] H.B. Hassan, Z.A. Hamid, International Journal of Hydrogen Energy 36 (2011) 849-856.

[228] J.S. Spendelow, A. Wieckowski, Physical Chemistry Chemical Physics: PCCP 9 (2007) 2654-75.

[229] G. Vertes, G. Horanyi, Electroanalytical Chemistry and Interfacial Electrochemistry 52 (1974) 47-53.

[230] W. Buchberger, Elektrochemische Analyseverfahren, 1st ed., Spektrum, Akad. Verl., Heidelberg, Berlin, 1998.

[231] C.H. Hamann, W. Vielstich, Elektrochemie, 4th ed., Wiley-VCH Verlag GmbH & Co. KGaA, Weinheim, Germany, 2005.

[232] M.T.M. Koper, Nanoscale 3 (2011) 2054-73.

[233] E. Auer, A. Freund, J. Pietsch, T. Tacke, Applied Catalysis A: General 173 (1998) 259-271.

[234] A.L. Dicks, Journal of Power Sources 156 (2006) 128-141.

[235] E. Antolini, Applied Catalysis B: Environmental 88 (2009) 1-24.

[236] J.-P. Tessonnier, D. Rosenthal, T.W. Hansen, C. Hess, M.E. Schuster, R. Blume, F. Girgsdies, N. Pfänder, O. Timpe, D.S. Su, R. Schlögl, Carbon 47 (2009) 1779-1798.

[237] P. Dinka, A. Mukasayan, J. Phys. Chem. B 109 (2005) 21627-21633.

[238] R.N. Singh, A. Singh, D. Mishra, P. Chartier, Journal of Power Sources 185 (2008) 776-783.

[239] U.S. Mohanty, Journal of Applied Electrochemistry 41 (2010) 257-270.

[240] C. Perego, V. Pierluigi, Catalysis Today 34 (1997) 281-305.

[241] C. Coutanceau, S. Brimaud, C. Lamy, J. Leger, L. Dubau, S. Rousseau, F. Vigier, Electrochimica Acta 53 (2008) 6865-6880.

[242] C. Bock, H. Halvorsen, B. MacDougall, in:, J. Zhang (Ed.), PEM Fuel Cell Electrocatalysts and Catalyst Layers, Springer-Verlag London Limited, London, 2008, pp. 447-485.

[243] K.S. Nagabhushana, H. Bönnemann, in:, D.J. Lockwood (Ed.), Nanotechnology in Catalysis, Kluwer Academic/Plenum Publishers, New York, 2004, pp. 51-82.

[244] H. Bönnemann, W. Brijoux, R. Brinkmann, T. Joußen, B. Korall, E. Dinjus, Angewandte Chemie International Edition in English 30 (1991) 1312-1314.

[245] A. Oliveira Neto, Journal of the European Ceramic Society 23 (2003) 2987-2992.

[246] J. Solla-Gullón, V. Montiel, A. Aldaz, J. Clavilier, Journal of The Electrochemical Society 150 (2003) E104.

[247] A. Habrioux, D. Diabaté, J. Rousseau, T.W. Napporn, K. Servat, L. Guétaz, A. Trokourey, K.B. Kokoh, Electrocatalysis 1 (2010) 51–59.

[248] C. Lamy, S. Rousseau, E. Belgsir, C. Coutanceau, J.-M. Léger, Electrochimica Acta 49 (2004) 3901-3908.

[249] U. Demirci, Journal of Power Sources 173 (2007) 11-18.

[250] M. Bienzle, T. Oishi, F. Sommer, Journal of Alloys and Compounds 220 (1995) 182-188.

[251] B.D. Chandler, C.G. Long, J.D. Gilbertson, C.J. Pursell, G. Vijayaraghavan, K.J. Stevenson, Journal of Physical Chemistry C 114 (2010) 11498-11508.

[252] S. Papadimitriou, S. Armyanov, E. Valova, A. Hubin, O. Steenhaut, E. Pavlidou, G. Kokkinidis, S. Sotiropoulos, The Journal of Physical Chemistry C 114 (2010) 5217-5223.

[253] S. Papadimitriou, A. Tegou, E. Pavlidou, S. Armyanov, E. Valova, G. Kokkinidis, S. Sotiropoulos, Electrochimica Acta 53 (2008) 6559-6567.

[254] A. Stadlhofer, V. Hacker, submitted for publication (2013)

[255] C. Santoro, A. Stadlhofer, V. Hacker, G. Squadrito, U. Schröder, B. Li, Journal of Power Sources, accepted (2013)

[256] A. Stadlhofer, M. Bodner, H. Schröttner, V. Hacker, ECS Trans. 50 (2013), 1927-1932.

8. Appendix

8.1. List of abbreviations

PEFC	polymer electrolyte fuel cell
ADEFCs	alkaline direct ethanol fuel cell
PGM	platinum group metal
EOR	ethanol oxidation reaction
AFCs	alkaline fuel cell
KOH	potassium hydroxide
CO_2	carbon dioxide
AEM	anion exchange membrane
PEM	proton exchange membrane
QA	quaternary ammonium
PEO	polyethylene oxide
PBI	polybenzimidazole
PVA	polyvinylalcohol
DAFC	direct alcohol fuel cells
DMFC	direct methanol fuel cell
PEMFC	proton exchange membrane fuel cell
ΔG^0	Gibbs free energy change
E^0	reversible cell voltage
ΔH^0	enthalpy change
η	energy conversion efficiency
ICE	internal combustion engine
DP	degree of polymerization
MSW	municipal solid waste

C&D	construction and demolition
SSF	simultaneous saccharification and fermentation
TFA	trifluoroacetic acid
AFEX	ammonia fiber explosion
ARP	ammonia recycled percolation
SAA	soaking in aqueous ammonia
AHP	alkaline hydrogen peroxide
IL	Ionic liquids
HMF	hydroxymethylfufural
SHF	separate hydrolysis and fermentation
SSCF	simultaneous saccharification and cofermentation process
DMC	direct microbial conversion
CBP	consolidated bioprocessing
ER	Eley-Rideal mechanism
LH	Langmuir-Hinshelwood mechanism
CV	cyclic voltammogram/cyclic voltammetry
EtOH	ethanol
CA	chronoamperometry
ICP-OES	Inductively coupled plasma optical emission spectrometry
SEM-EDX	Scanning electron microscopy coupled with energy dispersive X-ray spectroscopy
CNT	carbon nano tubes
CNF	carbon nanofibers
EASA	electrochemical active surface area
$NaBH_4$	sodium borohydride
EG	ethylene glycol

IWI	incipient wetness impregnations
w/o	water in oil
DEFC	direct ethanol fuel cell

8.2. List of figures

8.3. List of figures